Electrochemical and Microstructural Studies of AlPO$_4$-Nanoparticle Coated LiCoO$_2$ for Lithium-Ion Batteries

by

Anjuli T. Appapillai

B.S. Mechanical Engineering

B.S. Materials Science and Engineering
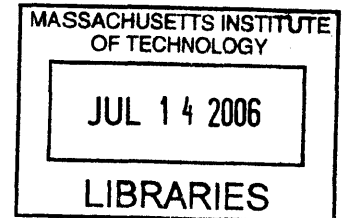
University of California at Berkeley, 2004

SUBMITTED TO THE DEPARTMENT OF MECHANICAL ENGINEERING IN

PARTIAL FULFILLMENT OF THE REQUIREMENTS FOR THE DEGREE OF

MASTER OF SCIENCE IN MECHANICAL ENGINEERING

at the

MASSACHUSETTS INSTITUTE OF TECHNOLOGY

June 2006

Signature of Author: _____
Department of Mechanical Engineering
May 2006

Certified by: _____
Yang Shao-Horn
Assistant Professor of Mechanical Engineering
Thesis Supervisor

Accepted by: _____
Lallit Anand
Professor of Mechanical Engineering
Chairman, Department Graduate Committee

Electrochemical and Microstructural Studies of AlPO$_4$-Nanoparticle Coated LiCoO$_2$ for Lithium-Ion Batteries

Anjuli T. Appapillai

ABSTRACT

AlPO$_4$-nanoparticle coated LiCoO$_2$ is studied as a positive electrode for lithium rechargeable batteries for a high-voltage charge limit of 4.7V. To understand the role of the coating in transport phenomena and in deintercalation of Li$^+$, the electrochemical behavior is studied alongside the microstructure of the coating. The galvanostatic charge profile is studied with electrochemical impedance tests conducted at various lithium contents during charging. The coating is found to increase the flatness of the two-phase region plateau and to cause the appearance of the monoclinic distortion at x=0.5 as well as distinct plateaus for O3 to H1-3 and H1-3 to O1 transitions, indicating that application of the coating transformed Li-rich LiCoO$_2$ into stoichiometric LiCoO$_2$. According to electronic resistance (R$_e$) values from impedance spectra, the coated LiCoO$_2$ has a more rapid decrease in R$_e$ with delithiation, and both materials show a rise in R$_e$ above 4.5V.

Structurally, SEM images show pitted surface morphology only on the edges of the layers of coated LiCoO$_2$. Furthermore, cross-sectional TEM images reveal a continuous coating layer with compositional variations seen through EDX mapping and point spectroscopy, indicating that a thin layer of aluminum covers the particle uniformly while the phosphorus is more concentrated in thicker, isolated clusters, which is further supported y XPS surface analysis. This coating composition may increase the ionic conductivity of the LiCoO$_2$ surface while protecting it from harmful side reactions and stabilizing the surface structure to inhibit Co dissolution.

Thesis supervisor: Yang Shao-Horn

Title: Assistant Professor of Mechanical Engineering

List Of Figures

I. Introduction

a. LiCoO$_2$ as Positive Electrode Material

Lithium cobalt oxide, LiCoO$_2$, is the most common positive electrode material used in commercial lithium rechargeable batteries. The theoretical capacity for Li$_x$CoO$_2$ is 274 mAh/g, however typically it is only charged to a lithium content of x=0.5, corresponding to a high voltage cutoff of 4.2V [1-3]. Therefore the practical capacity is approximately 140 mAh/g, and to increase the accessible capacity, the material must be charged to voltages greater than 4.3V. However, higher voltage limits such as 4.7V or 4.8V lead to capacity fade due to structural deterioration and thermal instability from electrolyte oxidation and thermal runaway.

Structurally, LiCoO$_2$ belongs to the R$\bar{3}$m space group with hexagonal cell parameters of a $\approx$ 2.816Å and c $\approx$ 14.08Å [4]. Its layered structure contains oxygen sheets with ABCABC stacking separated by alternating layers of cobalt and lithium, in a structure called O3, which is depicted schematically in Figure 1. The lithium deintercalates reversibly along the plane between CoO$_2$ slabs during charging of the battery cell [5]. Positively-charged Li$^+$ ions act as a screen to stabilize opposing negatively-charged CoO$_2$ sheets.

The phase transitions of Li$_x$CoO$_2$ during delithiation are shown in the phase diagram in Figure 2 [6]. During charge, Li$_x$CoO$_2$ undergoes a first-order phase transition for 0.75 < x < 0.96, as exhibited by a voltage plateau at 3.93V vs Li [1]. This two-phase region has

been associated with the insulator-to-metal transition, which actually occurs between 1.0

> x > 0.94, according to conductivity and NMR studies by Menetrier et al. [7].

$LiCoO_2$ experiences a second-order hexagonal-monoclinic-hexagonal transition near

x=0.5 due to lithium-vacancy ordering [1, 7, 8]. During this in-plane ordering, Li^+ ions

and vacancies are positioned in alternating rows as proposed by Reimers and Dahn [1]

and calculated theoretically by Van der Ven et al. [6] . This transition is manifested on

the voltage profile as two small plateaus at 4.07V and 4.19V [9]. However, it is

important to note that this ordering is not observed for overstoichiometric $Li_{1+y}CoO_2$, in

which excess Li^+ ions occupy sites in the Co layers [10]. In this case, the charge

difference is compensated by oxygen vacancies, and such structural defects prevent the

long-range Li-ion ordering.

At 4.55V, $LiCoO_2$ experiences a phase transition from the O3 to the H1-3 phase, which is

a hybrid between O3 and O1 phases [6]. The O1 phase, which contains the CoO_2 slabs

with ABAB stacking of oxygen layers, as opposed to the ABCABC stacking in the O3

phase, is the most thermodynamically stable phase at the fully delithiated state of CoO_2

[6]. The H1-3 phase, with a composition of x≈0.14, consists of Li sites in alternating

layers of O3 and O1 environments, which is more energetically favorable than regular

distribution of Li throughout the structure. Between x=0.50 and x=0.15, the c-axis

decreases dramatically by 4.7% [11]. Therefore, repeated cycling with a high-voltage

limit above 4.2V leads to mechanical deterioration of the layered material due to induced

strain [8]. The anisotropic nature of the 4.7% shrinkage of the c-axis parameter between 4.2V and 4.5V may cause microcracks and electrochemical grinding;

This volume decrease directly parallels the increase in cobalt dissolution during charge [11]. The amount of cobalt dissolution has been shown experimentally to follow the increase in capacity loss over 25 cycles with an upper voltage limit of 4.5V by Amatucci et al. [11]. The reason for cobalt dissolution is cited as the attack of the cathode surface by acidic species in the electrolyte solution. Aurbach has reported that formation of surface films on $LiCoO_2$ in the presence of electrolyte increases the surface impedance of the material; in particular, highly-resistive LiF is found through XPS studies as a product of the reaction between $LiCoO_2$ and trace amounts of HF acid [12].

Aside from structural and surface damage, $LiCoO_2$ also poses safety concerns by displaying thermal instability at high voltages [13-15]. When Li_xCoO_2 is delithiated, Co^{3+} is oxidized to Co^{4+}, which is an unstable oxidation state. When a large percentage of the cobalt in Li_xCoO_2 has been oxidized at low lithium contents, CoO_2 is formed, which decomposes to Co_2O_3 and O_2. At 5V, the electrolyte decomposes exothermically, raising the temperature of the cell while increasing the internal resistance. This temperature accelerates causes oxygen liberation from the positive electrode, which further accelerates electrolyte oxidation [13]. A higher degree of delithiation of the $LiCoO_2$ intensifies the amount of oxygen released, and these effects combine synergistically to cause thermal runaway in the cell, whereby exponential heat generation

surpasses linear heat dissipation from the cell, resulting in pressure buildup and explosion

or fire [16, 17].

Figure 1. The crystal structure of layered $LiCoO_2$, belonging to space group $R\overline{3}m$. The oxygen ions form close-packed planes stacked in ABCABC sequence, with alternating layers of lithium and cobalt in between.
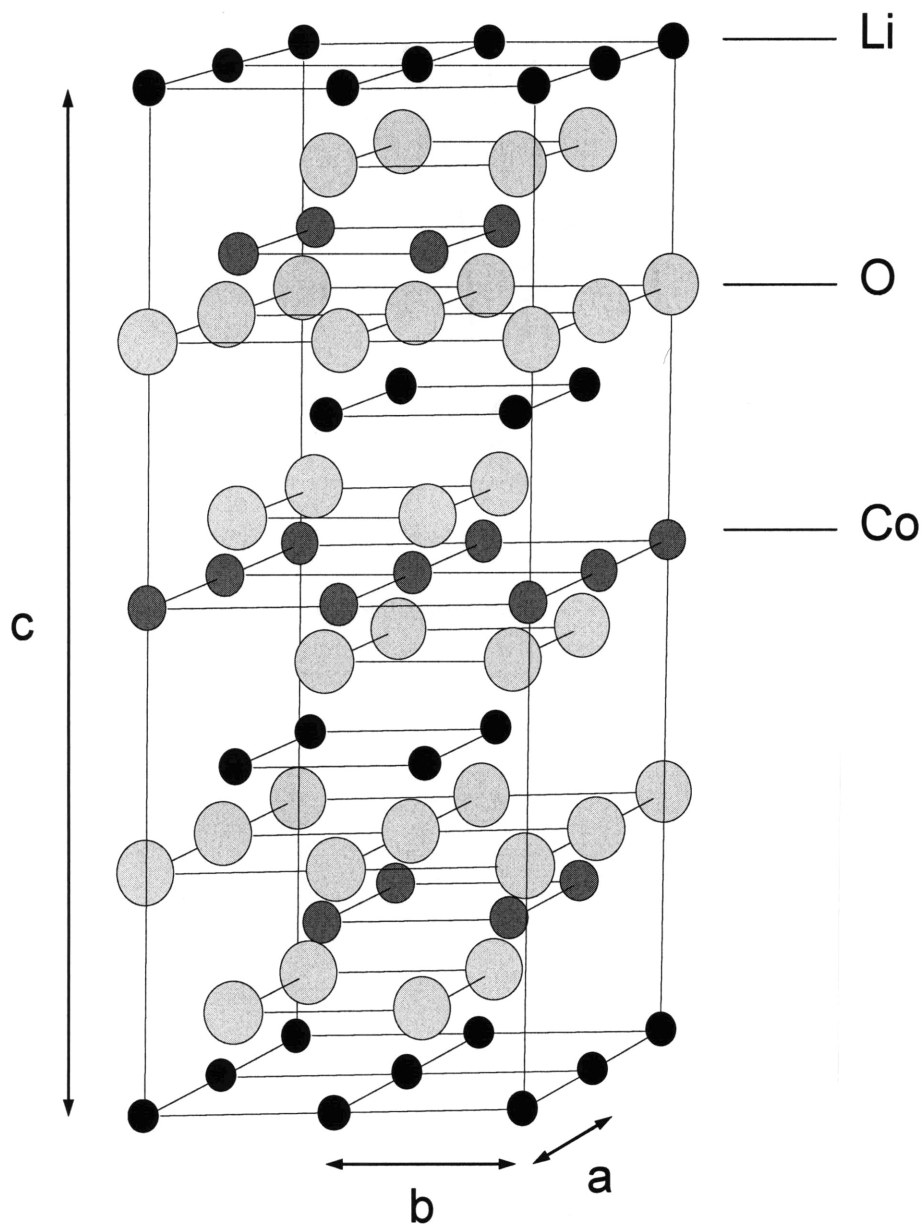
Figure 2. Phase diagram of Li_xCoO_2 based on first-principles calculations. The insets show the in-plane ordering predicted for x=0.5 and x=0.33.
(Van der Ven et al. Phys. Rev. B. 1998)
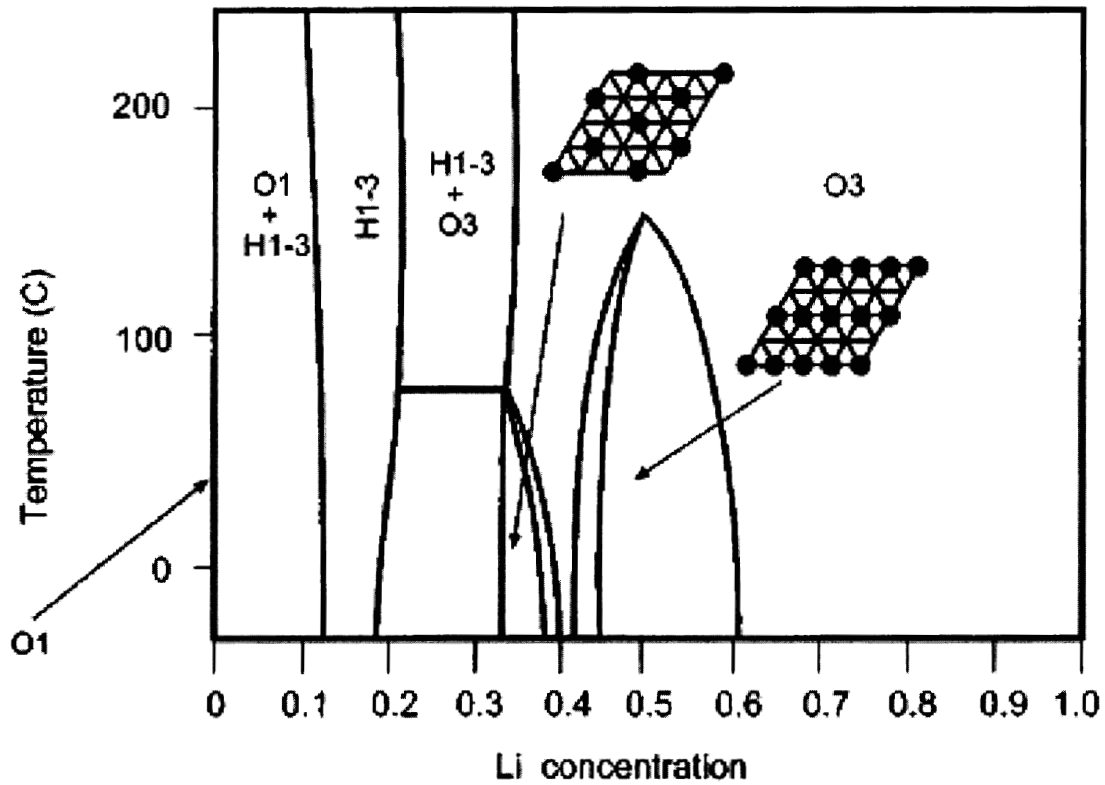
In order to access capacities closer to the theoretical value of 274 mAh/g for Li_xCoO_2, the cell must be charged to a lithium content $x \leq 0.5$, or beyond 4.2V. To lessen the mechanical, chemical and thermal instabilities previously described, different approaches have been suggested. Several researchers have tried doping or metal substitution of the material to form $LiCo_{1-y}M_yO_2$ (where M = Al, Mg, Ni) in order to increase mechanical stability by reducing the volume change of phase transitions, but this improvement was usually achieved at the expense of capacity and provided no benefits in terms of thermal stability [18, 19]. Tukamoto and West, as well as Levasseur et al., report that up to 10% Mg-doping in $LiCoO_2$ increases the electronic conductivity while removing the voltage plateau associated with the two-phase region at the start of charge and decreasing the discharge capacity [19, 20]. Levasseur et al. also report that small amounts (<6%) of Ni doping in $LiCoO_2$ produce a monotonically increasing voltage profile as well, but do not prevent lithium-vacancy ordering at x=0.5 [21]. As predicted theoretically and confirmed experimentally by Ceder et al. [22], Jang et al. find that aluminum doping of up to 50% causes an increase in open-circuit voltage compared to $LiCoO_2$, and lattice parameter changes during charging decrease by one half [18]. Furthermore, Myung et al. report that as low as 10% Al causes suppression of lithium-vacancy ordering and the two-phase region at the beginning of charge, as well as decreased discharge capacity [23]. Because doping of $LiCoO_2$ improved only some aspects of performance while neglecting thermal instability issues, many researchers turned to application of coating layers to the $LiCoO_2$ particles for structural and thermal stability.

Different nanoscale coating layers on $LiCoO_2$ particles have been investigated, including ZrO_2 [24, 25], Al_2O_3 [24-28], TiO_2 [24, 25, 29, 30], $LiAlO_2$ [31], SiO_2 [24], MgO [32] and $AlPO_4$ [33]. One common improvement among many coating technologies is the increased capacity retention, especially at higher voltage limits above 4.2V. For example, Cao et al. have shown that $LiAlO_2$ and Al_2O_3 coatings can improve capacity retention to 165 and 160 mAh/g respectively, compared to only 135 mAh/g for bare $LiCoO_2$, cycling between 2.8V and 4.5V for 20 cycles at C/10 rate [31]. Similarly, Oh et al. have shown that an Al_2O_3 coating improves C/5-rate 50-cycle capacity retention between 3.0-4.4V to 97.5% versus 59% for bare $LiCoO_2$ [26], and Cho et al. have reported an Al_2O_3 coating improvement over bare $LiCoO_2$ from 40% to 4% capacity loss during 70 cycles between 2.75-4.4V at a C/2 rate [27]. Clearly, capacity retention is improved at several different discharge rates for the Al_2O_3 coating on $LiCoO_2$. Moreover, several groups have shown superior cycling performance for ZrO_2 coated $LiCoO_2$ cycled between 2.75-4.4V; Y. Kim et al report negligible capacity fade during 70 cycles at C/2-rate compared to only 59% capacity retention after 30 cycles for bare $LiCoO_2$ [24], and Fey et al. report retention of 80% of initial capacity after 90 cycles at C/5-rate contrasted with only 12 cycles for bare $LiCoO_2$ and 64 cycles for TiO_2-coated $LiCoO_2$ [29]. In the larger voltage range of 3.0-4.8V, J. Kim et al. have studied several metal phosphate coatings on $LiCoO_2$, including $AlPO_4$, $FePO_4$, $SrHPO_4$, and $CePO_4$ [34]. They find that all four coating materials improve the initial discharge capacity as well as capacity retention over 50 cycles at C/10-rate. Specifically, $AlPO_4$ coating retains 65% of its initial discharge capacity after 50 cycles, compared to 39% for $CePO_4$ coating and 17% for $SrHPO_4$ coating over 50 cycles, and negligible discharge capacity after 33 cycles

for $FePO_4$ coating and 22 cycles for bare $LiCoO_2$. Unmistakably, the improvements in capacity retention due to coating the $LiCoO_2$ are drastically increased when cycling with higher upper voltage limits.

Many researchers have explained the increased capacity retention of coated $LiCoO_2$ cathodes by the correlation with reduced cobalt dissolution in the electrolyte. For uncharged $LiCoO_2$, the application of an Al_2O_3 coating decreases the cobalt dissolution by 60% over one week soaking in electrolyte [26]. Furthermore, coating effects are more dramatic at high-temperature or charged conditions. While a ZrO_2 coating on $LiCoO_2$, charged to 4.4V, reduces cobalt dissolution from 260pm to 30ppm at room temperature, at 90C it is reduced from 1330ppm to 200ppm, factors of 9 and 7 respectively [24]. After charging to 4.8V, the reduction is more pronounced; the ZrO_2 coating lowers cobalt dissolution by a factor of 17 from 20,000ppm to 1200ppm [24]. Under the same conditions, $LiCoO_2$ coated with SiO_2, B_2O_3, TiO_2, and Al_2O_3 show similar reduction effects, the level of which corresponding with their degree of improvement in capacity retention; ZrO_2 demonstrated the greatest enhancement in both areas. In studying various metal phosphate coatings on $LiCoO_2$, J. Kim et al. also find that the coating material $AlPO_4$ gives the best capacity retention and also shows the least cobalt dissolution of ~100ppm after 50 cycles to 4.8V, compared with 10,000ppm for bare $LiCoO_2$ [34]. However, the other coatings they tested ($FePO_4$, $SrHPO_4$, and $CePO_4$) did not fit the same trend between capacity retention and cobalt dissolution, suggesting that other factors contribute to capacity fade as well.

In addition to electrochemical improvement, some coatings show enhanced safety in terms of better thermal stability than $LiCoO_2$ in a charged state. For example, Oh et al. have shown that an Al_2O_3 coating on $LiCoO_2$ will increase the peak temperature for the exothermic oxygen evolution reaction to 280°C, from 263°C for bare $LiCoO_2$ charged to 4.4V [26]. Similarly, Cho et al. report an increase in the onset temperature of this reaction in a 4.3V-charged state to 230°C for $AlPO_4$-coated $LiCoO_2$, an improvement over onset at 190°C and 170°C for Al_2O_3-coated and bare $LiCoO_2$, respectively [35]. Furthermore, in 12V-overcharge tests when separator melting induces a short circuit, the bare and Al_2O_3-coated $LiCoO_2$ battery cells undergo thermal runaway, reaching temperatures as high as 500°C, while the $AlPO_4$-coated $LiCoO_2$ only reaches ~60°C [35]. While thermal analyses are not available for many of the other coating chemistries on $LiCoO_2$, Omanda et al. report a SiO_2-coated $LiNi_{0.8}Co_{0.2}O_2$ which actually lowers the exothermic reaction onset temperature at 4.3V by 10°C, but does in fact decrease energy released to 45% of that from the bare material [36]. In general, the level of thermal stability enhancement is highly dependent on the specific coating material.

In order to thoroughly understand these chemical and thermal effects, the coating microstructure and interaction with the host particle have been studied. In most cases, x-ray diffraction shows no additional peaks due to the coating material, due to coating thicknesses typically less than 100nm [25, 29, 31, 33, 34, 36-38]. However, Fey et al. find that ZrO_2 coating causes an increased c parameter compared to bare $LiCoO_2$, and they suggest the formation of a substitutional compound such as $Li_xZr_yCo_{1-y}O_{2+0.5y}$ [29]. Only J. Kim et al. find XRD evidence of a second phase with $CePO_4$-coated $LiCoO_2$, but

they attribute this data to large portions of $CePO_4$ material separate from the $LiCoO_2$ surface [34].

Since XRD studies typically yield little insight, coating layers have also been studied by high-resolution transmission electron microscopy (TEM). Fey et al. find a mechano-thermal TiO_2 coating layer of 60nm thickness which gives an ESCA signal of 1 at.% at the surface, decreasing to 0.5 at.% or less at 60nm from the surface [29]. Cho et al. find a unevenly-textured $AlPO_4$ coating layer of 10nm thickness, but report that a P_2O_5 coating produces a smooth, uniform particle texture [37]. J. Kim et al. correlate the level of coverage with coating particle size; for example, $FePO_4$ and $AlPO_4$ nanoparticles smaller than 20nm showed more uniform coverage in 50nm- and 20nm-thick layers than $CePO_4$ and $SrHPO_4$ nanoparticles of 40nm and 100nm diameter [34]. In their case, the coating nanoparticle morphology does not necessarily match before and after the coating procedure. Miyashiro et al. use a spray-coating process with 10nm-diameter ZrO_2 particles, which stack up to produce a 150nm uniform coating layer on $LiCoO_2$ [39]. Most coatings show similar characteristics to the aforementioned materials, with variation based on coating material and application process.

Further understanding can be gained from the charge voltage characteristics of bare and coated cathode materials, since the presence or absence of voltage plateaus that indicate phase transitions or atomic ordering may indicate changes in the $LiCoO_2$ crystal structure and composition. Specifically, many authors believe that the suppression of the hexagonal-to-monoclinic transition near x=0.5 is the reason for improved capacity

retention in coated cathode materials [27, 29, 40]. In differential capacity plots, coatings of $ZrTiO_2$ [29] and boehmite [40] cause the disappearance of hexagonal-monoclinic peaks near 4.2V after the first cycle, which might indicate that this phase transition is suppressed due to the coating. J. Kim et al. have studied metal phosphate coatings on overstoichiometric $LiCoO_2$ which does not show the ordering transition at x=0.5; remarkably, only the $AlPO_4$-coated sample displays this transition, although no remark is made about this phenomena in the literature [34]. In contrast, Chen and Dahn find that Al_2O_3 coating suppresses the ordering transition in $LiCoO_2$, however, no explanation is given [28]. In general, changes in the voltage profile are highly dependent on the individual coating material.

The coating material with the most outstanding performance is $AlPO_4$, as reported by Cho et al. [33-35, 41-45]. Specifically, they have found that the $AlPO_4$ coating increases the initial reversible discharge capacity from 200 mAh/g to 220 mAh/g with a 4.8V upper voltage limit, using a C/10 rate [45], in contrast to the decrease in initial discharge capacity due to ZrO_2 and TiO_2 coatings [29]. Importantly, capacity fading is drastically reduced; after 50 cycles at a 1C rate with a 4.8V cutoff voltage, the $AlPO_4$ coating retains ~150 mAh/g in capacity while the bare material declines to ~0 mAh/g, as shown in Figure 3 [46]. In addition, the $AlPO_4$ coating reduces Co dissolution by almost two orders of magnitude under these cycling conditions, compared to the bare material [46]. Moreover, thermal stability is improved. In a charged state of 4.7V, $AlPO_4$-coated $LiCoO_2$ increases the onset temperature for electrolyte oxidation from 187°C to ~220°C and reduces by a factor of ten the overall heat evolution, shown in Figure 4, which

accelerates oxygen evolution from the electrode [41]. Therefore, the risk of thermal runaway is reduced and safety is improved. Overall, the superior performance of the $AlPO_4$ coating made it the most attractive subject for investigation in this study.

The actual reason behind the performance improvements of $AlPO_4$ and other coatings is still a subject of debate. Cho et al. first suggested that the coating layer suppressed harmful phase transitions by constraining the particle against lattice parameter changes, depending on the fracture toughness of the coating material [25]. In contrast, Chen and Dahn argued that since no new phase transitions or volume changes occur between 4.2V and 4.5V, the suppression of phase transitions could not explain the difference in performance between cells cycled to those two upper voltage limits, and they find experimentally that performance enhancement is independent of fracture toughness of the coating [28, 47]. They reason that the impedance growth on the particle surface is instead due to reaction between surface species from exposure of $LiCoO_2$ to air or moisture and components of $LiPF_6$ electrolytes, and this effect can be minimized by grinding to form fresh surfaces or heating above 550°C [47]. Liu et al. also agree that the coating layer does not suppress phase transitions up to 4.5V, from an XRD study of Ti-doped and TiO_2-coated $LiNi_{0.8}Co_{0.2}O_2$ [48]. However, Fey et al. support Cho's hypothesis with slow-scan cyclic voltammetry data with an upper voltage limit of 4.4V, which shows that the phase transition peaks are suppressed to varying degrees that are dependent on coating material [40, 49]. Furthermore, Cho et al. also find that $AlPO_4$ coating improves performance with 4.6V and 4.8V upper voltage limits for cycling, at which O3 to H1-3 transition has occurred and Co dissolution is more prominent [45].

Specifically, the $AlPO_4$ coating reduces the first-cycle Co dissolution at 4.8V by a factor of ~11, improves Li diffusivity by one order of magnitude by the 50th cycle compared to bare $LiCoO_2$ as found by GITT, and improves capacity retention as described earlier [45]. Therefore, it follows that the coating layer may protect the $LiCoO_2$ surface from attack by electrolyte species, Co dissolution, and impedance growth at higher voltage limits.

The relative importance of coating structure and surface transport processes on improvement of $LiCoO_2$ electrochemical and thermal performance is not well understood. How does the coating affect the electronic resistance and charge-transfer processes into the $LiCoO_2$? By what mechanism do Li^+ ions travel through the coating layer, and how does it differ from a Li_2CO_3 surface layer found on bare $LiCoO_2$? How does the structure of the coating dictate its properties? To gain more insight on the relationship between occurring on coated $LiCoO_2$, this work aims to correlate the micrometer- and nanometer-scale structure of $AlPO_4$-coated and bare $LiCoO_2$ with its electrochemical performance and transport properties through examination of its voltage profile and impedance spectra. Quantitative three-dimensional surface details are studied with atomic force microscopy. Furthermore, transmission electron microscopy with energy dispersive x-ray spectroscopy is used to study the coating microstructure and elemental distribution, while x-ray photoelectron spectroscopy reveals details of the surface composition. These structural features may be compared with the electronic and ionic resistances and capacitances of both materials, which are obtained by electrochemical impedance spectroscopy at different lithium contents between the voltage limits of 3.0V and 4.7V.

Figure 3. Capacity retention of bare, Al₂O₃- and AlPO₄-coated LiCoO₂ cathodes in coin
cells with a charge voltage limit of 4.8V (pre-cycled at the rates of 0.1C for the first two
cycles, and 0.2 and 0.5C each for the next two cycles). (J. Cho et al., J. Power Sources,
2005)
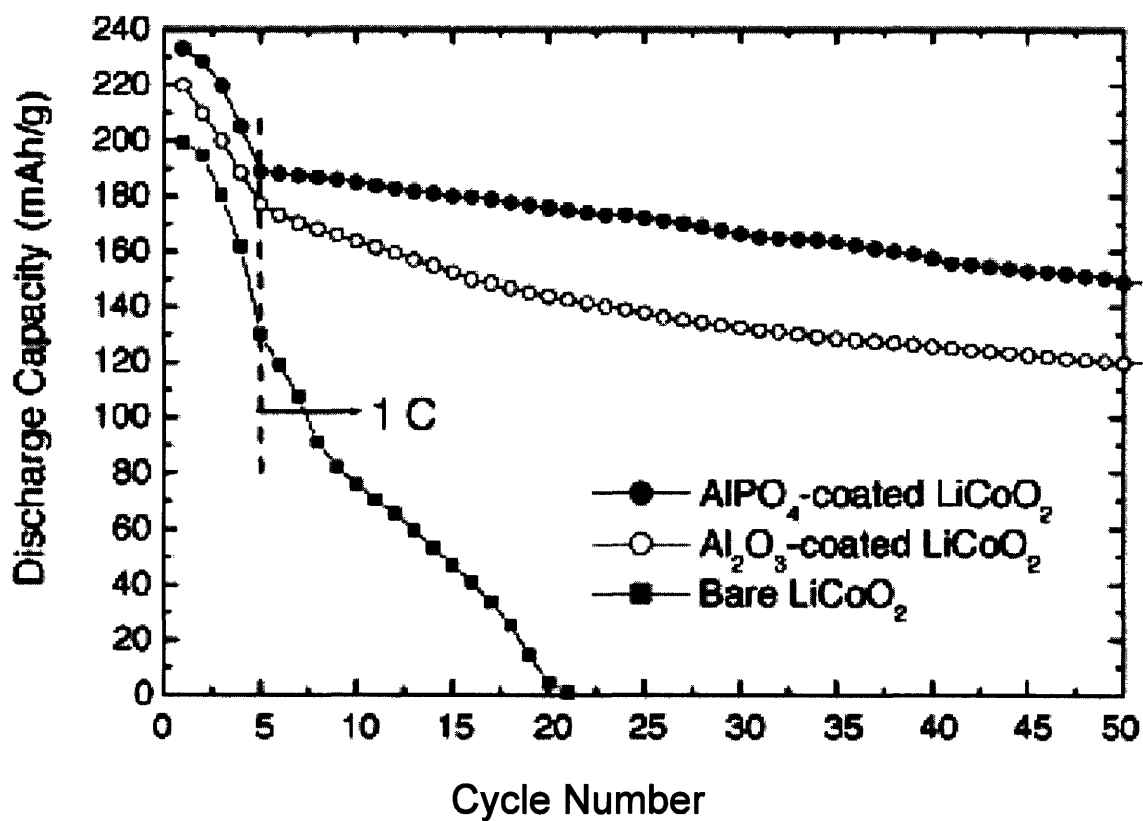
Figure 4. DSC scans of 4.7V-charged positive electrodes containing the bare and AlPO$_4$-coated LiCoO$_2$ with different coating thicknesses. In increasing order of coating thickness, cathodes are labeled P10, P30, and P100. (J. Cho, Electrochim. Acta, 2003)
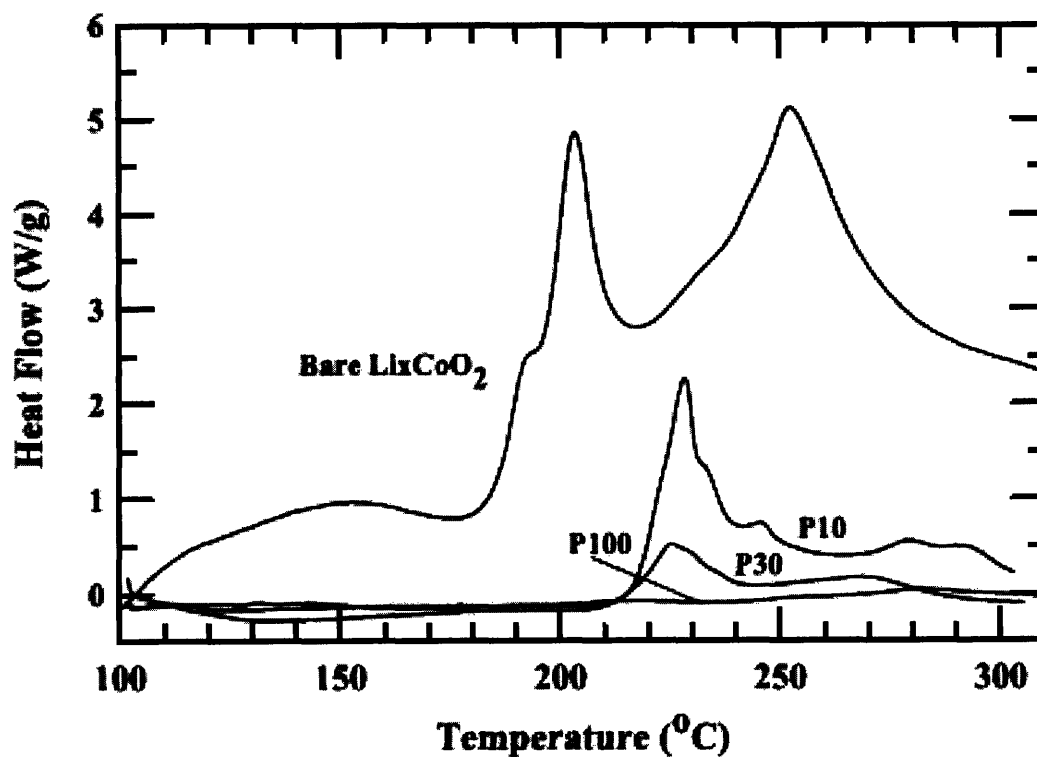
b. EIS studies of Positive Electrode Materials

Several researchers have studied lithium battery positive electrode materials using electrochemical impedance spectroscopy (EIS). This technique involves application of an ac voltage signal to an electrochemical cell at a range of frequencies, and measurement of the ac current response allows calculation of the complex impedance at each frequency. The amplitude of this perturbation must be small so that the response can be assumed to be linear. The impedance data provide information about the different electronic and ionic transport properties occurring within the cell at different time constants, and results are typically modeled by an equivalent circuit consisting of resistors and capacitors in parallel for each physical process represented.

Composite $LiCoO_2$ electrodes in three-electrode cells have been studied using EIS by Barsoukov et al., who describes the important kinetic steps occurring at the positive electrode [50]. At high frequencies above ~50 kHz, ion conduction through the electrolyte and electronic conduction through wires are typically lumped together as solution resistance, and are typically not limiting factors in liquid electrolyte systems. At slightly lower frequencies, ranging from ~750 Hz to 50 kHz, insulating surface layers and then, near 80 Hz, charge transfer of the Li^+ between solvation in the electrolyte and entrance into the particle surface are represented in the impedance data as two semicircles in the Nyquist plot that are often close in peak frequency. This range of data also includes the effects of the electrical double layer which forms at the interface between electrolyte solution and particle surface. At medium-low frequencies around 1 Hz, the effect of electronic resistance in the bulk of the active material particle is seen by a

semicircle. At very low frequencies, a 45-degree sloping line shows the presence of solid-state diffusion of Li^+ in the particle bulk.

Choi et al. have studied lithium transport in $LiCoO_2$ and $LiNiO_2$ composite electrodes utilizing three-electrode cells containing Li reference and counter electrodes. During C/10 galvanostatic charging between x=0.8 and x=0.5, EIS results for Li_xCoO_2 show two semicircles followed by a low-frequency sloping line [44]. The high-frequency arc with peak frequency of ~10 kHz remains nearly constant in magnitude at ~20Ω in this x range, and its temperature dependence yielded an activation energy of 10^{-4} eV, which was too small for charge transfer; therefore it was labeled as inter-particle contact resistance and capacitance [44]. Choi et al. argue that the medium-frequency arc, with peak frequency of ~0.05 Hz, represents absorption of Li^+ ions into the oxide, due to its increase with increasing lithium content [44]. The low-frequency line was assigned to Warburg impedance of Li^+ diffusion.

In addition, Levi et al. have studied Li_xCoO_2 in a three-electrode cell containing Li counter and reference electrodes, as a function of potential between 3.70V and 4.07V during deintercalation in slow-scan cyclic voltammetry [12, 51]. At each open-circuit voltage, their Nyquist data shows a potential-independent high-frequency depressed semicircle with a 10^{-6} F/cm^2 capacitance, which they attribute to surface films on the positive electrode, such as Li_2CO_3, because of its similarity to the response of the solid electrolyte interphase (SEI) on graphite electrodes [12]. For the Li_xCoO_2 study, Levi et al. also find an undepressed medium-frequency semicircle, with peak frequency near 0.2 Hz,

whose diameter decreases from $\sim 10^4 \Omega$ to $\sim 100\Omega$ as voltage increases, and they assign

this feature to interfacial charge transfer of Li^+ ions and electronic conductivity of the

$LiCoO_2$ [12]. The associated capacitance is on the order of mF/cm^2 due to charge

transfer over the high surface area of the porous electrode [12]. Above 3.87V, at low

frequencies near 10 mHz, they report a narrow Warburg diffusion region of solid-state

diffusion and a steep sloping line attributed to capacitance of Li^+ accumulation in the

bulk. They model this behavior with a generalized Frumkin and Melik-Gaykazyan

equivalent circuit, shown in Figure 5, which they developed and fitted for lithiated

graphite in previous studies [12]. From this model, they report a charge-transfer

resistance decrease from 1000Ω to $\sim 100\Omega$ between 3.86V and 4.07V, as well as an

intercalation capacitance C_{int} reflecting the low-frequency spike, which shows a

maximum at the deintercalation plateau voltage of $LiCoO_2$ [12].

Figure 5. Equivalent circuit model developed by Levi et al., including the various time
constants associated with each process. (Levi et al., J. Electrochem. Soc., 1999).
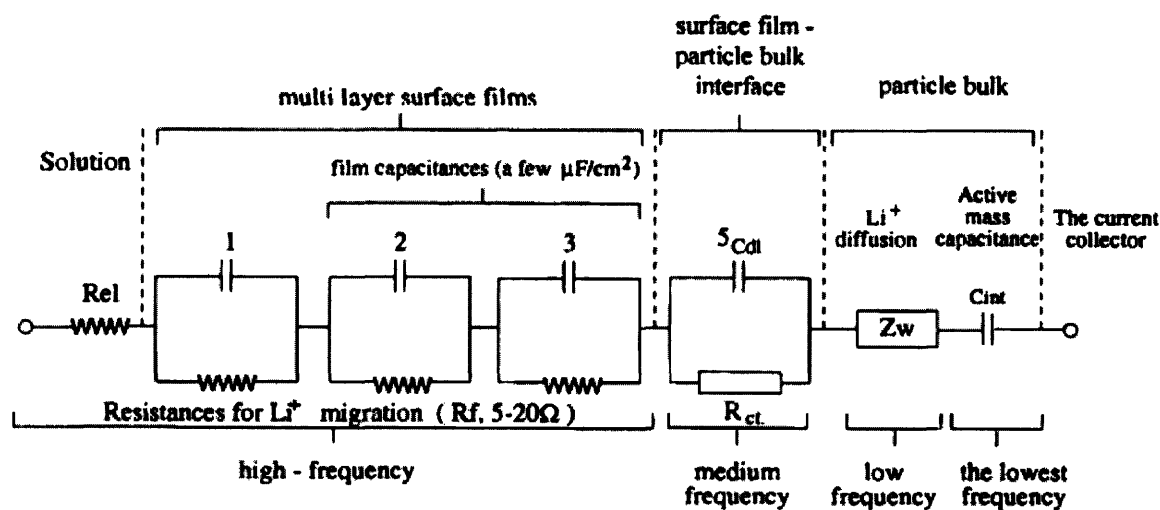
Nobili et al. have also conducted several studies on $LiCoO_2$ using EIS as a function of potential and of temperature [52-54]. Using a T-shaped Swagelok electrochemical cell with Li counter and reference electrodes, they have studied Li_xCoO_2 composite electrodes under potential control between x=1.0 and x=0.7 [52]. Subsequent EIS data yield a potential-dependent low-frequency semicircle with peak near 0.7 Hz, and a relatively potential-independent high-frequency semicircle, which upon closer inspection appears to be a combination of two different semicircles of medium and high frequency. They argue that the low-frequency semicircle represents electronic resistance due to its potential-dependent decrease of three orders of magnitude, which corresponds with the known insulator-metal transition in $LiCoO_2$ [52]. The corresponding electronic capacitance value, possibly explained by electron accumulation in nanometer-size crystallite domains, is ~100 μF [52]. In contrast to previous researchers, Nobili et al. attribute the medium frequency arc around 80 Hz to the charge-transfer process, and the small high-frequency arc near 8 kHz to surface layer resistance, both of which are generally potential-independent in magnitude [52]. At lower x values, the characteristic diffusion spike is seen, similar to the previously reviewed studies.

Nobili et al. further studied the temperature dependence of the EIS spectra of $LiCoO_2$ [53]. Between 0°C and 30°C, overall impedance increases with decreasing temperature. As temperature decreases, the poorly-defined high and medium frequency semicircles tend to separate into distinct arcs. Therefore they use the equivalent circuit given in Figure 6, taken from that developed by Bruce and Saidi [55], to extract resistance values from the EIS data, which are shown in Figure 7. Arrhenius plots of electronic

conductivity from the low-frequency semicircle show the thermally-activated nature of this feature, supporting its designation as the electronic conductivity. The resistance and capacitance of the high-frequency semicircle are relatively constant with potential, with values of $\sim 3\Omega$ and $\sim 1 \times 10^{-5}$ F respectively, and indicate the presence of a stable passivating layer [55]. With decreasing temperature from 24°C to 1°C, this resistance increases slightly from 3Ω to 20Ω, and capacitance gives no clear trend. Nobili et al. consider the initial decrease of charge-transfer resistance with increasing potential to stem from the closely spaced semicircles at high lithium content, and they regard charge-transfer to be constant at $\sim 250\Omega$ as a function of lithium deintercalation. Charge-transfer resistance also increases from $\sim 250\Omega$ at 24°C to $\sim 700\Omega$ at 1°C. Furthermore, this charge-transfer process appears to have a single activation energy at different potentials, and its potential independence is explained by the fact that when an ion is accepted into the host matrix, the corresponding electron does not combine with that ion specifically, but rather enters the host matrix for charge neutrality; the energy of this process does not depend on the potential of the host matrix, unlike the electronic energy of a metal host electrode [55]. The corresponding double-layer capacitance is reported to be $\sim 1.5 \times 10^{-5}$ F, slightly increasing as temperature decreases to 1°C. Nobili et al. find similar trends to support their interpretation when studying Mg-doped $LiCoO_2$ [54].

While the 45-degree sloping line measured by EIS at low frequencies reflects solid-state diffusion, it is at those low frequencies that reliable data points are most difficult to obtain, due to low-frequency noise and the long period of time required to record a

reliable data point. Another method frequently used for measuring the solid-state diffusion properties is galvanostatic intermittent titration technique.

Figure 6. Equivalent circuit used by Nobili et al., and developed by Bruce and Saidi. (Nobili et al., J. Phys. Chem. B, 2002)
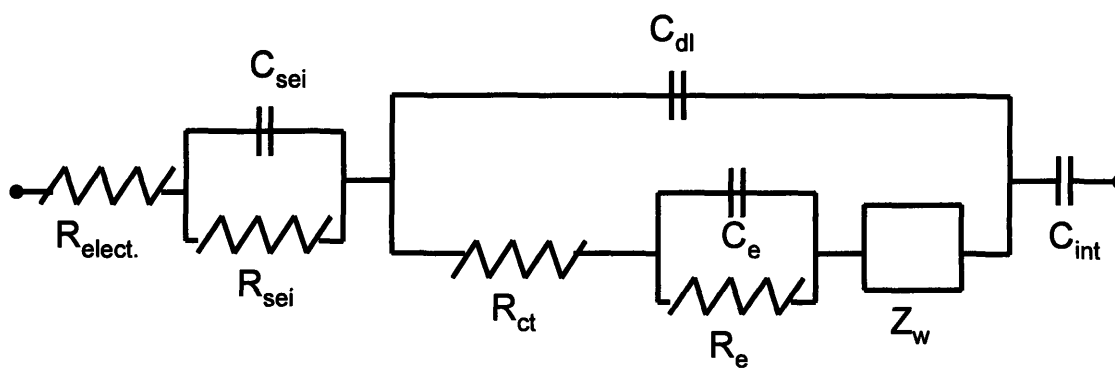
Figure 7. Plots of (a) electronic resistance, R_e, (b) charge-transfer resistance, R_{ct}, and (c) surface layer resistance (R_{sei}) as a function of deintercalation degree, x, at different temperatures, as reported by Nobili et al. (Nobili et al., J. Phys. Chem. B, 2002)
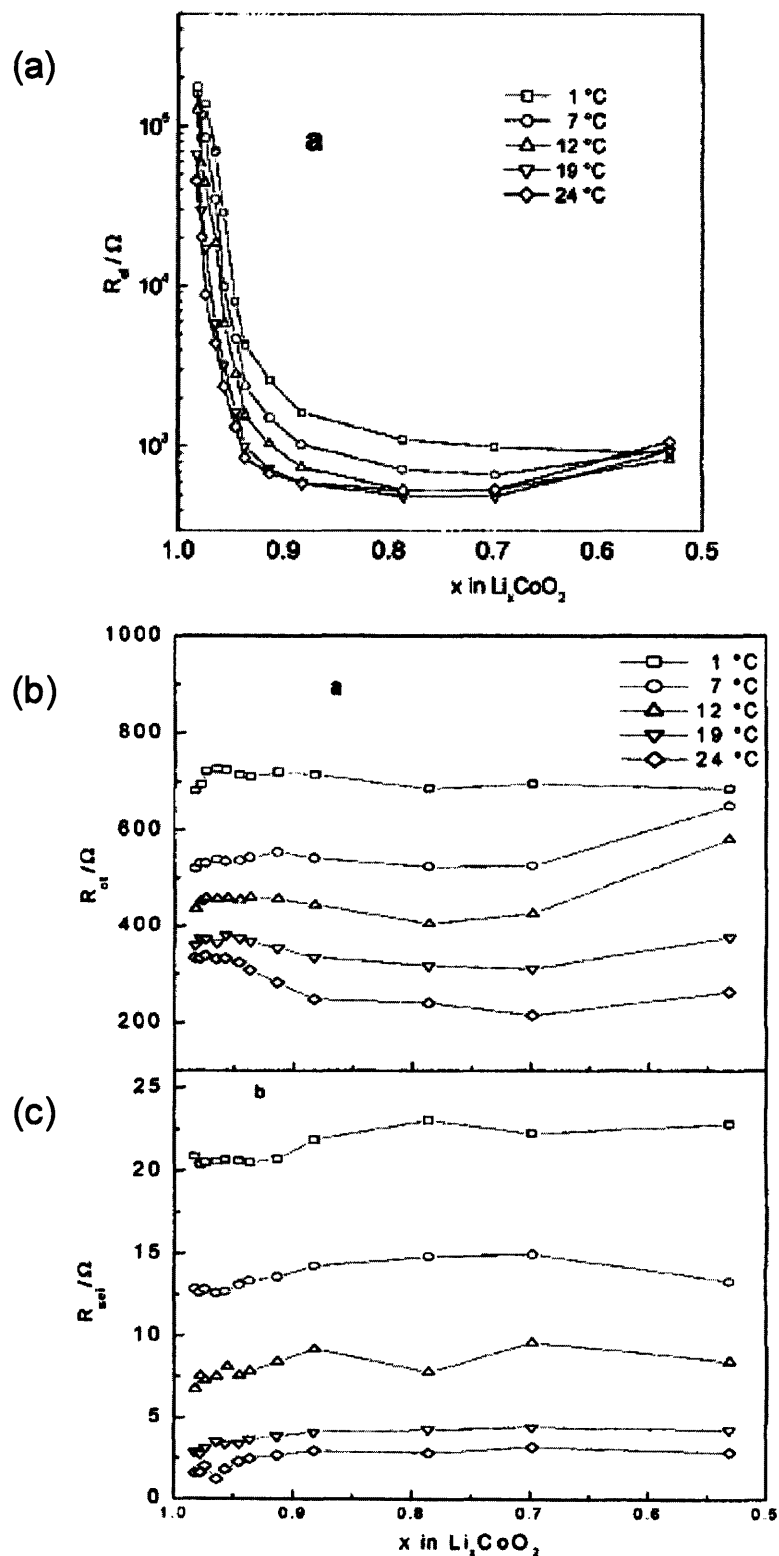
c. Galvanostatic Intermittent Titration Technique

First developed by Weppner and Higgins, galvanostatic intermittent titration technique (GITT) is a method for measuring the chemical and component diffusion coefficient of solid mixed-conducting electrodes [56]. In this technique, a constant current is applied to the electrochemical cell for a time period τ while measuring the potential E_t, after which the current is stopped and the cell is allowed to reach a new equilibrium potential E_s, at which the surface composition becomes homogeneous by diffusion of the mobile ion. If one can assume that the molar volume does not change with composition and that the system can be modeled as semi-infinite diffusion ($\tau << L^2/\widetilde{D}$), the following equation, derived from Fick's diffusion equation, can be used to calculate the chemical diffusion coefficient from the measured parameters:

$$\widetilde{D} = \frac{4}{\pi}\left(\frac{V_M}{SFz_i}\right)^2 \left[I_0\left(\frac{dE}{d\delta}\right)\bigg/\left(\frac{dE}{d\sqrt{t}}\right)\right]^2$$

where V_m is the molar volume of the electrode, S is the area of the electrode-electrolyte interface, I_0 is the applied current, and F is Faraday's constant. $d\delta$ represents the change in stoichiometry of the sample, t is the length of the current pulse, and L is the electrode thickness. In order for this equation to be valid, the given derivatives of E and the diffusivity must be assumed constant for each perturbation [57].

Because $LiCoO_2$ is a mixed conductor, such that both electrons and ions are mobile, there develops an electric field within the solid which accelerates the slower species (in this case, Li^+) and slows the faster species (electrons) in order to maintain charge neutrality. Also calculable by GITT, the thermodynamic enhancement factor, W, quantifies this

effect as the ratio between field-enhanced (chemical) diffusion, $\widetilde{D}_{Li+}$, and random (component) diffusion, D_{Li+}. When the material is mainly an electronic conductor, the electronic transference factor, $t_e \approx 1$ [58, 59], and W can be calculated as follows:

$$W = t_e \frac{\partial \ln a_{Li}}{\partial \ln c_{Li}} = -\frac{F\delta}{RT}\frac{dE}{d\delta}$$

Component diffusion, which represents the self-diffusion of the mobile constituent by random motion without influence of the concentration gradient, is then related to chemical diffusion by

$$\widetilde{D}_{Li+} = W\, D_{Li+}$$

Using GITT, Choi et al. have measured the $\widetilde{D}_{Li+}$ of Li_xCoO_2 in the x range of 0.5-0.75 in three-electrode cells using C/10 charge rate, reporting slight increase with decreasing lithium content, with a value on the order of 10^{-8} cm^2/s [44]. They report a similar trend for component diffusivity, D_{Li+}, nearly constant at 10^{-11} cm^2/s. Component diffusivity represents the random motion of lithium ions in the absence of a concentration gradient, and Choi et al. suggest that this parameter is dependent on the number of available lattice sites in the lithium layer [44]. Jang et al. have studied $\widetilde{D}_{Li+}$ for Li_xCoO_2 between $0.45 < x < 0.7$ using potentiostatic intermittent titration technique (PITT), and they also find that $\widetilde{D}_{Li+}$ increases between 0.7 and 0.5, with a value near 10^{-10} cm^2/s [59]. However, they find that $\widetilde{D}_{Li+}$ experiences two minima surrounding a maxima at x=0.5 which corresponds to features of the order-disorder transition of $LiCoO_2$ in the differential capacity plot. They also report that the sharpness of the peaks in the differential capacity plot corresponds with the intensity level of the minima of $\widetilde{D}$ vs. potential.

Hong et al. have also studied the dependence of D_{Li+} on lithium content x in Li_xCoO_2 [60]. Using a Panasonic type CGR18650 Li-ion cell with 2-hour current pulses at a C/20 charge rate at 35.7°C and 65.7°C, they report a local maxima of 10^{-9} from $10^{-7.9}$ cm^2/s in chemical diffusivity, $\widetilde{D}$, at x=0.5 due to the order-disorder phase transition in Li_xCoO_2, although they do not see pronounced minima surrounding this peak. This discrepancy with the previous study may be due to differences in cell construction and lithium content resolution. They find that the thermodynamic enhancement factor, W, reaches a maximum near x=0.5, and that these trends for both $\widetilde{D}$ and W are reversible upon discharge. Hong et al. also found that the peak in both $\widetilde{D}$ and W at x=0.5 decreased at 65.7°C [60], which agrees with the phase diagram reported by Reimers and Dahn, stating that the monoclinic distortion at x=0.5 is thermodynamically favorable only in the temperature range -10°C $\leq$ x $\leq$ 60°C [1, 2].

GITT has also been used to characterize other oxide cathode materials [12, 61, 62], which may lend insight into the behavior of $LiCoO_2$. Levi et al. have correlated the minima in $\log \widetilde{D}$ vs. potential for Li_xNiO_2 and $Li_xCo_{0.2}Ni_{0.8}O_2$ with attractive interactions between the intercalations species, with especially sharp peaks for first-order phase transitions [12]. They note that during a two-phase reaction, the diffusion coefficient may reflect long- and short-range interactions between intercalation species, which differs from a solid solution which achieves full equilibrium throughout the bulk of the electrode. Therefore, the accuracy of GITT measurements in a two-phase region depends on the magnitude of the pulse current used, but for a material with a single-phase solid solution

during deintercalation, values obtained from GITT are well-defined[12]. They also find

small minima in $\log \widetilde{D}$ corresponding to order-disorder transitions in the material, which

indicate a super-lattice pattern due to short-range repulsive interactions [12].

d. AFM Studies with Electrical Measurements

Several researchers have employed the atomic force microscope (AFM) in conducting

nanoelectrode experiments [7, 63-67]. Because an AFM cantilever tip radius is usually

~20nm, using it as a nanoelectrode can enable measurement of conductivity or

impedance variations across the surface of a single particle, or similar microscale

substrate. There are two general methods for impedance measurement with the AFM:

scanning impedance microscopy and single-point impedance frequency sweeps.

Scanning impedance microscopy involves choosing a single frequency for the AC bias

and scanning the tip across a particular square area of the sample, resulting in a 3-

dimensional map with the color scale corresponding to varying impedance values.

Single-point measurements hold the tip stationary while a frequency sweep is conducted.

A conductive tip must be used, and tip selection depends on the nature of the sample. For

soft samples such as polymer, a silicon tip with a 40-nm gold coating can be used [64];

for harder samples that may wear down a gold coating, a doped diamond-coated probe is

more suitable [66, 67]. The tip spring constant must be relatively high (>10 N/m) to

enable application of high tip-sample forces (~μN) in order to increase contact area and

data reproducibility [67] . With a doped diamond coated tip, O'Hayre et al. find a tip

resistance of ~3000 Ω, but they report this value to be negligible compared with contact

resistance [67]. R. Shao et al. used a gold-coated tip with a ZnO varistor sample, and they report a 40Ω contact resistance for an undamaged tip; for a damaged tip this resistance rises to ~100 MΩ and impedance becomes dependent on frequency [7]. Because of possibly large impedances caused by this experimental aspect, this technique is often limited at the high impedance range.

Other issues to consider are sample drift and measurement time. O'Hayre et al. conduct several frequency sweeps within a measurement area and use this data to choose the critical frequencies for the sample [66]. Next, full-area single-frequency scans are conducted, pausing for several seconds at each pixel for an impedance measurement. Naturally, longer pauses at each pixel will allow good contact to be established and reliable data to be recorded; however, too much time per pixel leads to sample drift issues and unreasonably long measurement times for the entire sample area.

II. Experimental

The active electrode materials, both bare and AlPO$_4$-coated LiCoO$_2$, were prepared by J. Cho and coworkers at the Kumoh National Institute of Technology. The LiCoO$_2$ was prepared from stoichiometric amounts of Co$_3$O$_4$ and Li$_2$CO$_3$ at 1000°C for 4 hours in an oxygen stream. The AlPO$_4$-nanoparticle solution was prepared by slowly dissolving Al(NO$_3$)$_3$·9H$_2$0 and (NH$_4$)$_2$HPO$_4$ in distilled water until a white AlPO$_4$-nanoparticle suspension was observed. LiCoO$_2$ was added to this coating solution and mixed thoroughly for 5 minutes. The slurry was dried in an oven at 130°C for 6 hours and heat-treated at 700°C for 5 hours [35].

Electrochemical studies were carried out with 2016 coin-type cells, shown schematically in Figure 8. The positive electrode began with a slurry comprised of bare or AlPO$_4$-coated LiCoO$_2$ powder, poly-vinylidene fluoride (PVDF), and Super P carbon black in an 80:10:10 weight ratio, which was ground with a mortar and pestle to break up large agglomerations. A few millileters of N-methyl pyrrolidone (NMP) solution was added to the powder mixture until a viscous slurry was formed. The slurry was cast onto Al foil using a doctor blade and dried under vacuum at room temperature overnight, and subsequently dried under vacuum at 120°C for 8-10 hours. 15-mm diameter electrode disks were punched and re-dried under vacuum at 120°C for at least 30 minutes before being kept in an argon-filled glovebox. Coin cells were constructed inside the argon-filled glovebox, with oxygen levels below 5ppm, using a 16-mm-diameter lithium metal foil negative electrode and the composite positive electrode separated by two polypropylene microporous separators (Celgard) of 17-mm diameter. The electrolyte

used was 1M $LiPF_6$ in a 1:1 weight ratio ethylene carbonate (EC): dimethyl carbonate (DMC) solvent (Merck and LithChem International). Assembled coin cells were allowed to soak overnight before undergoing electrochemical testing on a Solartron 1470 battery tester and a Solartron 1290 frequency response analyzer, as well as a Solartron 1470E/1455 BTU/FRA combination. Electrical connections between the experimental cell and the Solartron instrument are illustrated in Figure 9.

Galvanostatic charging and discharging occurred at a C/50 or C/100 rate (5.48 mA/g or 2.74 mA/g). Electrochemical impedance spectra were obtained using a 10mV amplitude perturbation in a frequency range of 500 kHz to 1 mHz. Each impedance test was conducted after galvanostatically charging the coin cell at C/100 or C/50 to particular lithium contents, at which the cell was allowed to rest for 2 hours to reach equilibrium at open circuit voltage before beginning the EIS measurement. Similarly, GITT measurements were conducted using 1-hour current pulses at C/50 rate and 2-hour equilibration periods. Electrode thickness, L, was taken to be the diameter of a $LiCoO_2$ particle, 10μm.

In preparation for scanning electron microscopy (SEM), loose particles of $LiCoO_2$ were sprinkled onto silver paint on an aluminum stub and imaged using a JEOL 6320FV field-emission SEM. In addition, ~3mg of $LiCoO_2$ particles were pressed between two disks of gold foil under 5000 psi on a Carver hydraulic press for imaging by atomic force microscopy (AFM). After separating the two disks, each surface contained embedded

LiCoO$_2$ particles which were imaged using silicon nitride DNP cantilevers on a Veeco Enviroscope AFM.

Transmission electron microscopy (TEM) was used to examine the high-resolution cross-sections of the AlPO$_4$ coating. Microtomed TEM samples were prepared by embedding the coated LiCoO$_2$ powder in a clear epoxy resin and then microtoming slices of 30-nm thickness. These cross-sections were examined on a JEOL 2010 microscope under an accelerating voltage of 200kV.

To study the elemental distribution across the coating, the LiCoO$_2$ particles were cooled with liquid nitrogen and fractured in a controlled manner to produce thin fracture planes of single crystals for imaging in a VG HB603 scanning transmission electron microscope (STEM) with energy dispersive x-ray (EDX) capabilities. This sample preparation method was chosen because microtomed samples were unsuitable due to the sample drift caused by damage to the epoxy resin framework under the STEM beam.

X-ray photoelectron spectroscopy (XPS) was conducted using a Kratos AXIS Ultra Imaging X-Ray Photoelectron Spectrometer with monochromatized Al Kα x-rays, operated at 2 kV. Samples were prepared by pressing a small amount of powder onto copper tape on the sample holder. An argon ion gun source operated at 150W was used for depth profiling.

Figure 8. (a) Photograph of sealed coin cell. (b) Schematic of coin cell assembly.

(a)

(b)

Current collector

Gasket

Li metal anode

Electrolyte

Two porous separators

Electrolyte

Composite cathode

Steel spacer

Current collector
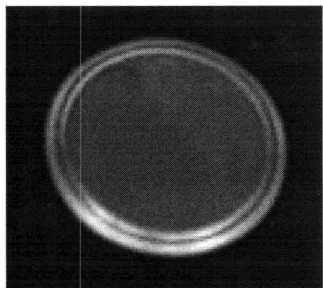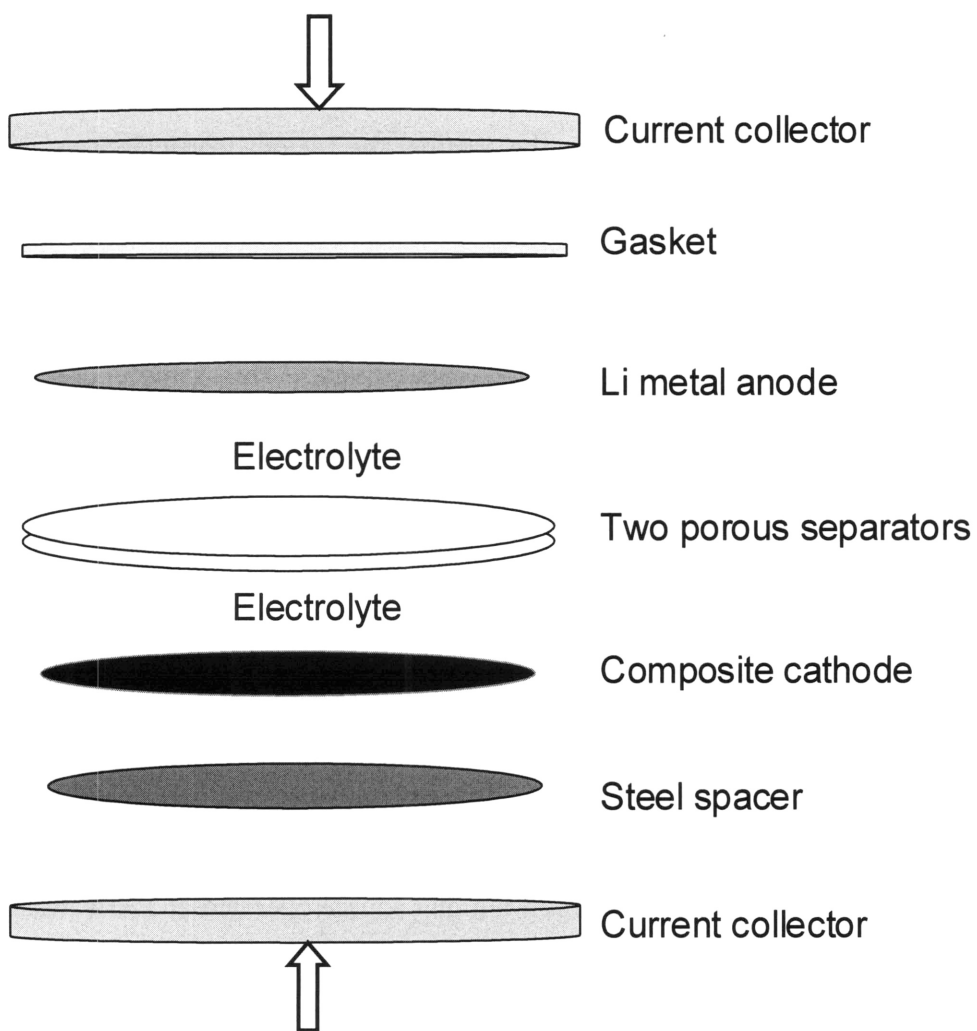
Figure 9. Schematic of test cell connections to Solartron 1470 battery tester, as indicated in Solartron User Guide.
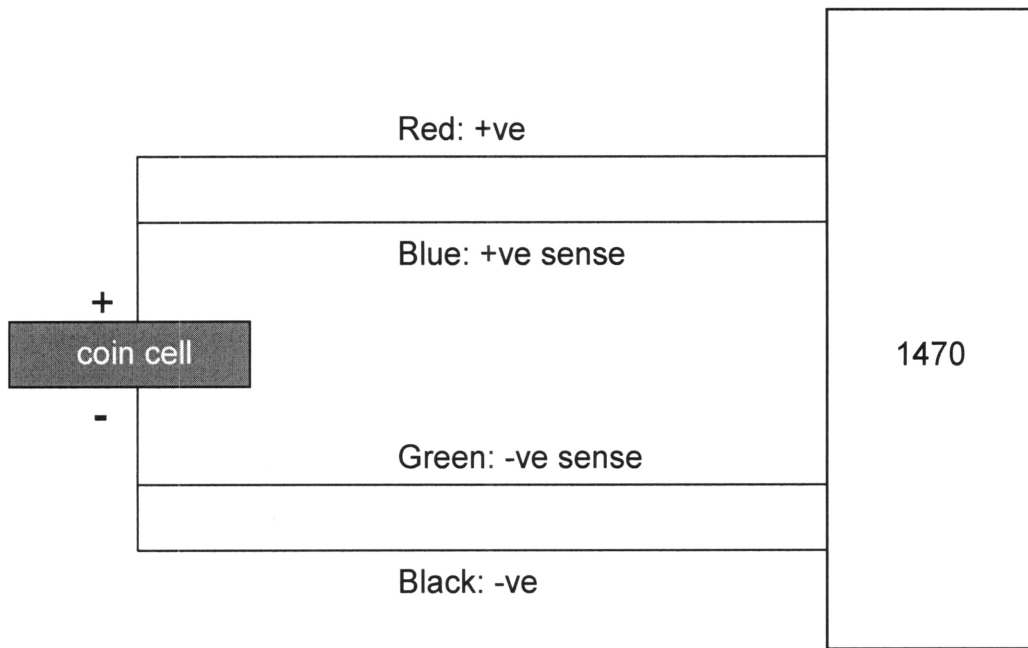
III. Electrochemical Studies of $AlPO_4$-Coated and Bare $LiCoO_2$

a. Galvanostatic Measurements

The galvanostatic voltage profile for both bare and $AlPO_4$-coated $LiCoO_2$ between 3.0V and 4.7V at a charge rate of C/50 is presented in Figure 10. The first plateau near 3.93V is characteristic of the two-phase region for $0.75 < x < 0.96$, and the plateau voltage is approximately 0.02V higher for the coated material. The voltages of these plateaus are shown clearly as peaks in the differential capacity plot of Figure 11, which also emphasizes the sharpness of the deintercalation peak for the coated $LiCoO_2$. It is important to note that, while both samples came from the same parent sample of $LiCoO_2$, only the coated sample shows the two small plateaus near x=0.5 corresponding to the hexagonal-monoclinic distortion of lithium-vacancy ordering. The bare sample lacks this feature, indicating it is overstoichiometric $LiCoO_2$ [21]. This connection between monoclinic distortion absence and overstoichiometry has been reported by Levasseur et al., who find that 10% excess lithium is sufficient to suppress the distortion [21]. Because the extra lithium lies in the transition metal layer, enough structural perturbations are present to prevent the Li/vacancy ordering in the lithium layer at x=0.5 [21]. Furthermore, the bare sample shows only one sloping plateau in the high voltage region, shown by a broad peak in Figure 11 at approximately 4.55V, while the $AlPO_4$-coated sample clearly shows two voltage plateaus at 4.55V and 4.63V, shown as sharper peaks in Figure 8. These two plateaus correspond to the transitions from the O3 to the H1-3 phase, and the H1-3 to the O1 phase, respectively [6, 68]; they are reversible upon discharge in the coated material. However, stoichiometric $LiCoO_2$ prepared in the Electrochemical Energy Lab also lacks these two sharp peaks in Figure 11, having a

similar broad peak to the bare Li-rich $LiCoO_2$, while sustaining the features of lithium-vacancy ordering. Dahn et al. report a similar effect of an Al_2O_3 coating on $LiCoO_2$ in the high-voltage region, in which the plateaus at 4.55V and 4.63V occur reversibly on the discharge in only the coated $LiCoO_2$ [68]. Cho et al. find well-defined monoclinic distortion features on $AlPO_4$-coated $LiCoO_2$ voltage profiles, but not bare or Al_2O_3-coated $LiCoO_2$ [35].

Figure 10. Comparison of voltage profiles between bare and $AlPO_4$-coated $LiCoO_2$ with an upper voltage limit of 4.7V, charged at C/50 rate. The absence of the lithium vacancy ordering feature at x=0.5 indicates the bare $LiCoO_2$ is lithium-rich. $AlPO_4$-coated $LiCoO_2$ shows two distinct plateaus at 4.53V and 4.62V, as well as a higher OCV than bare $LiCoO_2$.
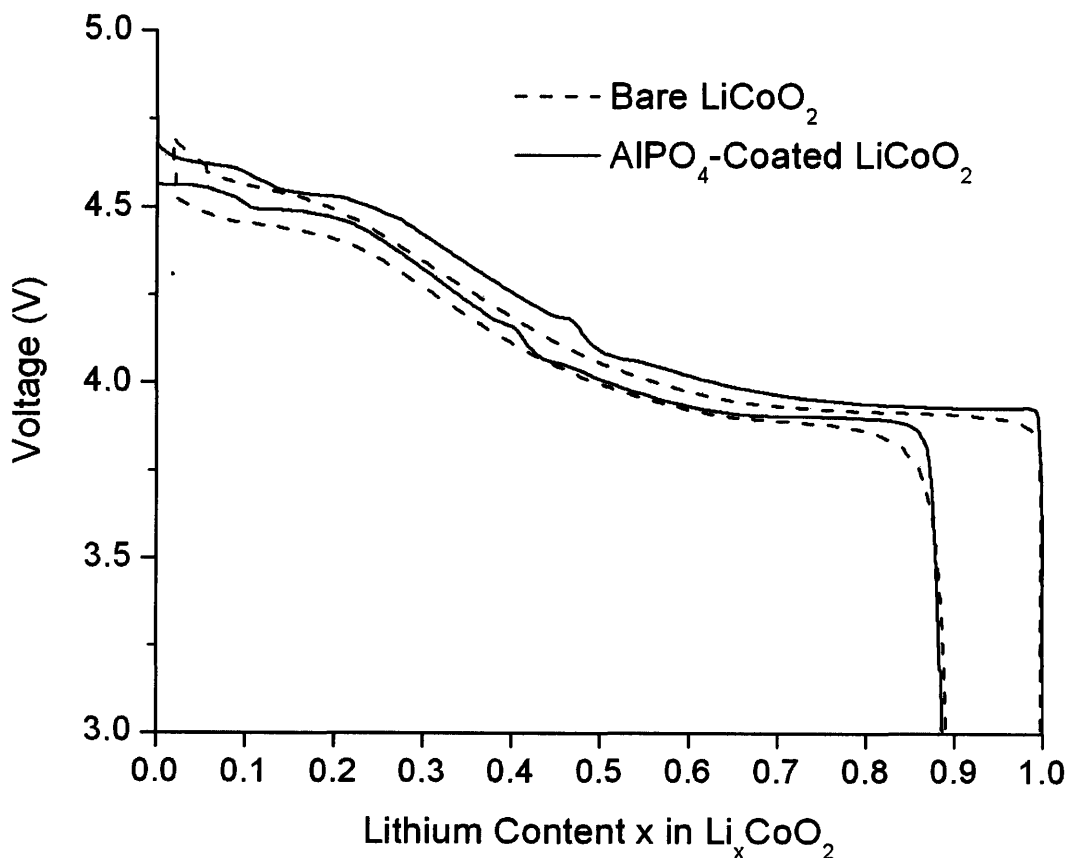
Figure 11. Galvanostatic measurements at C/50 between the voltage limits of 3.0V and 4.7V yield differential capacity plots for bare and $AlPO_4$-coated $LiCoO_2$, compared with stoichiometric $LiCoO_2$. The coated material produces a higher plateau voltage of 3.93V than the bare at 3.91V. The stoichiometric and $AlPO_4$-coated materials show the hexagonal-monoclinic distortion near x=0.5, and the $AlPO_4$-coated material alone shows the O3 to H1-3 transition and H1-3 to O1 transition plateaus, at 4.53V and 4.62V respectively. Bare and stoichiometric $LiCoO_2$ show a more sloping plateau at 4.55V, corresponding to a broader peak in the differential capacity plot.
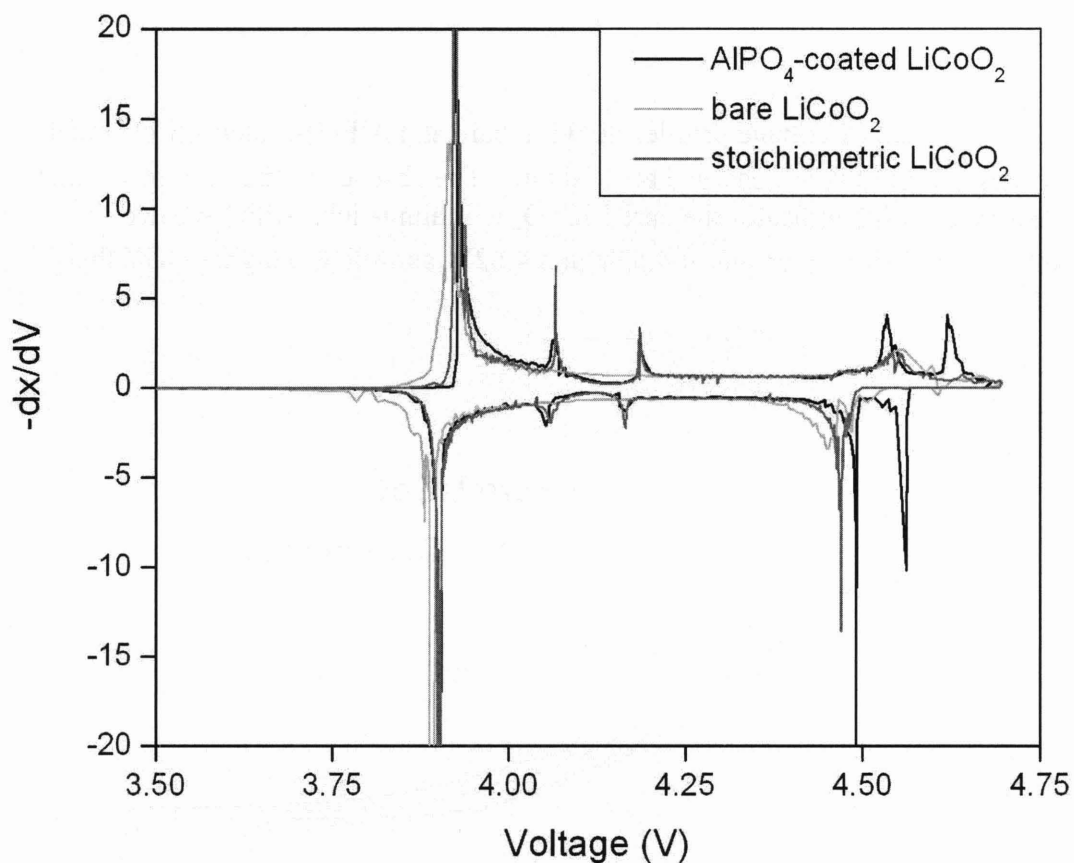
The open-circuit voltage (OCV) of the bare and coated materials as a function of lithium content provide further support to the analysis of the galvanostatic charge profile. As shown in Figure 9, the two-phase voltage plateau exists between x=0.96 and x=0.74 for the $AlPO_4$-coated $LiCoO_2$, with a voltage of 3.91V. However, the bare $LiCoO_2$ does not reach such a distinct voltage plateau, instead increasing from 3.89V to 3.91V between x=0.90 and x=0.74. Furthermore, the bare material maintains a lower open-circuit voltage throughout the range of 1 > x > 0.5, indicating that the lower charge voltage seen in the galvanostatic profile was not due to differences in overpotential, but rather differences in the equilibrium properties of the materials. The monoclinic distortion at x=0.5 is reflected in the OCV data for the coated material, as in the galvanostatic profile. Between x=0.40 and x=0.28, the OCV magnitudes coincide closely for both materials, demonstrating that they have similar equilibrium states in this range. Beyond x=0.18, the OCV behavior of the two materials differs; the $AlPO_4$-coated $LiCoO_2$ shows two voltage plateaus at 4.53V and 4.60V, while the bare $LiCoO_2$ has one sloping plateau at approximately 4.55V.

Figure 12. Open-circuit voltage as a function of lithium content for bare and AlPO$_4$-coated LiCoO$_2$.
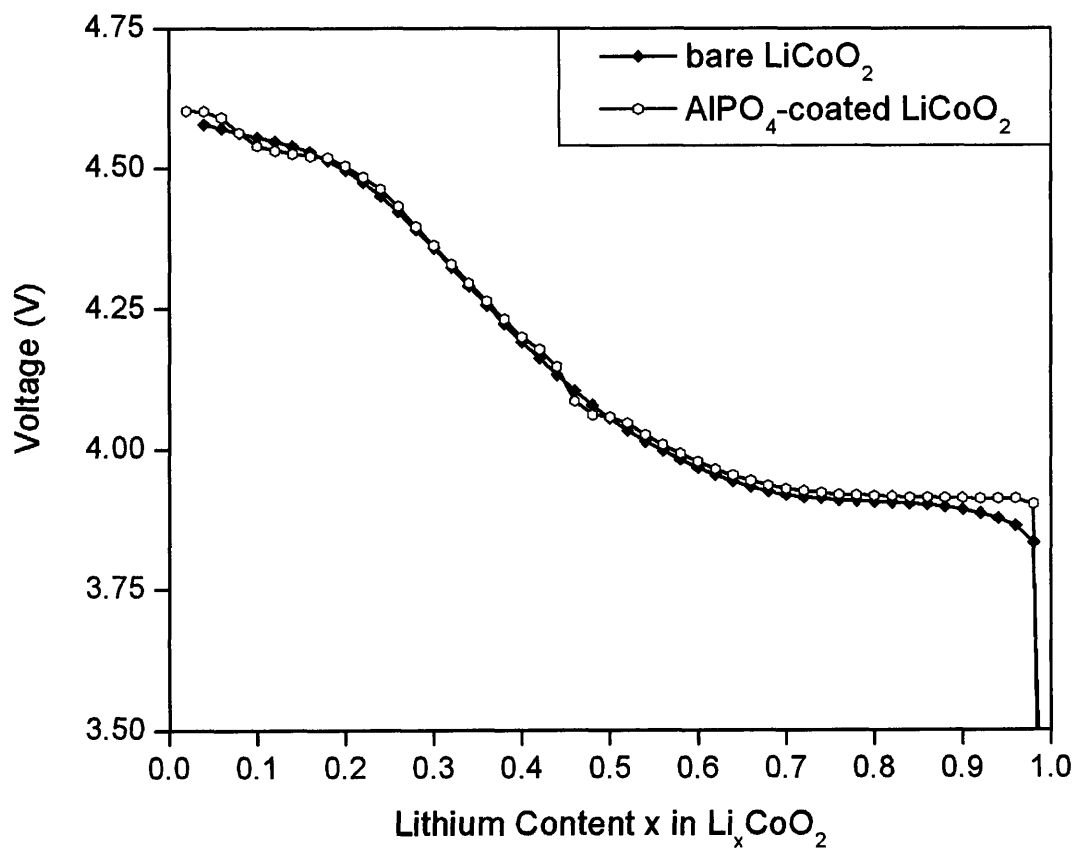
b. Galvanostatic Intermittent Titration Technique

The chemical diffusion coefficient of Li^+ ions, $\widetilde{D}_{Li+}$, in bare and $AlPO_4$-coated $LiCoO_2$ was studied by GITT at various lithium contents, as shown in Figure 13a and Figure 14a. Because straight-line behavior was not seen in the plot of E vs $\sqrt{t}$ for the duration of the 1-hour current pulse, the initial slopes were taken from plots of E vs $\sqrt{t}$ for calculations of $\widetilde{D}_{Li+}$ values. Both materials show a minimum in $\widetilde{D}_{Li+}$ at compositions corresponding to the voltage plateau given by the two-phase region between $0.75 < x < 0.96$, a behavior cited for several other oxide cathodes with phase transitions [12, 51, 69]. Values of $\widetilde{D}_{Li+}$ are on the order of 10^{-11} cm^2/s for both materials, although these exact values in this composition range contain significant error due to the fact that the change in E during the current pulse was less than 0.01V, which is the measurement limitation of the 1470 battery tester. Furthermore, values of $\widetilde{D}_{Li+}$ in this range are ambiguous due to contributions from the two coexisting phases, but may be interpreted as reflecting the long- and short-range interactions between the intercalated Li^+ ions [12]. During the short current pulse, the boundary between the two phases is moved further into the particle interior, and interactive forces between the two phases further obscure the physical meaning of the measured chemical diffusion coefficient [12].

Both bare and coated Li_xCoO_2 show a rise in $\widetilde{D}_{Li+}$ with decreasing lithium content between $0.75 < x < 0.60$. Bare Li_xCoO_2 reaches a relatively constant value of $\widetilde{D}_{Li+}$ at ~3x10-10 cm2/s beyond x=0.60, until x=~0.24 where a subsequent decrease begins. Because of the Li-rich stoichiometry of the bare $LiCoO_2$ sample, and its subsequent lack of lithium-vacancy ordering at x=0.5, it can be expected to show no minima due to

ordering between 0.75 < x < 0.24. However, $AlPO_4$-coated Li_xCoO_2 does in fact show a local maximum in $\widetilde{D}_{Li+}$ at x=0.54, followed by two local minima of $\sim1\times10^{-10}$ cm^2/s at x=0.52 and x=0.44 which surround a local maximum of $\sim1.5\times10^{-9}$ cm^2/s at x=0.46. As seen in the voltage profile in Figure 12, the center of the monoclinic distortion actually occurs at x=0.46 instead of x=0.50, which may be attributed to non-uniform cathode utilization and minor weighing errors. The correlation between this maximum in $\widetilde{D}_{Li+}$ at x=0.46 and the monoclinic distortion feature in the voltage profile indeed show the same behavior as reported experimentally by Jang et al. [59] and Hong et al. [60]. The average value of $\widetilde{D}_{Li+}$ surrounding these minima and maximum is $\sim5\times10^{-10}$ cm^2/s, which is slightly higher than the value found for bare $LiCoO_2$ above. Higher lithium content resolution in this lithium-vacancy ordering regime is necessary to accurately locate the minima and maxima in diffusivity.

At lithium concentrations less than x=0.24, both bare and coated materials show a decrease in $\widetilde{D}_{Li+}$. In bare Li_xCoO_2, a sloping voltage plateau begins at approximately x=0.18, which indicates the presence of a phase transition; as mentioned previously, two-phase regions have been associated with minima in $\widetilde{D}_{Li+}$. In $AlPO_4$-coated $LiCoO_2$, a local minima in $\widetilde{D}_{Li+}$ at 3×10^{-11} cm^2/s is seen at x=0.18, which corresponds with the beginning of the first voltage plateau at 4.52V of the O3 to H1-3 transition, displayed in Figure 12. After another rise in $\widetilde{D}_{Li+}$, a final decrease to 10^{-13} cm^2/s corresponds with the voltage plateau at 4.60V, representing the H1-3 to O1 phase transition. These trends are consistent with literature reports of minima in $\widetilde{D}_{Li+}$ during two-phase regions [12, 51, 61, 69].

The thermodynamic enhancement factor, W, which quantifies the ratio between chemical diffusivity and component diffusivity of Li^+, is given as a function of composition for bare and $AlPO_4$-coated $LiCoO_2$ in Figure 13b and Figure 14b respectively. The trends of W follow those of $\tilde{D}_{Li+}$, indicating that chemical diffusion is strongly determined by this thermodynamic factor. As W is governed by $-\dfrac{dE}{dx}$, it is not surprising that the locations of minima in W correspond with voltage plateaus in the galvanostatic profile.

Consequently, when Li^+ component diffusivity is calculated by dividing $\tilde{D}_{Li+}$ by W, the relative magnitude of these two factors will determine the coincidence or opposition of minima and maxima as a function of lithium content. Component diffusivity, D_{Li+}, is given in Figure 13c and Figure 14c. First considering bare $LiCoO_2$, D_{Li+} displays less discernable trends as a function of composition. This may be due to the fact that it has a higher dependence on $\dfrac{dE}{d\sqrt{t}}$, which contains a larger factor of error in these measurements due to the ambiguity of the proper slope to be measured in particular individual current pulse plots. This uncertainty factor may have contributed to the lack of smoothness in the D_{Li+} data. However, it may be noted that the bare $LiCoO_2$ exhibits an average value of D_{Li+} of $\sim 1 \times 10^{-11}$ cm^2/s, with a decrease occurring at lithium contents below x=0.20. Furthermore, this value differs from that shown by $AlPO_4$-coated $LiCoO_2$, with a typical value of $\sim 3 \times 10^{-11}$ cm^2/s. The coated material data also shows a larger variation in the D_{Li+} data, but several increasing and decreasing trends follow those shown by the chemical diffusion coefficient, such as minima at 4.52V and 4.60V. The

presence of minima surrounding the lithium-vacancy ordering near x=0.50 is somewhat

obscured by the uncertainty levels in this data.

Figure 13. Compositional variation of (a) chemical diffusion coefficient of Li^+, (b) thermodynamic enhancement factor, and (c) component diffusion coefficient of Li^+ in bare $LiCoO_2$.

(a)
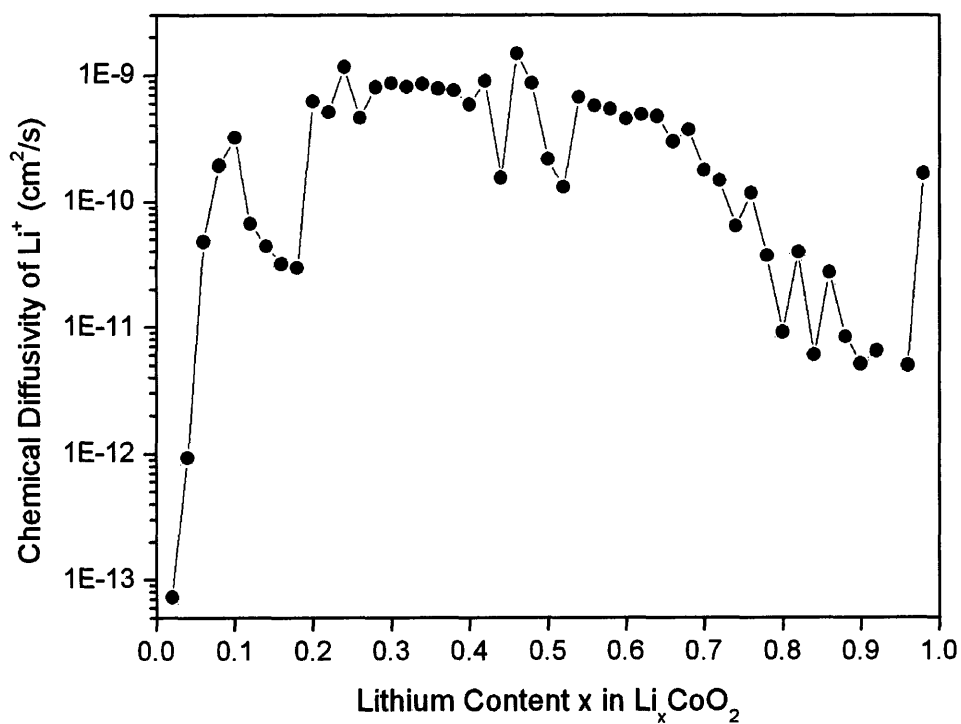
Figure 13 (continued).

(b)
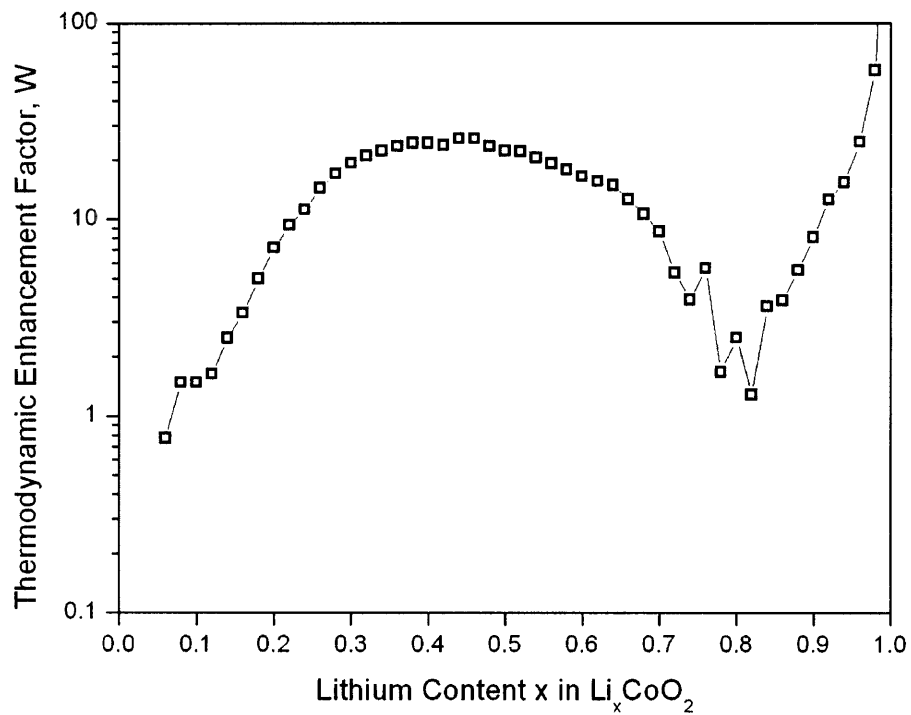
(c)
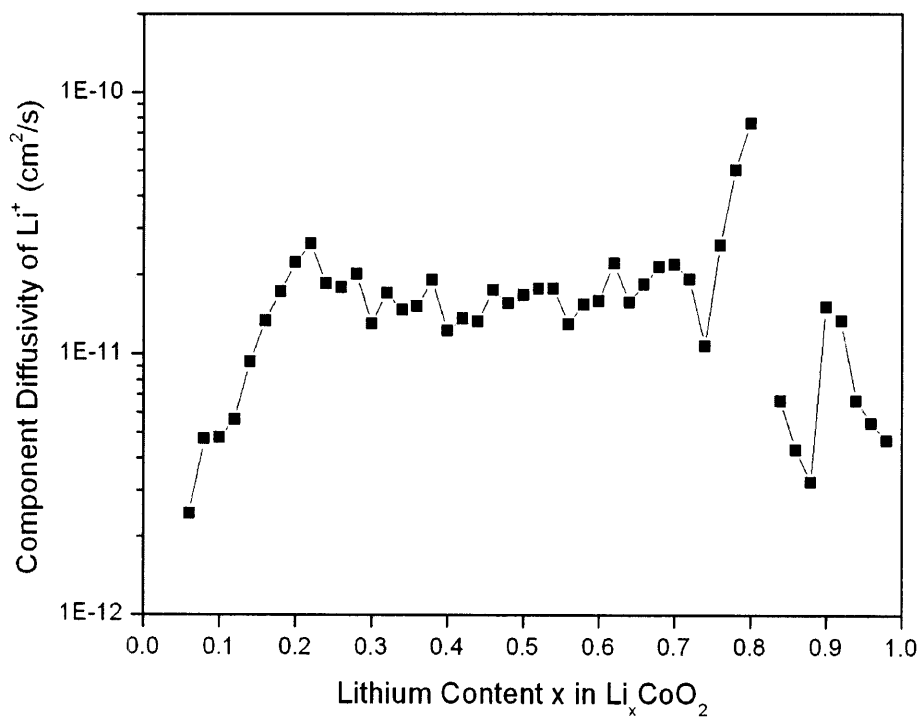
Figure 14. Compositional variation of (a) chemical diffusion coefficient of Li$^+$, (b) thermodynamic enhancement factor, and (c) component diffusion coefficient of Li$^+$ in AlPO$_4$-coated LiCoO$_2$.

(a)

(b)

(c)

The y-axis is labeled "Component Diffusivity of Li^+ (cm^2/s)" with values $1E-10$, $1E-11$, $1E-12$. The x-axis is labeled "Lithium Content x in Li_xCoO_2" with values from 0.0 to 1.0.
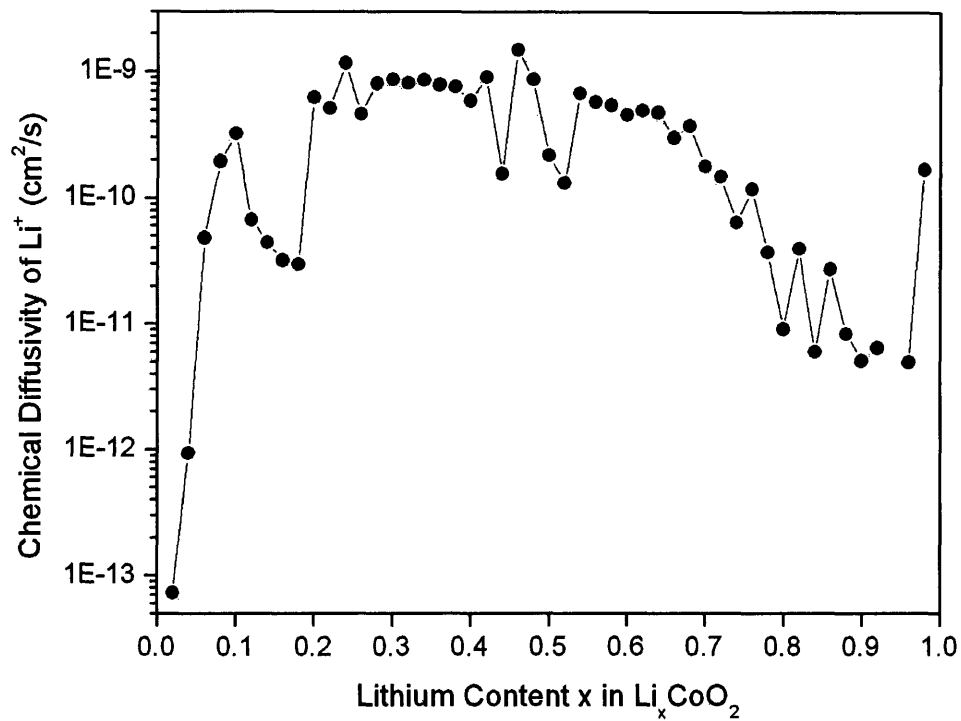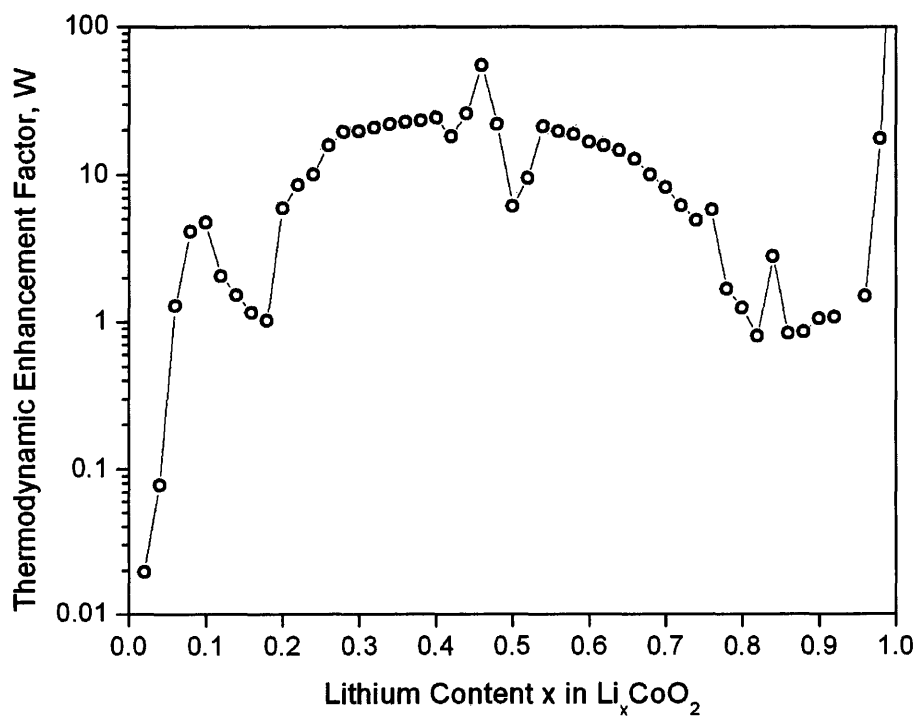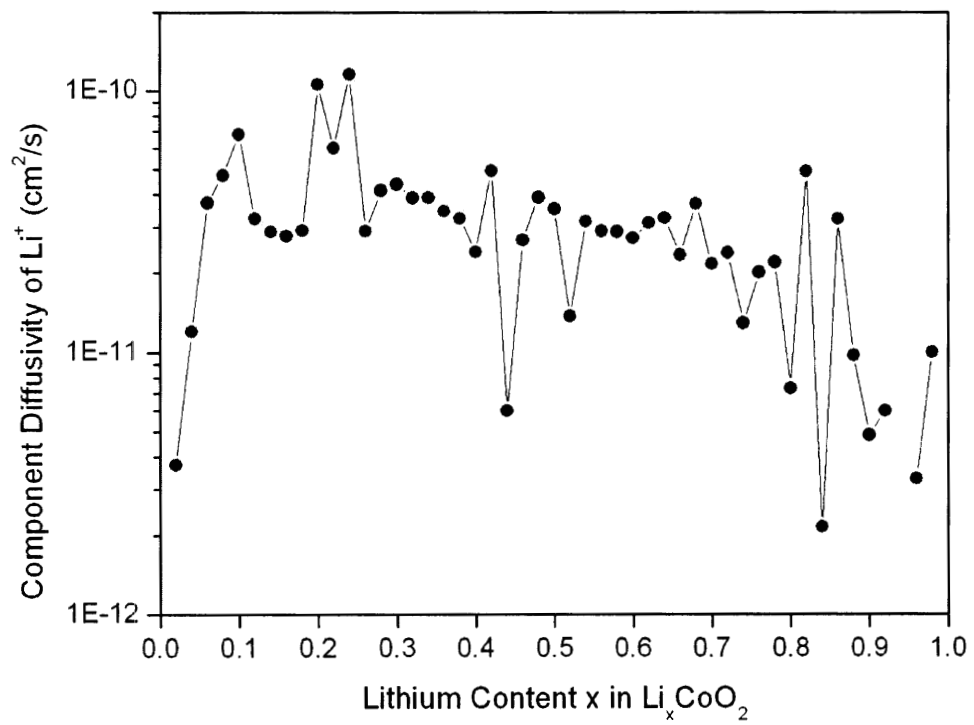
c. Electrochemical Impedance Spectroscopy

EIS spectra taken at various lithium contents along the charge profile yielded Nyquist curves with several typical features, as shown in Figure 15. The interpretation of features and assignment to particular transport processes at the positive electrode follows the analysis of Nobili et al. [53], having adapted the equivalent circuit from one proposed by Bruce and Saidi for Li^+ intercalation into TiS_2 electrodes [55]. The high-frequency region shows a semicircular feature that can be deconvoluted into two semicircles which represent the surface layer resistance and capacitance, and the charge-transfer process at the interface between the electrolyte and the active material. At lower frequencies, a large semicircle corresponds to the electronic resistance and capacitance, supported by Nobili et al.'s findings of temperature dependency for the low-frequency semicircle size [53]. The low-frequency tail is characteristic of solid-state diffusion in the bulk of $LiCoO_2$.

Figure 15. Impedance spectra from a bare LiCoO$_2$ cell show the typical trend of the data. (a) The Nyquist plot and (b) the Bode plot show the dramatic decrease in size of the low-frequency semicircle with increasing voltage at the beginning of charging. The high-frequency region shows a convolution of two small semicircles.
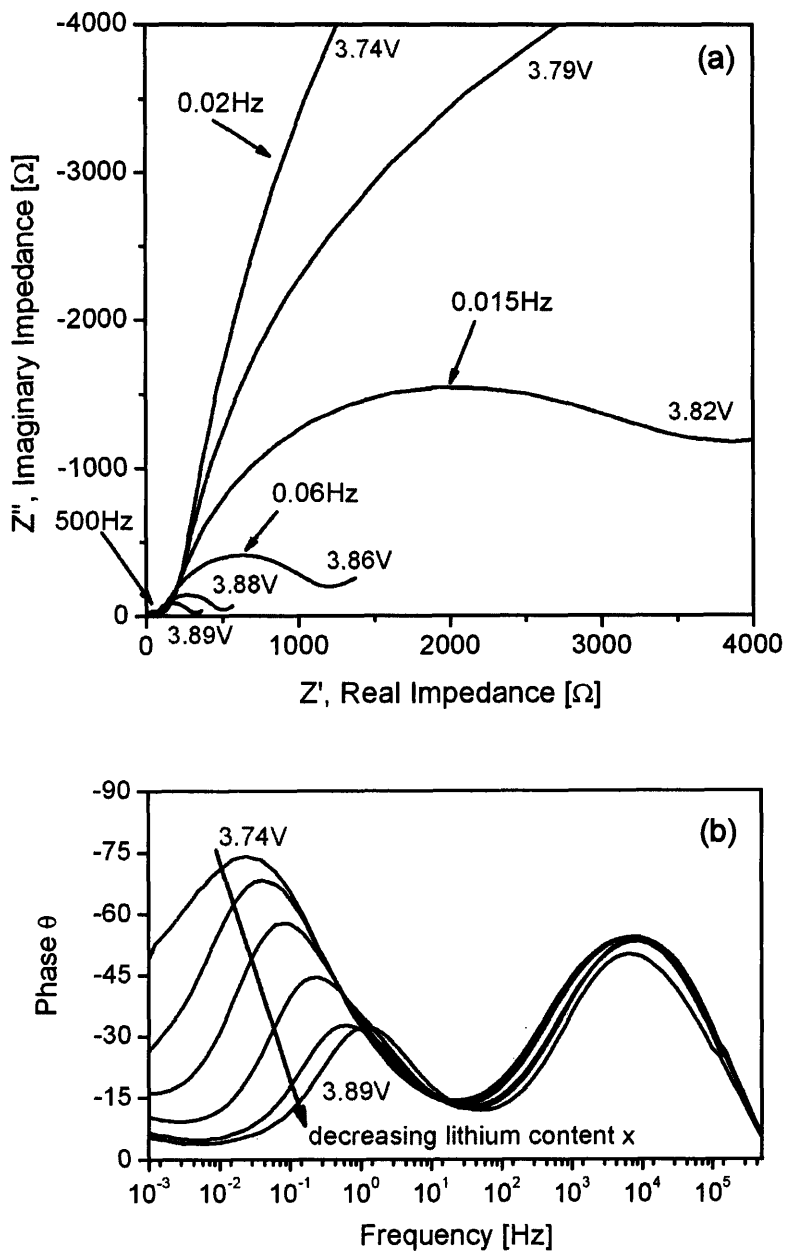
Figure 16 shows the equivalent circuit used to model these transport processes in the positive electrode material, as adapted from Nobili et al. [53]. However, due to the fact that two-electrode cells were used for this experiment, it is possible that the EIS data may include a response from the Li metal anode surface. EIS testing on Li-Li symmetric cells with no applied polarization show two semicircles on the Nyquist plot, with a total magnitude of $\sim 300\Omega$. This magnitude decreased upon polarizing the symmetric cell, but exact values cannot be extracted and applied to the $Li/LiCoO_2$ cell, which operates under different conditions. Because the peak frequencies of these semicircles, 0.2 Hz and 80 Hz, overlap with the charge-transfer process on the cathode side, the high frequency data for the $Li/LiCoO_2$ coin cells at x=1.0 cannot be attributed to the cathode alone. As deintercalation of $LiCoO_2$ proceeds, it is unclear how much the response of the Li metal surface affects the data, without using a reference electrode. However, due to the differences in peak frequency, the low-frequency semicircle of the $Li/LiCoO_2$ cell can still be valid in discerning trends in electronic resistance of the cathode. Studies of $LiCoO_2$ in three-electrode cells are planned in order to verify the coin cell data.

Figure 16. The physical transport processes associated with a LiCoO$_2$ particle in (a) can be modeled by the equivalent circuit in (b) in order to interpret the experimental EIS data. This circuit consists of several RC-elements to represent the surface layer, the electric double layer and charge transfer from solution, and the electronic resistance. A Warburg impedance element represents solid-state diffusion of Li$^+$ in the bulk.
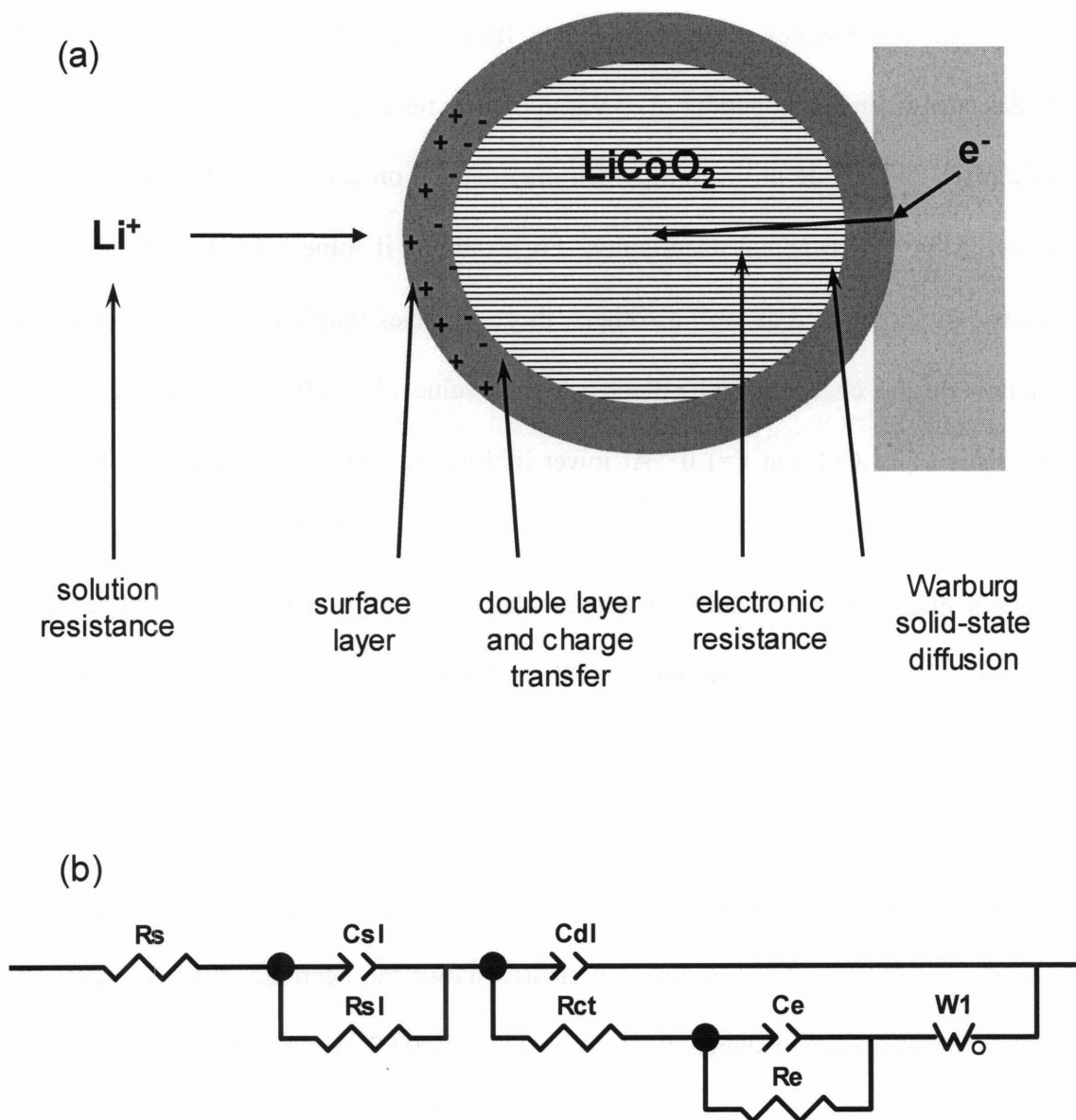
The electronic resistance results of the EIS curve-fitting for the bare and the $AlPO_4$-coated $LiCoO_2$ sample are given in Figure 17 and Figure 18, respectively. As several electrode batches were made during this study, the results from the different batches are plotted separately to show the trends more clearly, while the actual values of resistance may vary between batches. Supporting data from other batches of bare and coated electrodes are given in Appendix A. Variations in resistance values may stem from nonuniformity in cathode utilization, which may depend on cathode thickness variations and unavoidable experimental uncertainty. For example, if some $LiCoO_2$ particles were not electrically connected as well as others, those particles may have a lower degree of delithiation during charging and reflect a higher value of electronic resistance that is characteristic of Li_xCoO_2 at x=1.0. At lower lithium contents, we measure the average resistance of all particles in the cathode; this average may be higher for some electrodes than others due to this non-uniform deintercalation. Care is taken to minimize such uncertainties within experimental reason. EIS results are organized, in general, according to electrode batch.

The electronic resistance evolution of bare $LiCoO_2$ during charge at C/50 in Figure 17 for batches B1 and B2 together. Figure 17a clearly shows the decrease of three orders of magnitude in electronic resistance, R_e, from x=1.0 to x=0.90, which corresponds with the insulator-metal transition of Li_xCoO_2. After x=0.90, R_e can be considered constant at a value of 30-100Ω, until approximately x=0.40. At lithium contents below x=0.40, R_e begins increasing again. The magnitude of this increase varies between electrode batches, but can be considered to rise by 3 orders of magnitude between x=0.40 and x=0.

In order to correlate changes in R_e with phase transitions occurring in Li_xCoO_2, R_e data is displayed as a function of voltage in Figure 17b. While lithium content values are calculated based on cathode weight which is subject to experimental error, voltage data is comparable between cells given that all cells are charged at C/50 rates and can be correlated with well-known plateaus in the voltage profile. From this representation, one can see that the initial decrease in R_e corresponds with the rise to the voltage plateau at 3.91V, and the subsequent rise in R_e begins around 4.5V, which is associated with the sloping voltage plateau discussed in the previous section.

The trends for R_e of bare $LiCoO_2$ are compared with those of $AlPO_4$-coated $LiCoO_2$. Figure 18 show the trends in R_e for electrode batch C3 of $AlPO_4$-coated $LiCoO_2$, grouped according to performance. Initial delithiation of the material shows a similar drop of three orders of magnitude in R_e, from 10^5 to 20-100Ω as for the bare $LiCoO_2$. However, in this case most of the drop occurs before x=0.95. This phenomenon is probably related to the fact that $AlPO_4$-coated $LiCoO_2$ shows a sharper rise to the two-phase region plateau at 3.93V, compared to the more sloping two-phase plateau of bare $LiCoO_2$, as shown previously in Figure 8. For both materials, the arrival at the first voltage plateau corresponds with the resistance drop. This observation also suggests that the insulator-to-metal transition occurs before the two-phase region begins in $LiCoO_2$.

At approximately x=0.22, R_e increases for $AlPO_4$-coated $LiCoO_2$, as seen clearly in Figure 18a for electrode batch C3, which contained a high level of uniformity and therefore more reproducible data. This rise in R_e clearly begins at ~4.53V, as seen in

Figure 18b, which corresponds to the onset of the O3 to H1-3 phase transition plateau.

Therefore, these results indicate that the H1-3 phase and the following O1 phase have

lower conductivity than O3.

Figure 17. Results of equivalent circuit fitting for the EIS spectra yield trends in electronic resistance as a function of (a) lithium deintercalation and (b) voltage in bare Li_xCoO_2 for electrode batches B1 and B2. X-error bars are included in (a) to indicate the effect of weighing errors and non-uniform cathode utilization. Resistance as a function of voltage, (b), shows the relation to features in the charge profile and removes weighing errors.
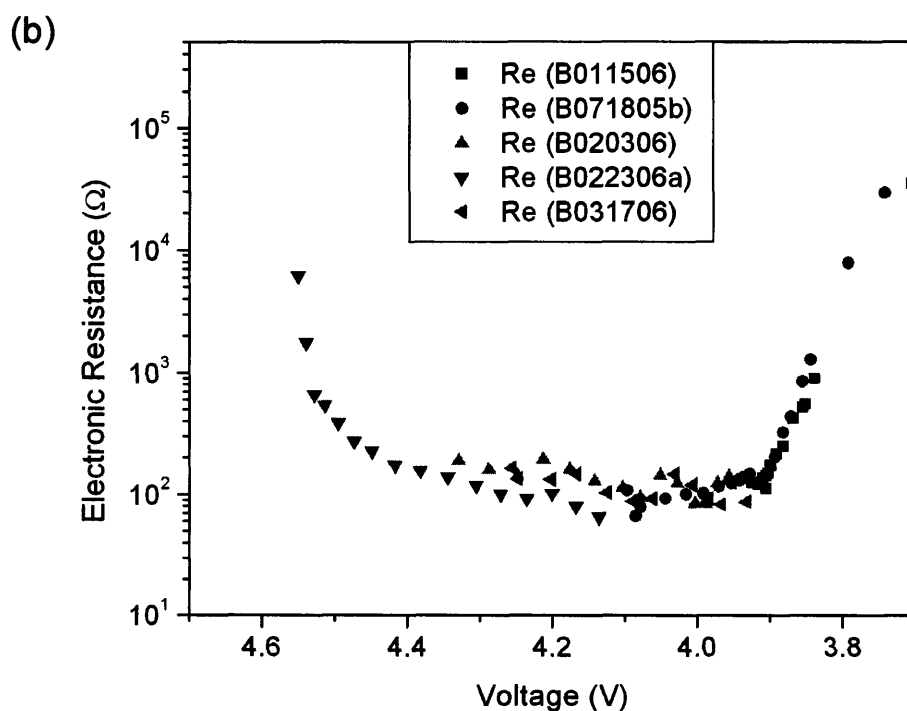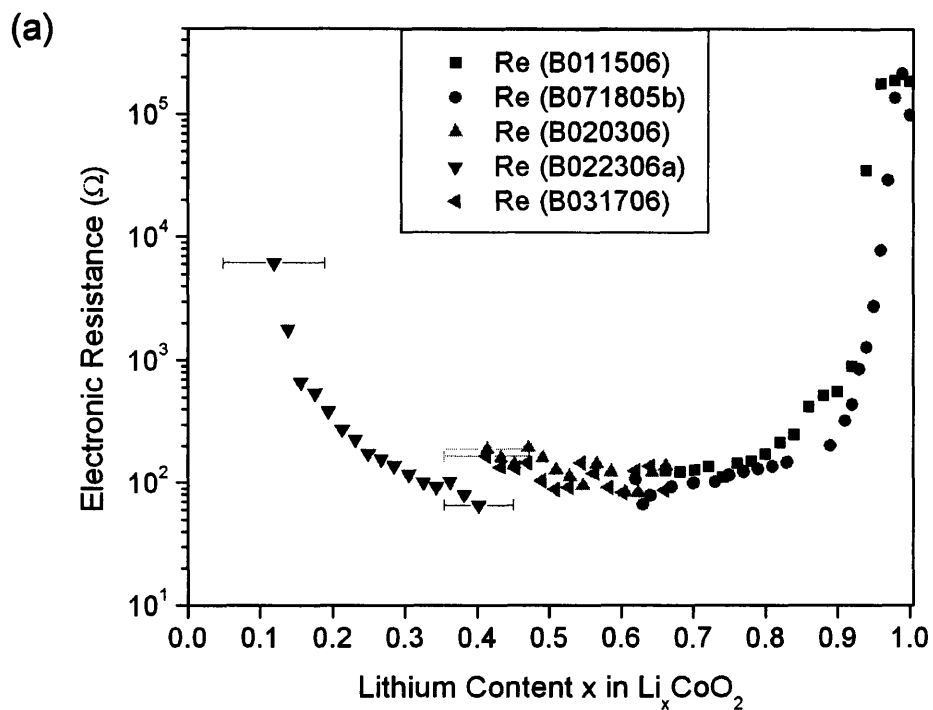
Figure 18. Results of equivalent circuit fitting for the EIS spectra yield trends in electronic resistance as a function of (a) lithium deintercalation and (b) voltage in $AlPO_4$-coated Li_xCoO_2 for electrode batch C3. The y-axis in (b) is displayed in linear scale rather than logarithmic as in (a) in order to show details in the voltage range of interest.
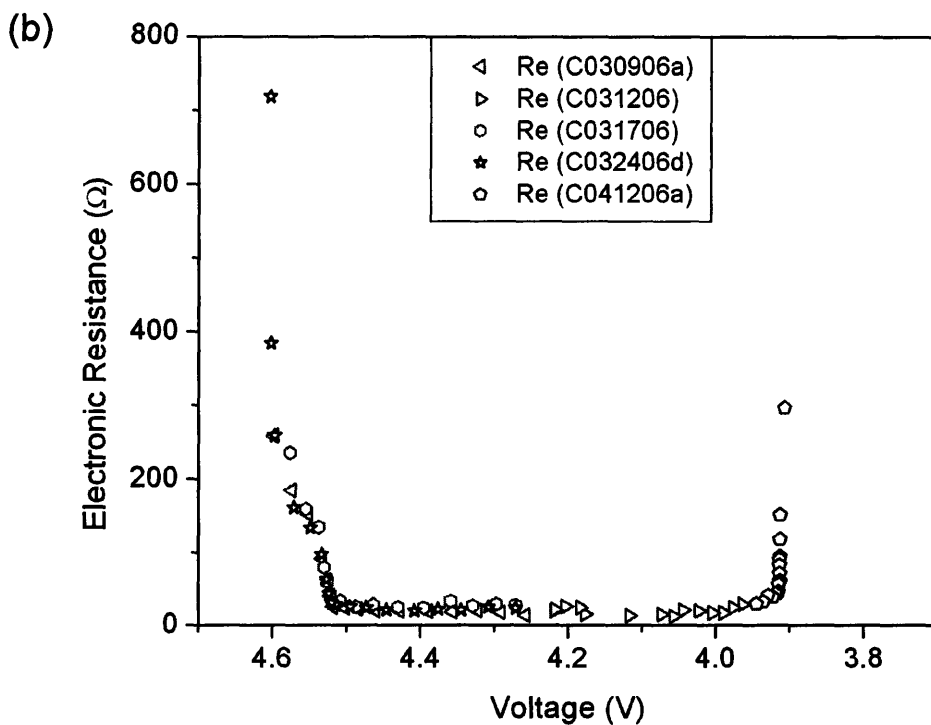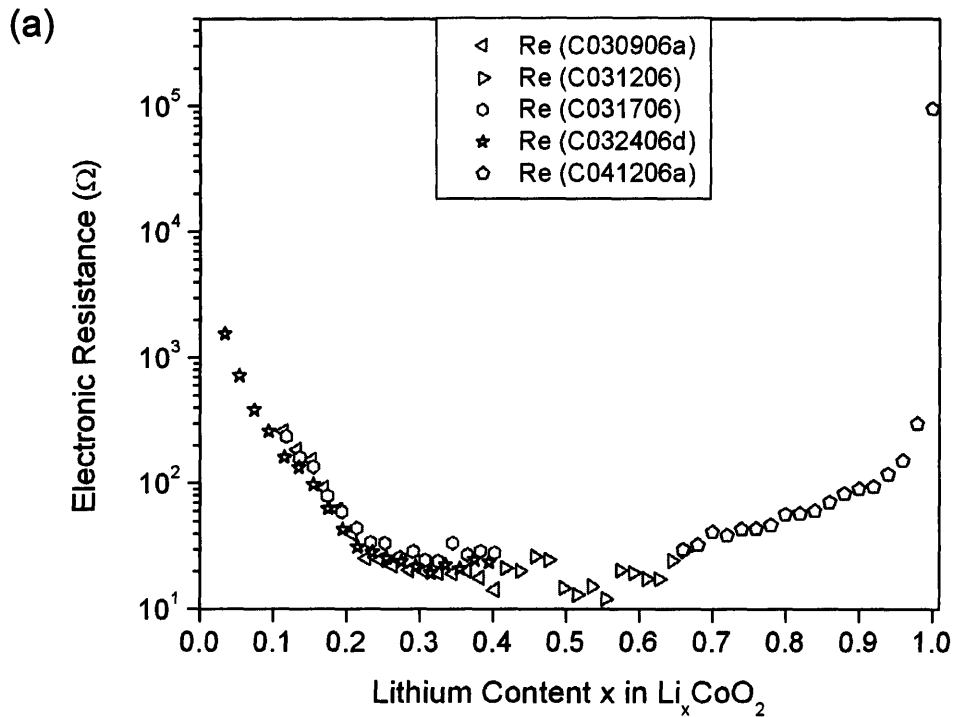
d. Discussion

The voltage profiles of the bare and coated materials lend more insight to their stoichiometry and electrochemical behavior. The bare $LiCoO_2$ voltage increases monotonically upon charging, as is reported for overstoichiometric $LiCoO_2$ with as little as 10% excess Li [21]. However, the $AlPO_4$ coating leads to the appearance of features such as the lithium-vacancy ordering distortion near $x=0.5$ and the two phase-transition plateaus at higher voltage, which are only seen for stoichiometric $LiCoO_2$ [21]. From this evidence, it is possible that during the 5-hour annealing step at 700°C during the coating process, diffusion of excess lithium towards the particle surface left stoichiometric $LiCoO_2$ in the bulk. The excess lithium may have formed a compound with the coating layer, or it may have been removed in the form of Li_2O. Levasseur et al. have reported that a 900°C heat-treatment either at extended length of 5 days or under high oxygen pressure of 5GPa leads to removal of excess lithium from $Li_{1.08}CoO_2$ in the form of Li_2O [70], but it is not clear if the 700°C 5-hour anneal in the coating procedure is sufficient to produce the same effect. Another possibility is the diffusion of some Al from the coating layer into the surface of the $LiCoO_2$ particle during the heat-treatment, which may explain the slight rise in deintercalation voltage by 0.02V in the coated sample, corresponding to the theoretical calculations of Ceder et al. [22]. However, Myung et al. find that doping $LiCoO_2$ with 10% Al to form $LiCo_{0.9}Al_{0.1}O_2$ results in a monotonically increasing voltage profile [23], which is not shown for the $AlPO_4$-coated $LiCoO_2$ studied here; however it must contain much less than 10% Al.

The open-circuit voltage curves of Figure 12 reveal the higher deintercalation voltage of $AlPO_4$-coated $LiCoO_2$, which may reflect the stoichiometric composition of the bulk material as mentioned previously. This data further supports the proposed compositions postulated from the galvanostatic voltage profiles.

GITT studies show that the $AlPO_4$-coated $LiCoO_2$ displays a higher average chemical diffusion coefficient than the bare material by a factor of two during the first charge. Cho et al. have also shown that $AlPO_4$-coated $LiCoO_2$ has a higher Li^+ diffusivity of $\sim 10^{-11}$ cm^2/s compared with $\sim 3 \times 10^{-12}$ cm^2/s of bare $LiCoO_2$ [35]. While the comparative values of diffusivity between the two samples are similar to those presented here, the absolute magnitudes are lower than those here, which may be due to different assumptions of cathode surface area due to the highly porous nature of composite cathodes. Values presented here are closer to those reported by Jang et al., who find increasing values of $\widetilde{D}_{Li+}$ for $0.70 > x > 0.55$ on the order of 10^{-10} cm^2/s [59]. Furthermore, they also find two local minima surrounding a maximum at the ordered stoichiometry of x=0.50, similar to the results discussed here. Furthermore, they also similar trends between $\widetilde{D}_{Li+}$ and W, but their relative magnitudes combine to produce a minimum in component diffusivity at x=0.5. These experimental findings by Jang et al. [59] also correspond to the theoretical predictions made by Ceder et al., who calculate a a minimum in Li^+ chemical diffusivity at x=0.5 [71]. They explain this minimum in diffusivity as a "locking up" of the lithium vacancies that are necessary for diffusion of ions, resulting from the lithium-vacancy ordering which occurs at this composition. They suggest that variations in the intensity of this minimum are related to the purity of the sample, which affects the level of order

achieved at x=0.5. Similarly, the results for $AlPO_4$-coated $LiCoO_2$ displayed in this report may contain impurities due to the coating layer which may affect the level of ordering at x=0.5. A higher resolution of data points in the surrounding concentration range may also clarify the detailed trends occurring near this ordered stoichiometry.

The Nyquist plot features for both bare and $AlPO_4$-coated $LiCoO_2$ are similar to those previously reported [12, 54]. The evolution of the electronic semicircle for the bare material shows a gradually decreasing trend upon initial deintercalation, whereas the coated material shows a rapid decrease as a function of lithium content. This difference in behavior relates to the voltage profiles of bare and coated $LiCoO_2$. The bare $LiCoO_2$ follows a more sloping path to the large plateau, while the coated $LiCoO_2$ steeply rises to that plateau. Thus the arrival at ~100 Ω magnitude for electronic resistance corresponds to the arrival at the two-phase region of the voltage profile. No change in R_e is observed for the lithium-vacancy ordering at x=0.5, during which the overall structure of the material is still in the O3 phase. Upon reaching the phase transition to H1-3 near 4.5V, R_e magnitude increases for both bare and $AlPO_4$-coated $LiCoO_2$. This increase may provide some insight into the reasons behind cathode instability when cycled to high voltages above 4.4V. While the coated material does not prevent this increase in R_e, it may increase the surface stability of the $LiCoO_2$ particles and hinder microcracks and Co dissolution during cycling.

IV. Microstructure Characterization of AlPO$_4$-coated and Bare LiCoO$_2$

a. Surface Morphology

The surface morphologies of the bare and coated crystals are compared in Figure 19, respectively. The rounded shape of the LiCoO$_2$ particle edges in Figure 19a differs from the highly faceted shapes of typical stoichiometric LiCoO$_2$ crystals. The intricate texture of the AlPO$_4$ coating is shown in Figure 19b; the nature of its topography appears to be different on various faces of the crystal. The top-facing side shows small bumps while the surrounding faces appear to have small pits. This morphology can be seen more clearly in Figure 20, where a fractured particle reveals the orientation of the layers in LiCoO$_2$. The AlPO$_4$ coating surfaces that are normal to these layers have a pitted texture, while the surface parallel to the layers shows only convex bumps. To eliminate the possibility of an imaging artifact in SEM, this observation of specifically oriented surface textures is confirmed by AFM examination, as seen in Figure 22. AFM section profiles of the coated particle reveal ~100nm wide pits on the side faces and ~50-150nm high bumps on the top face. The surface texture of bare LiCoO$_2$ is contrasted in Figure 21b, which displays a smooth rounded surface with small bumps that are most likely Li$_2$CO$_3$ [72].

Figure 19. Scanning electron micrographs of (a) bare $LiCoO_2$ and (b) $AlPO_4$-coated $LiCoO_2$, showing the rounded shape of the particles. Average particle size is 5-10 mm. The $AlPO_4$-coated sample shows a unique pitted texture on the side faces.

(a)

(b)
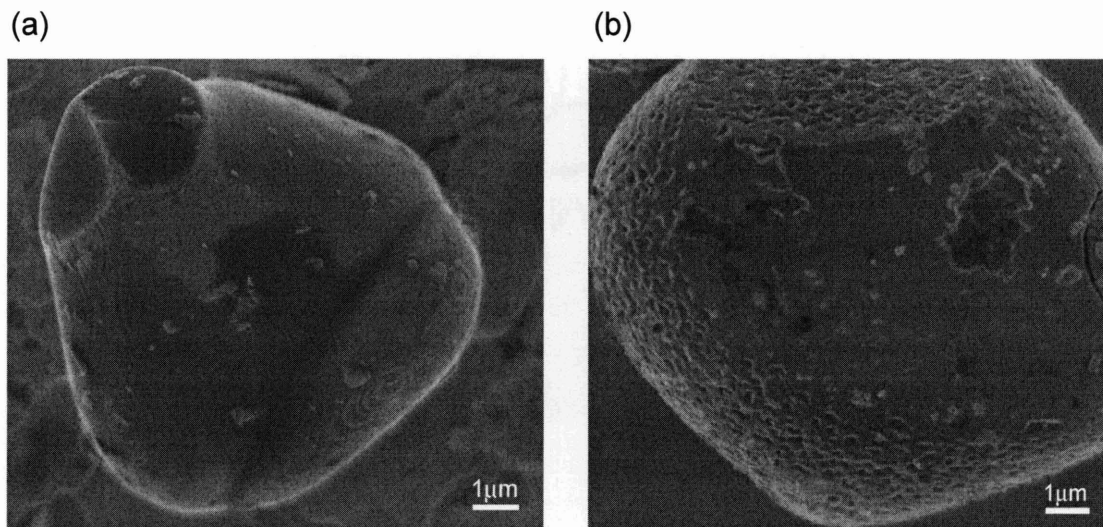
Figure 20. A fractured particle of $AlPO_4$-coated $LiCoO_2$ shows that the layers of the bulk material are oriented normal to the coating faces which show a pitted texture.
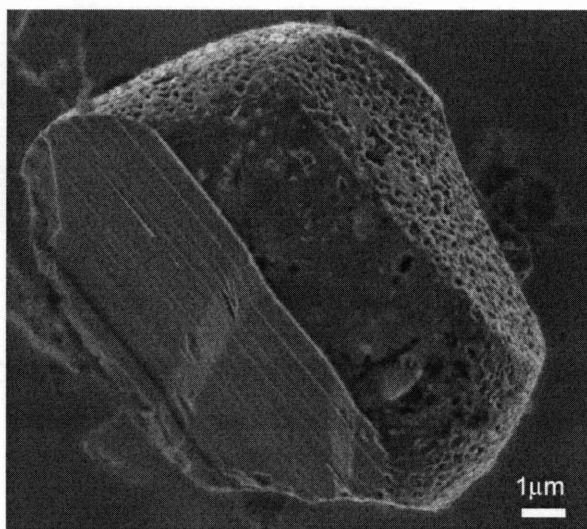
Figure 21. High-resolution SEM image of small rounded bumps on a bare $LiCoO_2$ particle.

1 μm
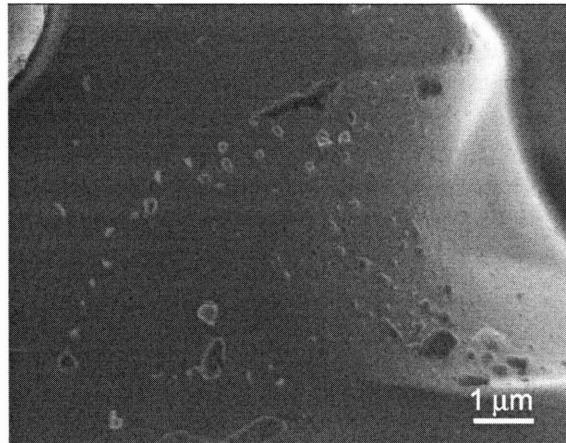
Figure 22. AFM images of a coated particle confirm that the pitted texture of the $AlPO_4$-coated $LiCoO_2$ is in fact present only on side faces of the particle, and only protruding bumps appear on the flatter face.

2μm

0

pitted
side
faces

15μm

10

5

0
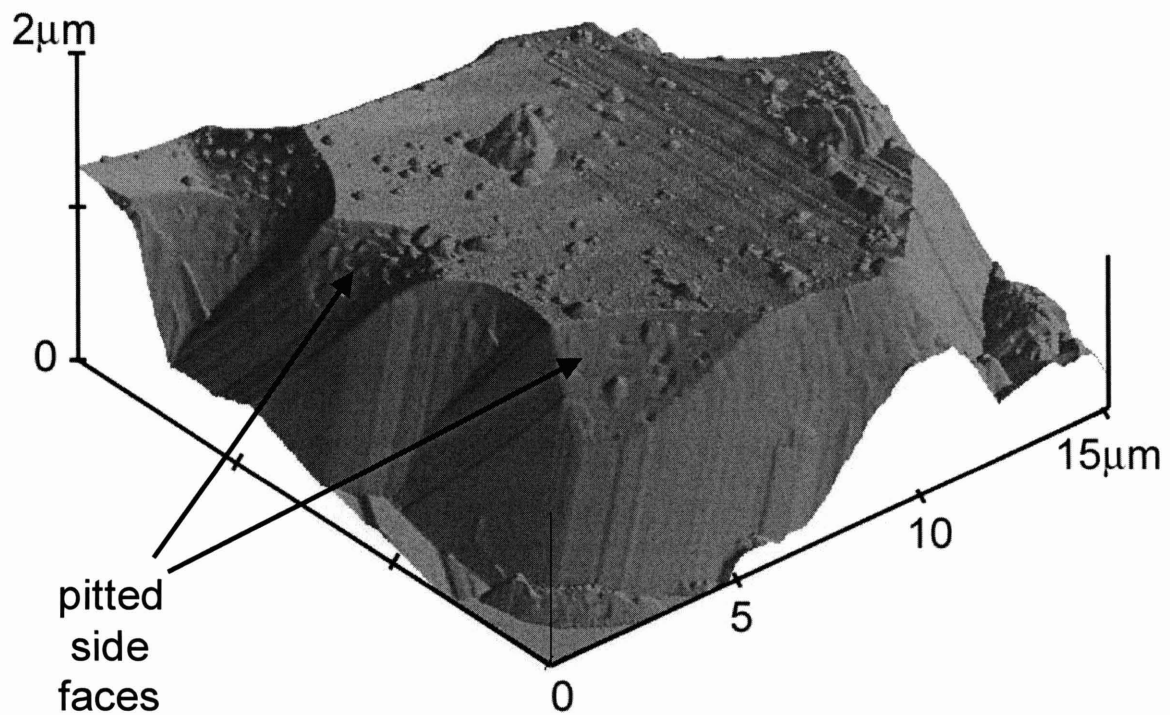
b. Cross-Sectional Morphology

Cross-sectional TEM images of thin slices of $AlPO_4$-coated $LiCoO_2$ reveal the coating thickness in Figure 23. The coating layer appears to cover the entire particle surface, with a thickness variation of 10-100nm over many $LiCoO_2$ particles. The thin coating-layer microstructure is characterized by small spot-like features, while the adjacent bulk $LiCoO_2$ contains lattice fringes, as shown in Figure 23b. In the figure, the almost vertically-oriented lattice fringes nearest the coating correspond to a d-spacing of 2.53Å, which is close to the (101) plane spacing of the hexagonal cell, typically 2.41Å. The horizontal lattice fringes are spaced at 4.47Å, which is close to one-third of the c-axis parameter of the hexagonal cell, 14.05Å. According to Jang et al., substitution of Al for Co causes a decrease in the a-axis and an increase in the c-axis [18]. While the measured values from the known $LiCoO_2$ d-spacings do not follow this trend, it is possible that the deviation is within the margin of error inherent to measurement from the TEM image. However, observance of these lattice fringes is useful in distinguishing the $LiCoO_2$ from the coating layer. The level of crystallinity of the coating is yet unknown, as the coating thickness is too small to produce an electron diffraction pattern.

Figure 23. Cross-sectional TEM images of the AlPO$_4$-coated LiCoO$_2$ show uniform coverage of the particle surface, with a thickness variation of 10-100nm. High-resolution TEM images of the AlPO$_4$ coating cross-section show a light-dark variation which may indicate regions of varying composition or thickness in the coating. The spacing between lattice lines in region A is 2.53Å ((101) plane), and the spacing between lattice lines in region B is 4.47Å (one third of c-axis). The coating layer shows no lattice fringes.
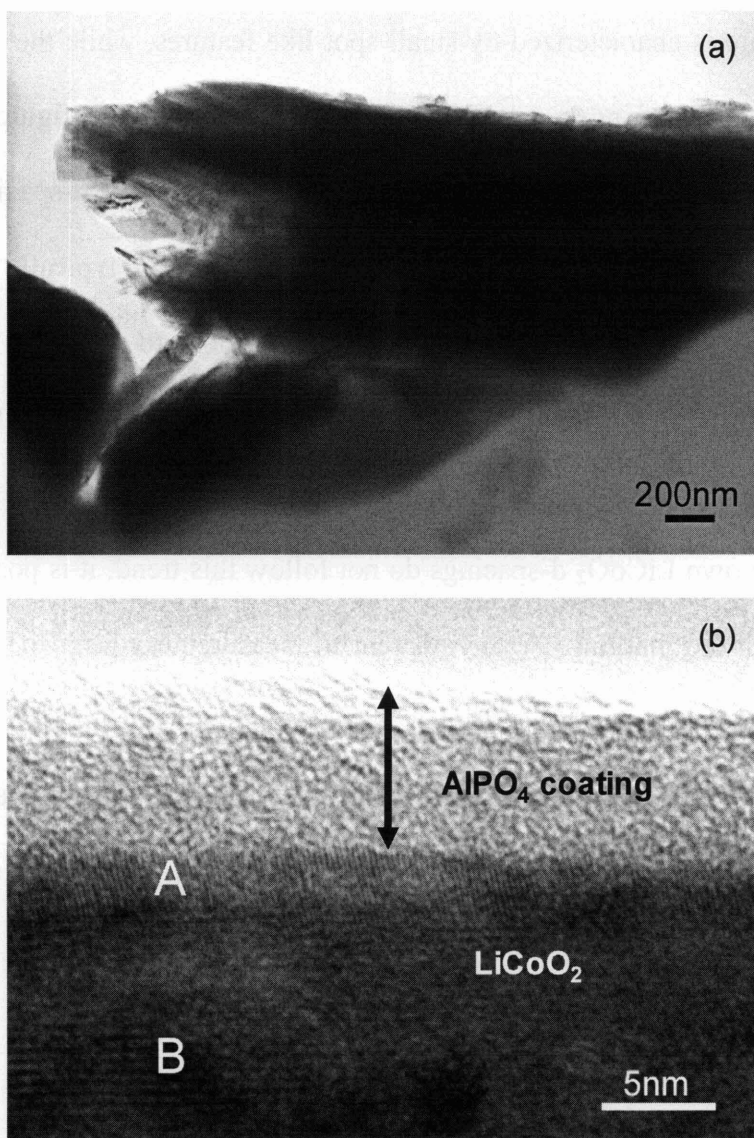
c. Elemental Mapping in Transmission Mode

Investigation of the composition and uniformity of the coating on each $LiCoO_2$ particle was conducted using elemental mapping through STEM. EDX mapping of an $AlPO_4$-coated $LiCoO_2$ particle cross-section in Figure 24 reveals the non-uniform distribution of Al and P in the coating layer. While Co appears to be confined to the interior of the particle as expected, the Al and P do not show the same regions of high or low intensity, as would be expected if they occurred in a 1:1 intensity ratio of Al:P as in $AlPO_4$. EDX point spectra obtained from several places across the particle revealed variation in this ratio ranging from 0.2 to 8.8, which indicates that there may be regions of Al-rich and P-rich material or the formation of a solid solution between $AlPO_4$ components and $LiCoO_2$. As shown more clearly in Figure 25, the Al signal appears to uniformly cover the entire particle, without fading near the particle edge which may indicate its presence on the surface; in contrast, the Co signal becomes weaker towards the edge of the particle due to thickness effects. The P signal does not appear to cover the surface completely as the Al does, but rather exist in particular regions in high concentration.

Increased magnification of a particle edge yields a detailed map of a thicker region of the coating, in Figure 26. Clearly, the Al and P exist in distinctly different regions of the coating; part of the Al region contains no P at all. The feature containing a high P concentration also coincides with the O signal, suggesting that this part of the coating is a phosphate compound. However due to the difference in the Al signal, one must infer that the coating is not precisely $AlPO_4$. Unlike the P signal, the Al signal intensity also remains consistent into the bulk region of this particle, indicating it may be coated with a

layer of Al, Al_2O_3, or Li-Al-Co-O compound, without phosphorus. Indeed, Figure 27 shows a high-magnification image of a coating surface which lacked the large coating bumps usually associated with high P signal. In fact, over a long data collection time, a strong Al signal was collected, showing uniform coverage with a clear border at the particle edge. However, the P signal was negligible, with no intensity higher than the background radiation. These observations indicate that an Al-rich coating layer uniformly covers this region of the particle, in a compound containing little or no phosphorus.

Figure 24. Energy-dispersive x-ray mapping on a cross-sectional piece of $AlPO_4$-coated $LiCoO_2$ shows the physical distribution of the elements of interest. The distributions of aluminum and phosphorus in the coating region are non-uniform. Regions with strong phosphorus signal are concentrated in the thick, rough layer of coating at the edge. Aluminum signals are more evenly distributed across the particle.
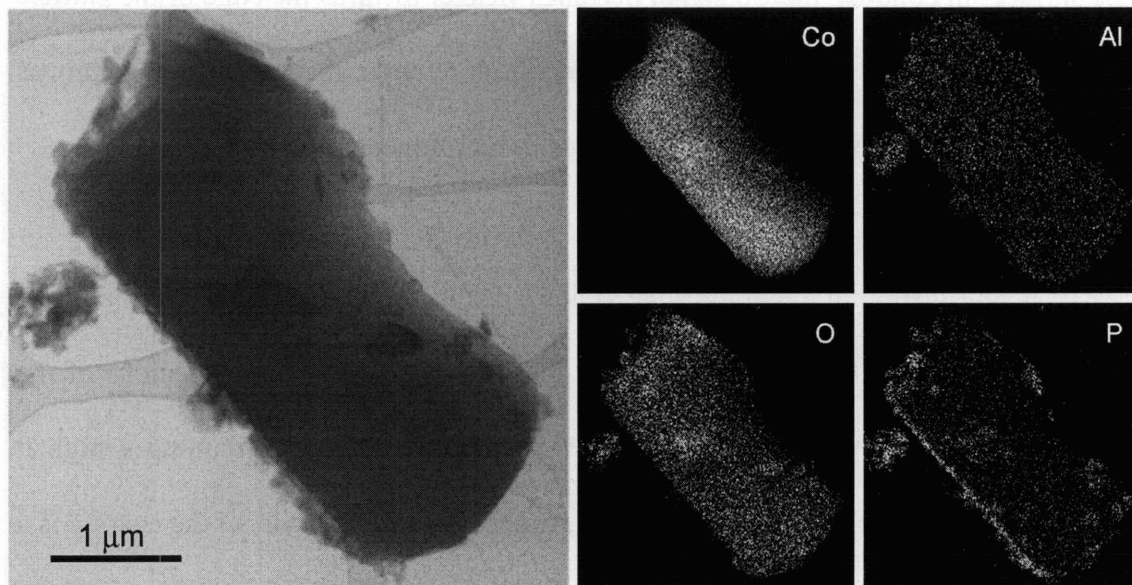
Figure 25. EDX mapping of single LiCoO$_2$ particle shows small concentrated areas of phosphorus, but aluminum distribution is more uniform over surface of particle. Aluminum signal extends to the borders of the particle, in contrast to cobalt in the particle bulk, which fades with closeness to the edge, showing a thickness effect.
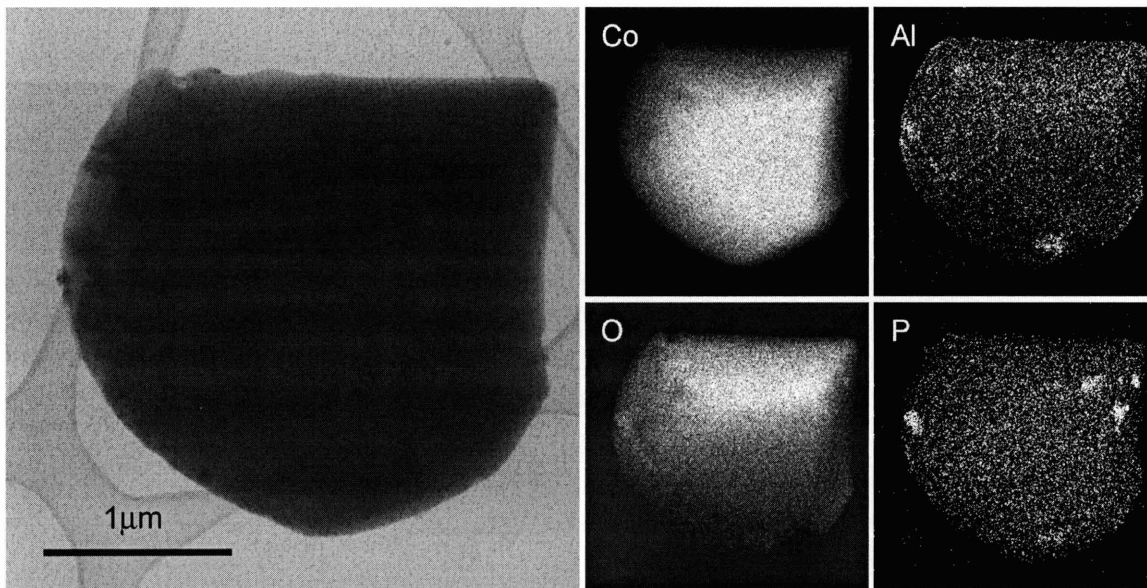
Figure 26. EDX mapping of AlPO$_4$-coated LiCoO$_2$ particle edge with STEM. Only the vertical center band of the image has been mapped by EDX. Clearly, certain features correspond to phosphorus-rich clusters, while the aluminum is more evenly distributed across the thick coating region and the rest of the particle surface. Oxygen distribution follows the phosphorus distribution most closely, and cobalt is confined to the particle bulk as expected.
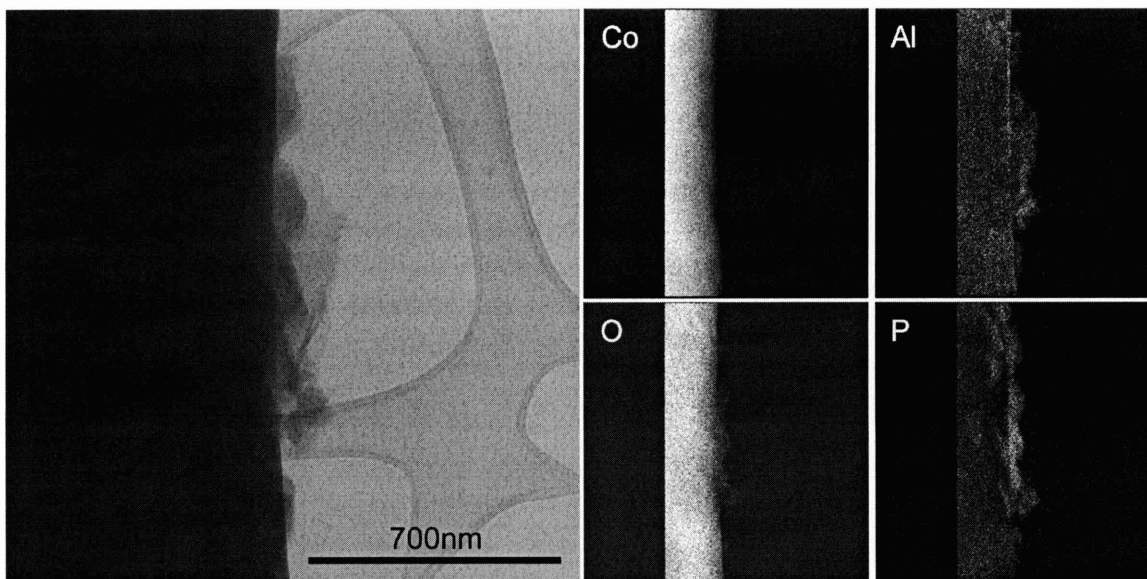
Figure 27. A region of an AlPO$_4$-coated LiCoO$_2$ particle with a thin-coating layer only. The phosphorus signal is negligible, while the aluminum signal has uniform coverage of the surface, showing no fading effects close to the edge which indicates it resides on or near the particle surface and not in the bulk.
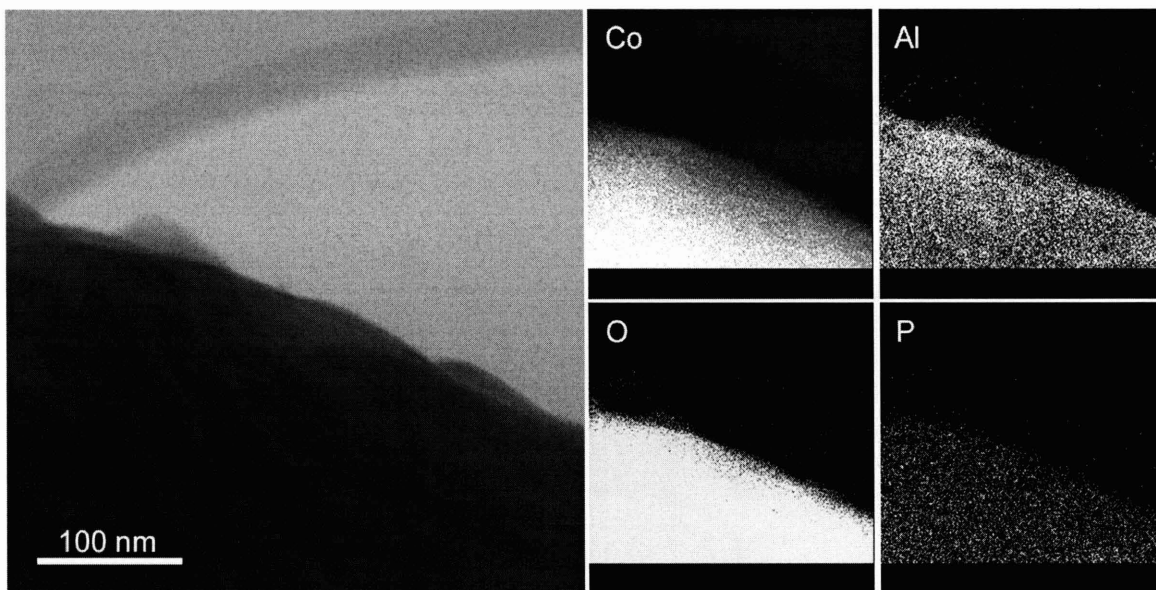
d. XPS Surface Analysis

X-ray photoelectron spectroscopy (XPS) measurements were taken to explore the surface chemistries of aluminum, phosphorus, lithium, cobalt, and oxygen on the surface of bare and coated $LiCoO_2$. Samples of bare $LiCoO_2$ and $AlPO_4$-coated $LiCoO_2$ were studied together to determine the different surface chemistries present on each sample. In the same session, Li_2CO_3 was also examined as a comparative reference to ascertain its presence on the surfaces of the other two materials.

XPS spectra for all three samples were calibrated for instrumental shift according to the C 1s hydrocarbon peak at 285 eV, which is widely used as a reference. The origin of this carbon peak is adventitious non-graphitic carbon contamination, as discussed in the literature [73, 74]. P. Swift cautions that the use of the C 1s hydrocarbon contamination peak should not be used as an absolute reference between XPS data collected on different instruments, unless absolute energy calibration is defined by a reliable peak such as Au 4f 7/2 [74]. Because the results presented here were collected on the same instrument during a single XPS session and have been calibrated consistently, they can still give a useful comparative look at the surface chemistries of the bare and coated samples.

In addition to calibration, the C 1s spectra provide information about the presence of Li_2CO_3 on the surface of the active material. Peaks for hydrocarbons have been calibrated to 285 eV, as mentioned above, and a second peak at 289.7 eV can be attributed to carbon in Li_2CO_3 [73], shown in Figure 28c. The presence of the small peak at 289.7 eV in the bare $LiCoO_2$ sample indicates the existence of some Li_2CO_3 on the

surface. $AlPO_4$-coated $LiCoO_2$ also shows a small peak near 289.4 eV, which may suggest the presence of Li_2CO_3 on the coated particle surface as well.

Figure 28. XPS spectra of C 1s for (a) bare $LiCoO_2$, (b) $AlPO_4$-coated $LiCoO_2$, and (c) Li_2CO_3.

(c)

$\times 10^2$

Li$_2$CO$_3$

CPS

hydrocarbon
contamination

C 1s
in
Li$_2$CO$_3$

Binding Energy (eV)
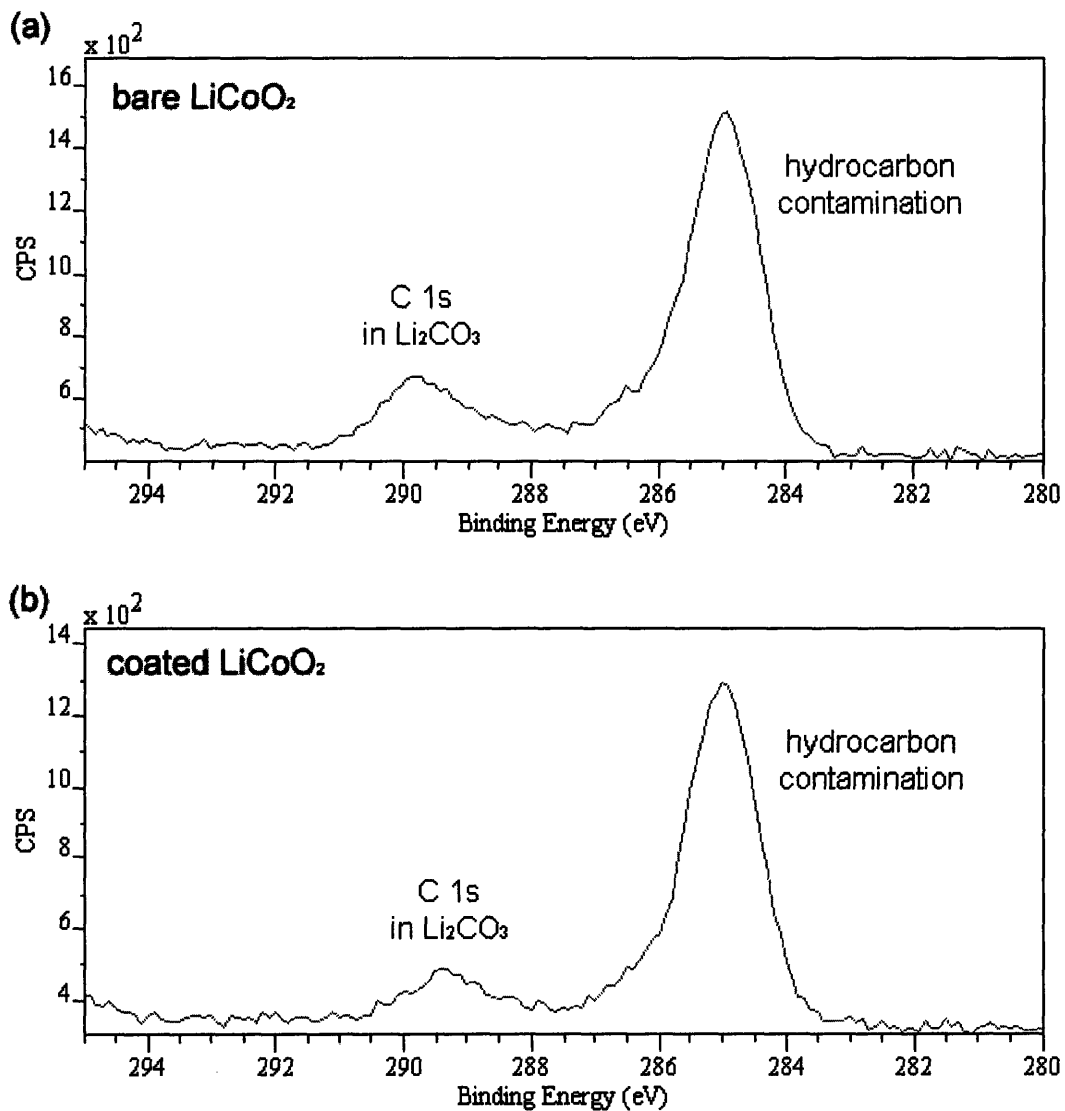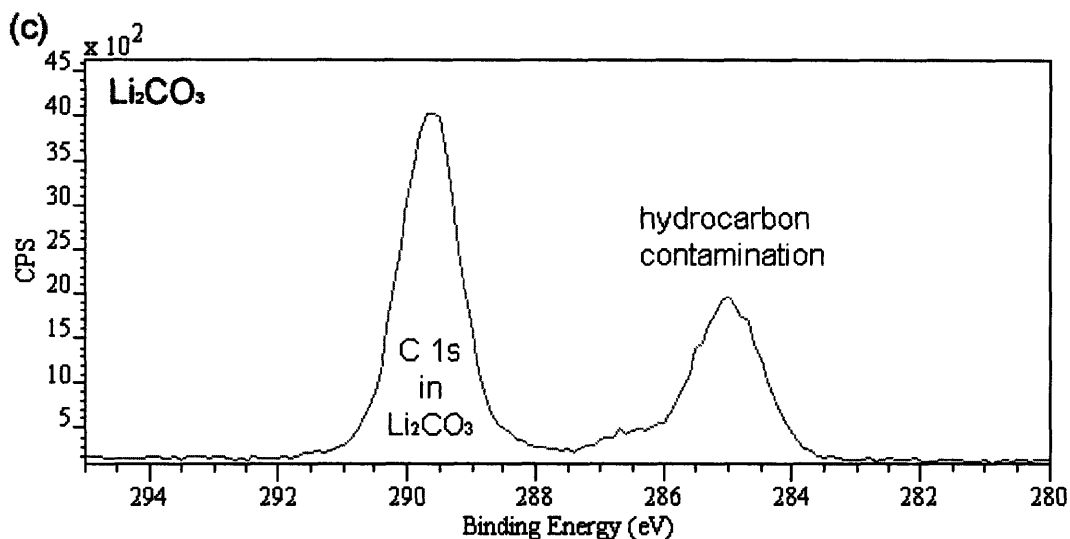
In Figure 29, the spectra containing Li 1s and Co 3p peaks can be seen for the three examined samples. The Co 3p peak appears at 61 eV, which agrees with peak positions reported in the literature [73]. Previous studies have also shown a Li 1s peak at 54.3 eV for LiCoO$_2$, at 55.2 eV for Li$_2$CO$_3$, and at 54.7 eV for LiOH [73, 75]. Since the large peaks shown in Figure 29 a and b occur at approximately 54.2 eV, they can be attributed to Li in LiCoO$_2$. The small deviation from the reported value can be ascribed to the calibration uncertainties described previously. The spectrum for AlPO$_4$-coated LiCoO$_2$ in Figure 29b also contains a small peak at 49.7 eV, whose identity is presently ambiguous. A peak in this energy range is typically assigned to Mg 2p3/2; however, because magnesium was not involved in any of the preparation processes for this coated material, and no further evidence of magnesium can be found in the full-range XPS survey spectrum nor the EDX spectra collected during STEM analysis, the attribution of this peak to a magnesium impurity is somewhat unsupported. A possible assignment of the peak may be to Li 1s with a shift in binding energy due to a bonding environment

different from $LiCoO_2$. More detailed examination of this peak through high-resolution XPS is necessary to fully characterize it.

The Li 1s spectrum for Li_2CO_3 in Figure 29c contains a single peak at 54.9 eV. This position is close to the reported value of 55.2 eV for Li_2CO_3 [73, 75]. A peak at this position may also occur in the spectra for bare and coated $LiCoO_2$, but with a small intensity it may be concealed in the broad base of the Li 1s peak for $LiCoO_2$.

Figure 29. XPS spectra of Li 1s for (a) bare LiCoO$_2$, (b) AlPO$_4$-coated LiCoO$_2$, and (c) Li$_2$CO$_3$.

(a)

bare LiCoO$_2$

Co 3p
in LiCoO$_2$

Li 1s
in LiCoO$_2$

(b)

coated LiCoO$_2$

Co 3p
in LiCoO$_2$

Li 1s
in LiCoO$_2$

(c)

Li$_2$CO$_3$

Li 1s in
Li$_2$CO$_3$
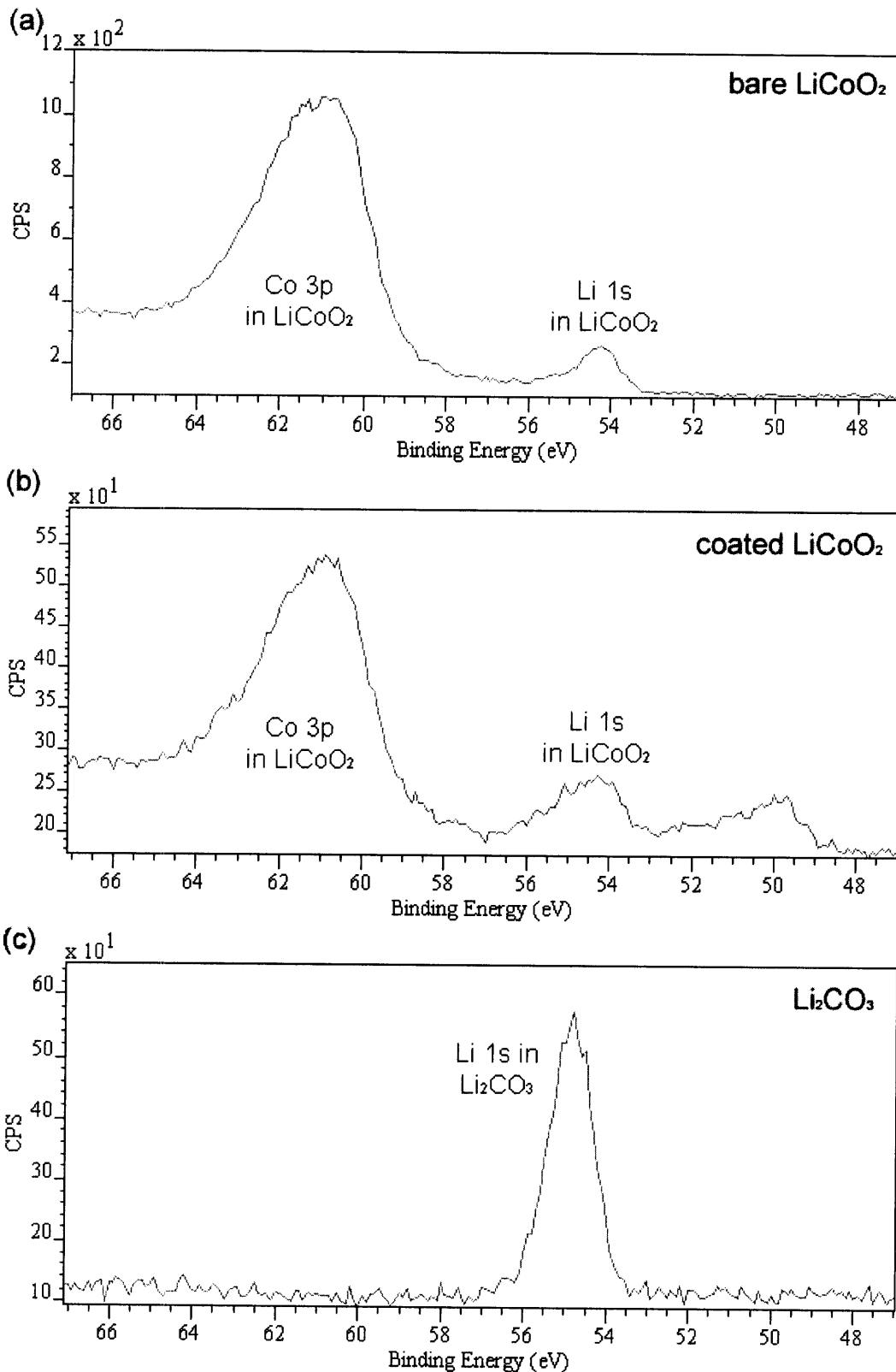
The O 1s spectra yield further information about the differences in surface chemistries for bare and coated $LiCoO_2$, as shown in Figure 30. Both bare and coated materials contain a sharp peak at 529.4 eV, which can be attributed to the O^{2-} ions in the crystalline structure of $LiCoO_2$ [73, 76]. A second broader peak is also seen close to 531.5 eV for bare and coated $LiCoO_2$, and it appears in the same position with higher intensity for the Li_2CO_3 sample. Li_2CO_3 is reported to give a peak for O 1s at 533 eV, suggesting that it partially contributes to the broad peak at 531.5 eV in the $LiCoO_2$ samples. A second contribution of this peak has been reported for $LiCoO_2$ as oxygen atoms with a higher degree of oxidation than O^{2-} and having more Co-O bonds than pure $LiCoO_2$ [75].

Notably, the aforementioned peak at 531.5 eV displays a higher intensity in the $AlPO_4$-coated $LiCoO_2$ than bare $LiCoO_2$. Because $AlPO_4$ has been previously reported by Sherwood et al. to have an O 1s peak at 531.44 eV [77], it is logical that the larger peak may contain a contribution from the coating material, $AlPO_4$. In fact, the intensity of this peak can be seen to decrease during a 1-hour period of sputtering with an argon ion source operated at 2 kV, as shown in Figure 31. This decrease supports the idea that the 531.5 eV peak comes from the coating layer on the surface.

Figure 30. XPS spectra of O 1s for (a) bare LiCoO$_2$, (b) AlPO$_4$-coated LiCoO$_2$, and (c) Li$_2$CO$_3$.

(a)

(c)
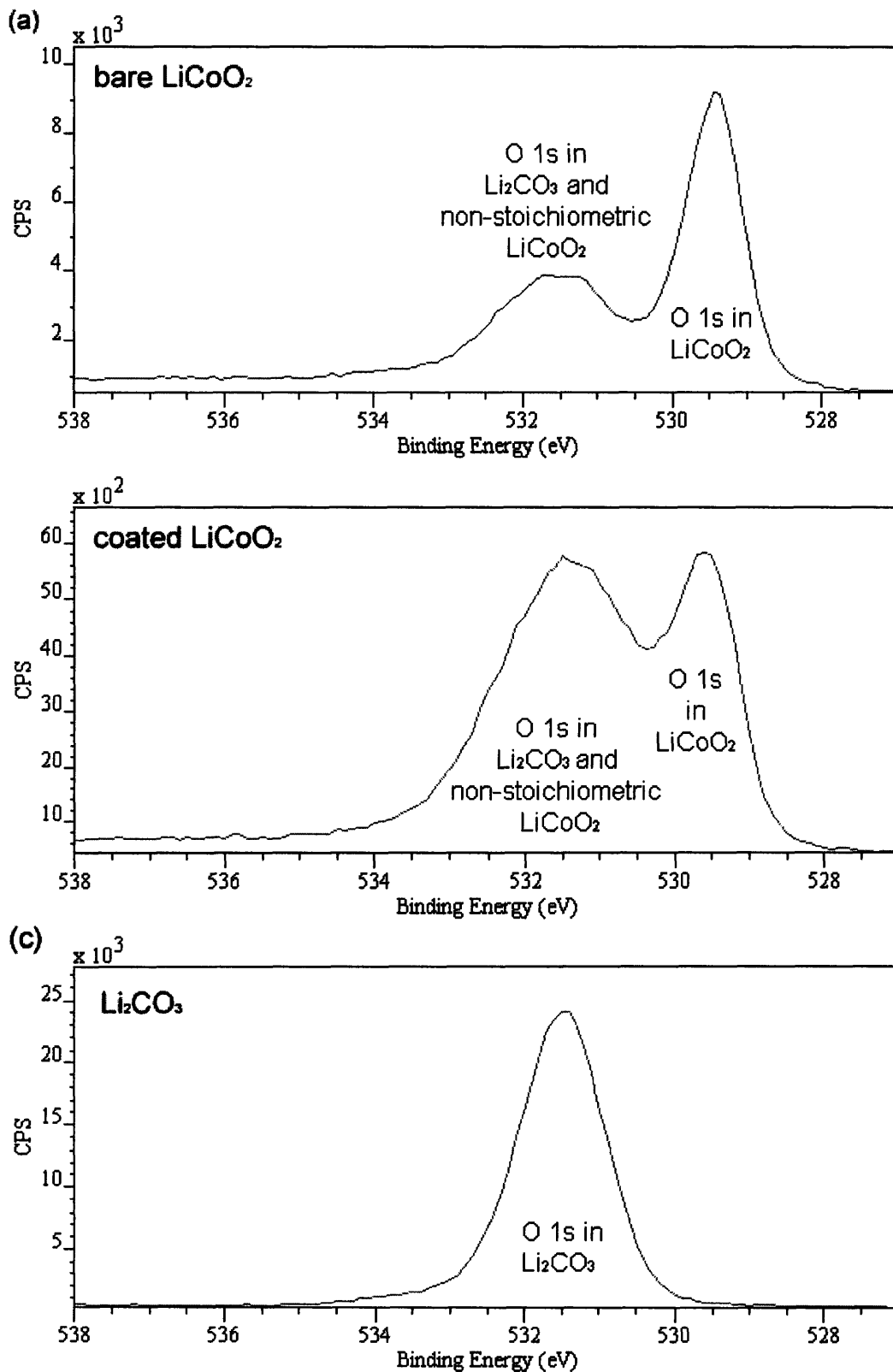
Figure 31. XPS spectra of O 1s for AlPO$_4$-coated LiCoO$_2$ during depth profiling. The spectra are offset in the vertical direction for clarity.
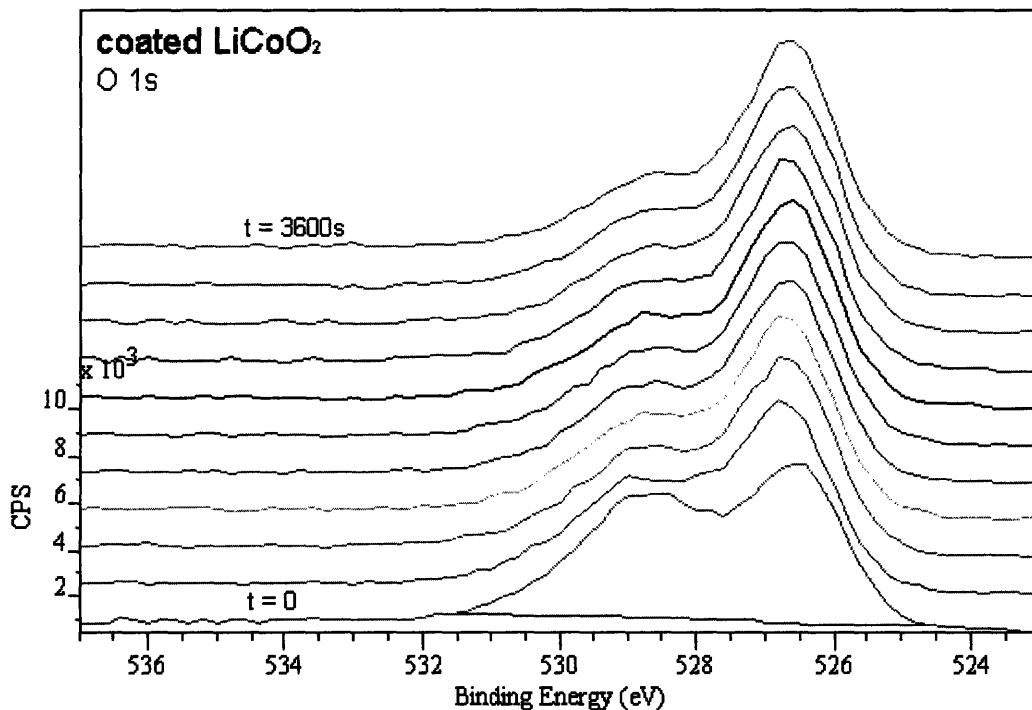
The XPS analysis of AlPO$_4$-coated LiCoO$_2$ also contained evidence of aluminum and phosphorus on the particle surface. Figure 32a shows the Al 2p peak to be located at 73.5 eV. Previous studies have reported the Al 2p peak at 73 eV for Al metal [78], at 74.5 eV for AlPO$_4$ [77], and at a range of values from 73.4 eV to 75.8 eV for various forms of Al$_2$O$_3$ [78, 79]. Therefore, from this experimental data, it is not immediately clear which chemistry of aluminum is present on the surface. It is possible that the aluminum exists in some form of Al$_2$O$_3$, and the peak position appears to fall within the reported range for this compound. However, further XPS measurements of the coated material may be necessary, and preferably compared to a reference sample of AlPO$_4$.

Figure 32b shows the phosphorus peak for $AlPO_4$-coated $LiCoO_2$, located at 133.1 eV. Briggs et al. report a P 2p3/2 peak for $AlPO_4$ to occur at 132.7 eV, which is very close to the value presented here. Other phosphate compounds reported in the literature have peak positions near this value, such as Na_2HPO_4 and KH_2PO_4 [80]. Co 2p3/2 and 2p1/2 peaks were seen at 780 eV and 794.5 eV respectively, for both bare and coated $LiCoO_2$. Given the energy resolution of these XPS measurements, no substantial difference between the peaks from the two samples could be found. In this case, higher resolution XPS studies are recommended.

Depth profiling of $AlPO_4$-coated $LiCoO_2$ for a total of one hour of material removal with an ion source yielded some insight into elemental distribution near the particle surface, as shown in Figure 33. Cobalt concentration increases slightly, while total oxygen level remains relatively constant, although the different oxygen chemistries producing two separate peaks change with depth, as shown in Figure 31 and previously discussed. The amount of phosphorus decays slightly from ~5% to ~3% in this depth range, which is consistent with EDX observations of small, thick phosphorus-rich islands on the surface. Aluminum levels decreased from ~10% to ~3% for the same depth, indicating that aluminum exists in a thinner layer which can be almost entirely removed in one hour of ion sputtering, which further supports the concepts previously discussed regarding EDX and TEM results.

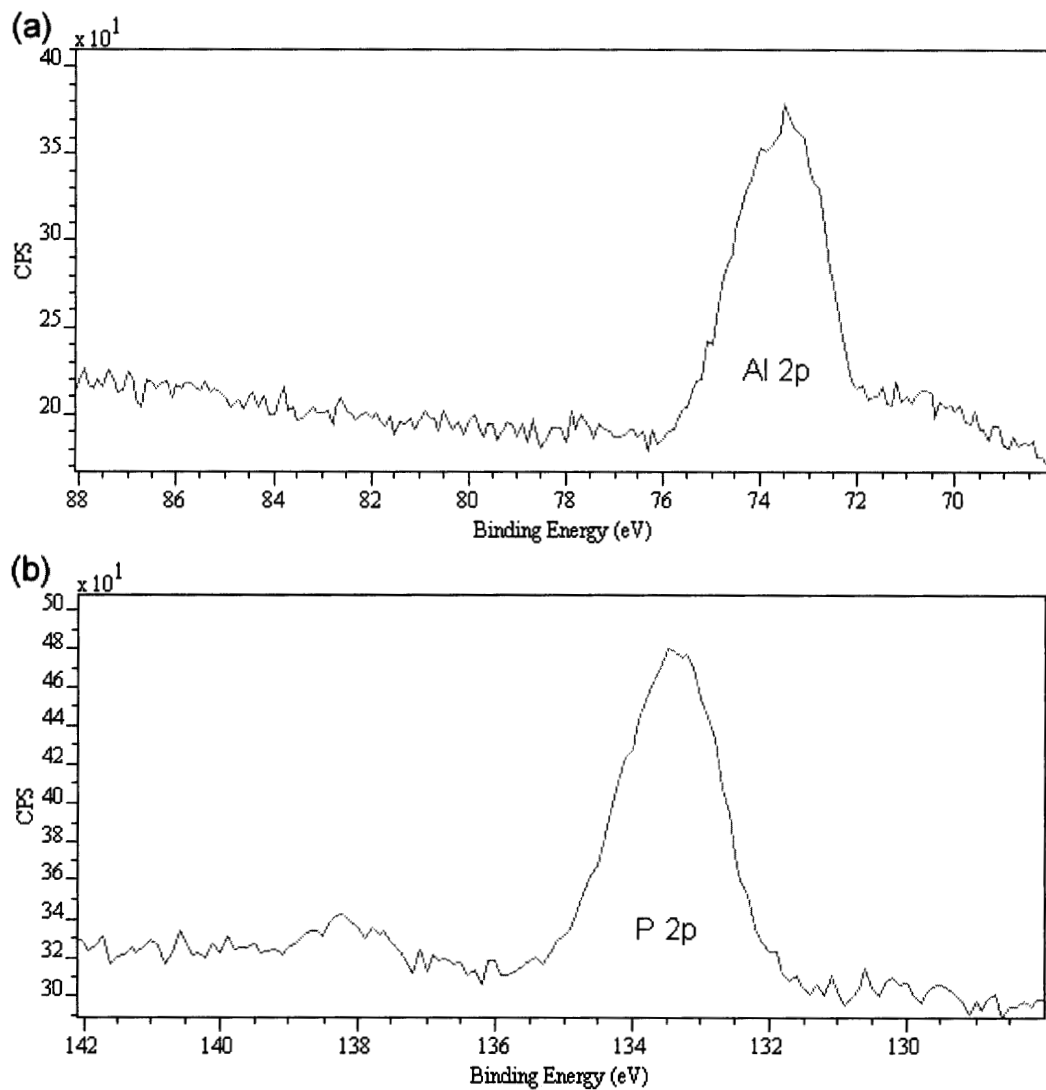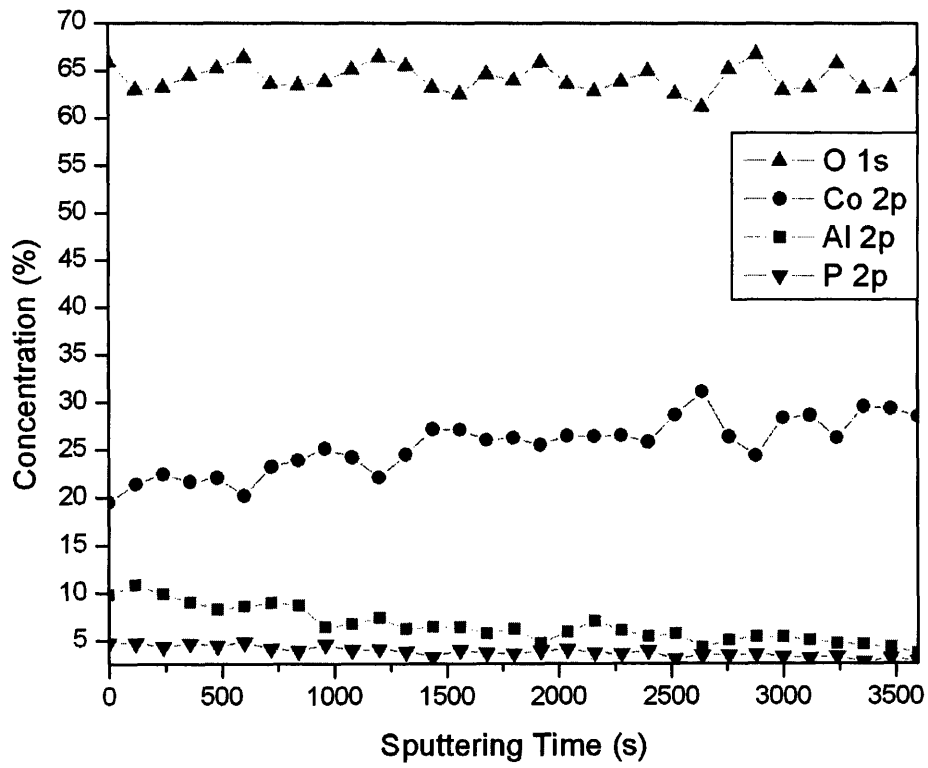Figure 32. XPS spectra of (a) Al 2p and (b) P 2p in AlPO$_4$-coated LiCoO$_2$.

Figure 33. XPS depth profiling from one hour of material removal with argon ion source operated at 150 W.

e. Discussion

The pitted surface texture of the $AlPO_4$-coated $LiCoO_2$ particles as shown by scanning electron micrographs are located only on the faces normal to the layers of the bulk material. This orientation may indicate that the coating layer interacts with the bulk $LiCoO_2$ along the layer edges, which may be more active since the lithium ions deintercalate and enter the electrolyte from those sites. Possible theories include diffusion of the Al into the $LiCoO_2$ bulk to form a solid solution of $LiAl_yCo_{1-y}O_2$, or the diffusion of the excess lithium from the overstoichiometric $LiCoO_2$ out of the layered structure to form a compound such as $LiAlO_2$ or Li_3PO_4 on the surface. $LiAlO_2$ is an electronic insulator, and because the EIS data revealed no significant increase in electronic resistance for the $AlPO_4$-coated material, formation of $LiAlO_2$ is not likely. Given that the phosphorus EDX map typically overlaps the oxygen map, and galvanostatic data indicate outward diffusion of lithium, the formation of Li_3PO_4 is more reasonable. Li_3PO_4 is the precursor for the commonly-used solid electrolyte material known as LiPON, or lithium phosphorus oxynitride (Li_3PO_4-N_x). Synthesis of LiPON involves sputtering Li_3PO_4 in N_2 gas, and the conductivity of the material, on the order of 10^{-6} S/cm increases with nitrogen content of the gas [81]. Li_3PO_4 itself has an ionic conductivity of ~6.3×10^{-8} S/cm [81], and its presence on the surface of the coated $LiCoO_2$ could enhance the transport of Li^+ and the stability of the surface during repeated cycling.

The uniform surface coverage of the coated particles by some form of aluminum may also protect the $LiCoO_2$ from harmful side reactions and reduce Co dissolution. The

aluminum may be in the form of pure Al or Al_2O_3 which might provide a layer of improved electronic conductivity on the $LiCoO_2$ surface. Such a layer might improve electronic contact between particles and inhibit Co dissolution and HF acid attack. The aluminum might also be present along the surface in a thin layer of solid solution with the $LiCoO_2$, in the form of $LiAl_yCo_{1-y}O_2$. Such a layer might serve to slightly increase the charging voltage of the active material, which is also seen in the $AlPO_4$-coated $LiCoO_2$.

XPS results provide further insight to the arrangement of surface species on the coated material. The presence of Li_2CO_3 on bare $LiCoO_2$ may serve to increase its surface impedance and hinder Li^+ transport into the electrolyte. Oxygen spectra show that the coated material has a different oxygen chemistry at the surface which may be more stable to decomposition in the electrolyte than bare $LiCoO_2$, thus maintaining the structural integrity of the particle surface and reducing cobalt dissolution. This oxygen may be part of a phosphate compound, as suggested by the P 2p peak. However, further assessment is needed to determine if a component with the form $Li_xP_yO_z$ is truly present on the surface, given that the low-energy peak in the Li 1s spectrum is as yet unidentified.

The proposed mechanism of the coating structure effect is illustrated schematically in Figure 34. A thin layer of Al-rich coating, possibly in the form of Al_2O_3 or $LiAl_yCo_{1-y}O_2$, covers most of the $LiCoO_2$ particle surface, as supported by EDX and TEM studies, serving to stabilize the layered structure of $LiCoO_2$ at the edges where it is most susceptible to cobalt dissolution during cycling. Although this layer may not be perfectly continuous, the level of coverage it provides is sufficient for significant stability

improvement. Clusters of thicker P-rich coating are dispersed over the particle surface, as suggested by SEM and EDX studies. The excess lithium from the overstoichiometric $LiCoO_2$ starting material has diffused out of the bulk during the coating procedure, as supported by galvanostatic charge-discharge studies, and it may have formed a new compound with the aluminum or phosphate components at the surface, such as Li-Co-Al-O and/or Li-P-O compounds. If these surface layer compounds have a fairly high ionic or electronic conductivity, they might stabilize the surface structure while providing a relatively unhindered pathway for Li^+ deintercalation.

Figure 34. Proposed mechanism and structure of $AlPO_4$-coated $LiCoO_2$.
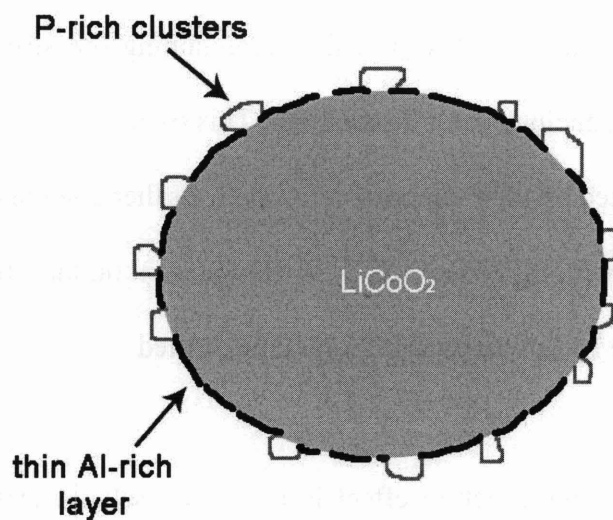
V. Nanoscale Impedance Spectroscopy Using AFM

a. Experimental Considerations

Nanoscale impedance spectroscopy involves application of an ac voltage perturbation between the sample and a conductive AFM tip, as shown schematically in Figure 35. For nanoscale impedance measurements using the AFM, the Veeco Enviroscope system requires a few modifications. The required connections are depicted in Figure 36. A Veeco Signal Access Module (SAM) is inserted between the Nanoscope IIIa controller and the Quadrex extender. The SAM must be inserted after the Quadrex module to avoid sending any high-frequency or high-voltage signals through the Quadrex that might incur damage. The SAM provides access to a variety of signals in the Enviroscope system; specifically, the connections labeled "Ana2" and "Bias" correspond to tip and sample bias respectively. Each connection on the SAM is accompanied by a toggle switch. When toggled to "output", the BNC connection allows measurement of the signal being transmitted by the system. When toggled to "input", the signal chain is broken and a user-defined signal can be applied. In the latter configuration, it is possible to connect the tip and sample to a frequency response analyzer or a potentiostat. This experimental arrangement has been constructed and tested using pin resistors of various values to confirm the continuity of the signal chain by generating simple I-V curves. The measurements from the FRA or potentiostat are recorded by an auxiliary PC computer, using CorrWare or ZView software. This configuration can be used for EIS provided that frequencies used are less than 1 MHz to avoid damaging the system electronics.

Figure 35. Schematic of nanoimpedance AFM experimental setup. $LiCoO_2$ pressed into gold foil is electrically connected to the sample stage. A user-defined signal can be applied between the probe tip and sample stage.
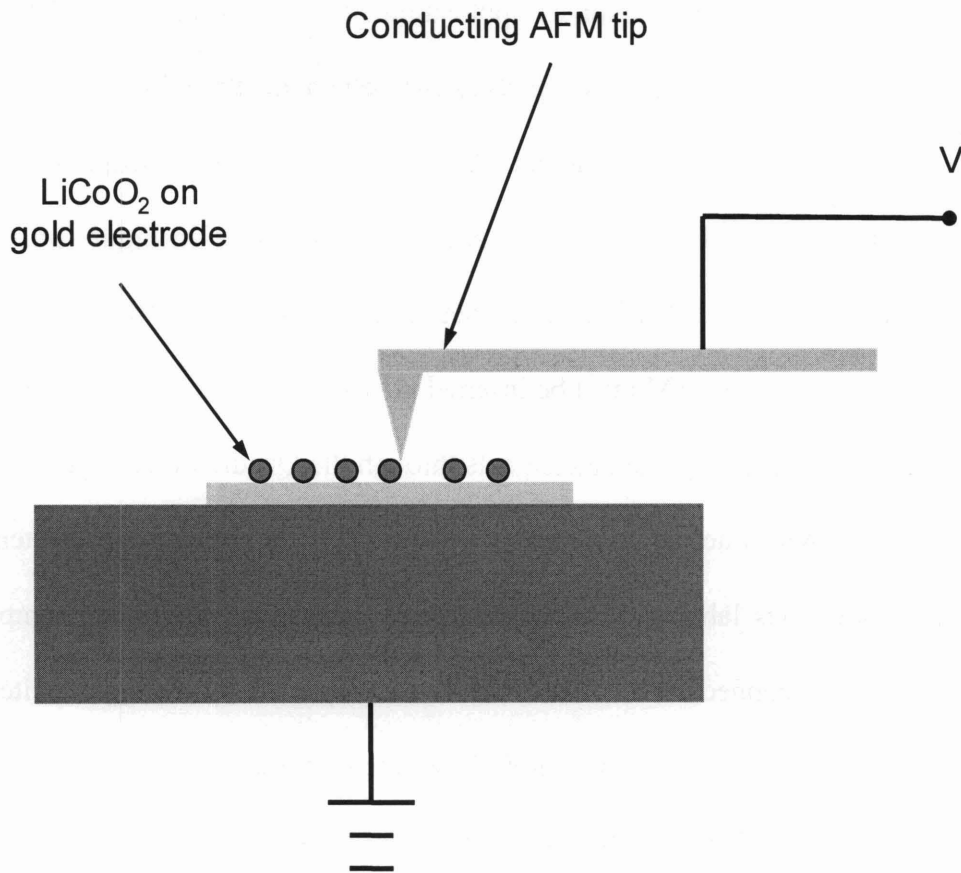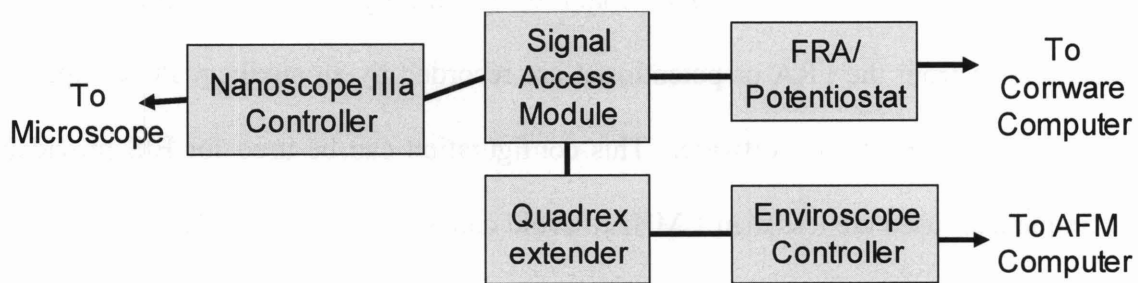

Figure 36. Schematic diagram of component connections for nanoimpedance AFM measurements using the Enviroscope.

The optimization of tip-sample interaction is a critical consideration. Veeco SCM-PIT tips, which are tapping-mode silicon probes coated with 20nm of Pt/Ir, were considered for their conductive coating and high spring constant (k = 2.8 N/m) in comparison to their contact-mode counterparts, SCM-PIC tips (k = 0.2 N/m). When measuring soft samples, these tips may be suitable, since there is little risk of damaging the tip from repeated scanning at high applied forces. However, for harder samples including $LiCoO_2$, the SCM-PIT tips are not sufficiently hard or stiff. Due to the high applied forces required for electrical contact, a much higher spring constant is required, of >10 N/m [66], as well as a more robust coating material with greater hardness, such as doped diamond. Consequently, Veeco DDESP doped diamond-coated probes (k = 42 N/m) were required for measurements on gold and $LiCoO_2$ samples.

b. Preliminary Measurements

The experimental setup was first tested with a test sample with known response, gold foil. Because gold has a purely resistive response, it was suitable for determination of the necessary deflection setpoint and corresponding applied force to obtain good electrical contact. The dependence of resistance on deflection setpoint for the DDESP tip was measured to determine the appropriate deflection setpoint for reliable measurements, and results are shown in Figure 37. Nanoimpedance spectroscopy yielded a repeatable resistive response at ~3 kΩ when measured at setpoints above ~1.0V, which correlated well with the tip resistance of doped diamond coated tips as reported by O'Hayre et al. [66]. In order to prolong the life of the tip, surface scanning prior to impedance

measurements was conducted at a lower setpoint of 0.6V, which provided optimal surface tracking for high quality images.

Figure 37. Change in resistance measured on gold foil substrate with DDESP doped-diamond coated probe tip in contact mode with varying deflection setpoints. Higher deflection setpoint corresponds to higher applied force. High-frequency instabilities occurred at setpoints above 2.0V.
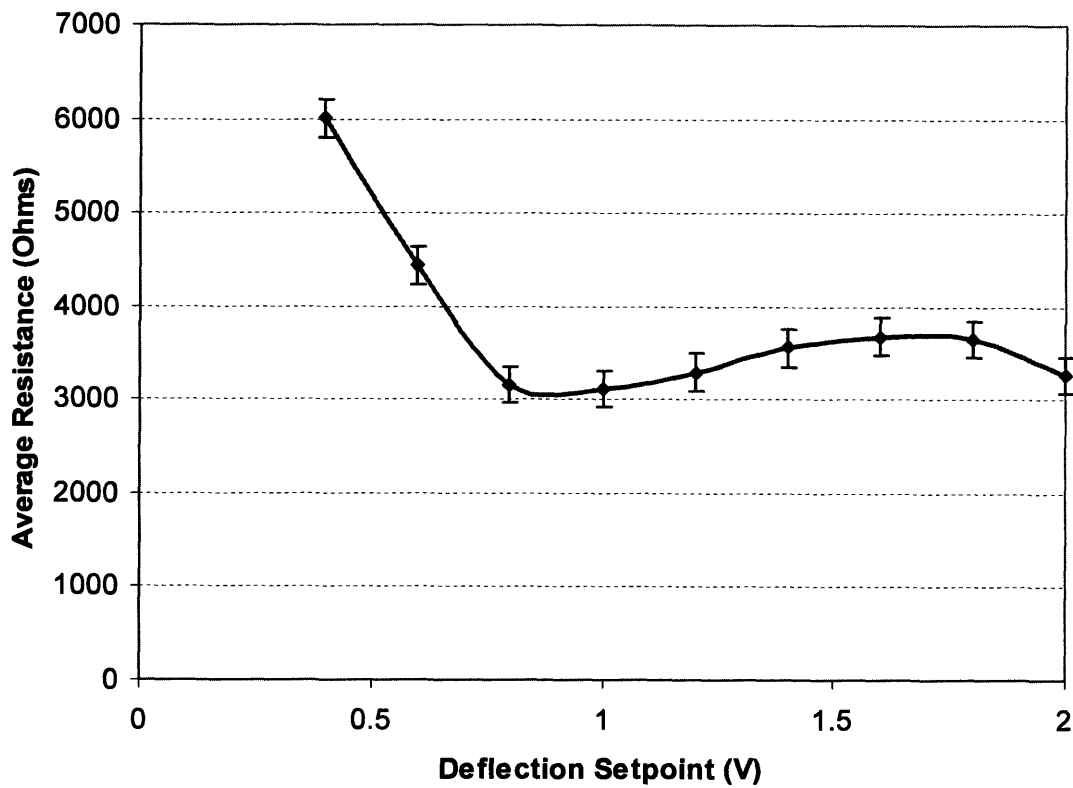
The surface structure of the DDESP probe tip after several measurement sessions is shown in Figure 38, and it appears to have suffered no damage during use. Due to the high cost of these doped diamond-coated tips, Ti-Pt coated probe tips with high spring constant of k = 40 N/m (NSC15 Ti-Pt, MikroMasch) were tested on the gold substrate. The initial response yielded a ~5kW resistance, and subsequent measurements deteriorated with high noise levels and capacitive behavior. After SEM observation of the used probe tip, shown in Figure 39, it became clear that the Ti-Pt coating was not robust enough to sustain the high contact forces required for nanoimpedance measurement. However, the rapidity with which the tip damage occurred was unexpected, since the probe tip is stationary, not scanning, during the EIS tests.

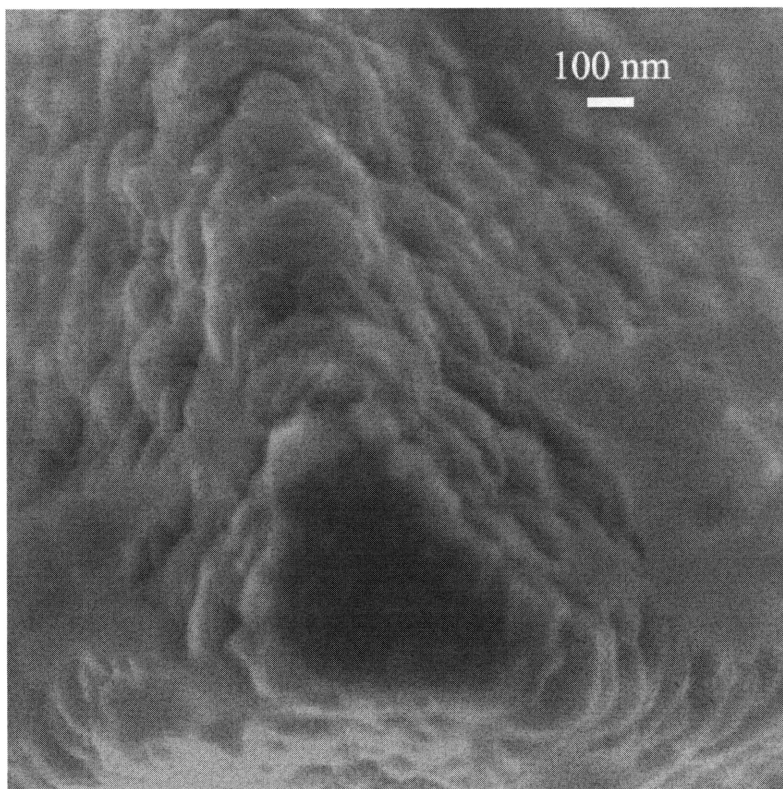Figure 38. Undamaged doped diamond-coated cantilever tip (DDESP, Veeco) after nanoimpedance measurements on gold foil and $LiCoO_2$.
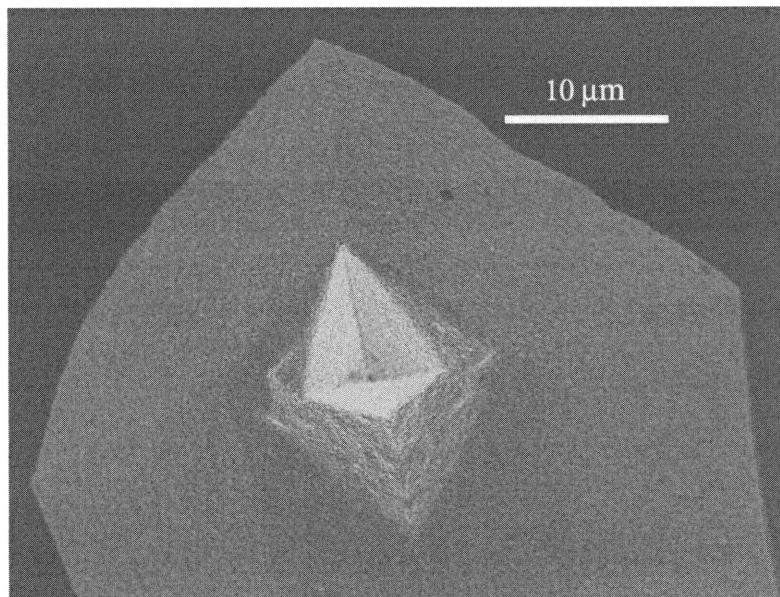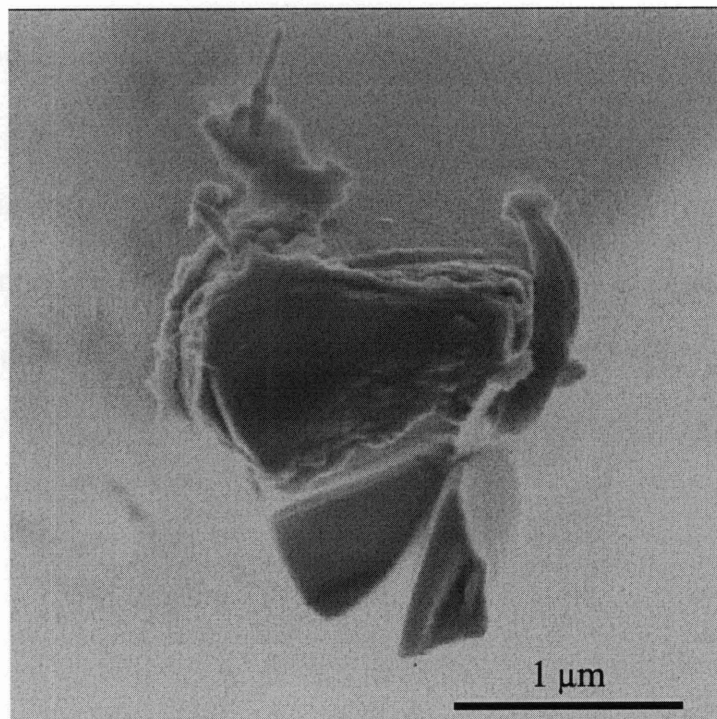
Figure 39. Ti-Pt coated cantilever tip (NSC15, Mikromasch) after nanoimpedance measurements on gold foil and LiCoO$_2$.
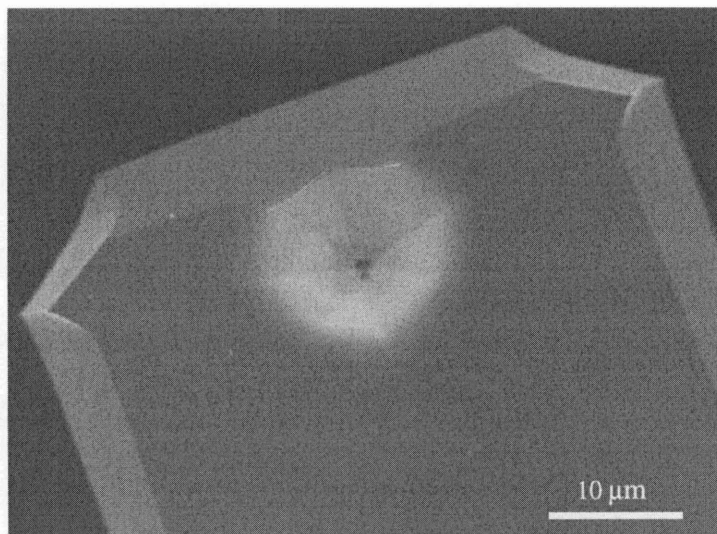
Next, nanoimpedance measurements were conducted on a sample of $LiCoO_2$ particles pressed into gold foil. Using a low tip-sample force of 0.5V, the sample surface was imaged until a suitable $LiCoO_2$ particle was found, shown in Figure 40. The scan size was repeatedly decreased until the tip was stationary, in contact with the top face of the particle. Impedance spectra were collected at setpoints greater than or equal to 1.0V, to determine the appropriate settings for the lowest noise and repeatability. Due to the high magnitude of impedance measured on the $LiCoO_2$, the Solartron 1296 dielectric interface was required to increase the measurement range of the Solartron 1260 impedance/gain-phase analyzer. The results of these measurements are shown in Figure 41. The Nyquist plot shows a single semicircle with a diameter on the order of 10^7 Ω, with low frequencies dominated by noise. The magnitude of the semicircle diameter decreased with increasing setpoint, indicating that better contact was achieved with higher applied forces. However, no measurements were taken above 2.0V due to limitations of the cantilever, which produce a high-pitched ringing noise at such setpoints, usually indicative of oscillation instability. Further optimization is needed to reduce the level of noise in the data, and to ensure repeatable measurements.

Figure 40. A bare LiCoO$_2$ particle pressed into gold foil and studied using nanoimpedance spectroscopy. Results for EIS measurements are given in Figure 41.
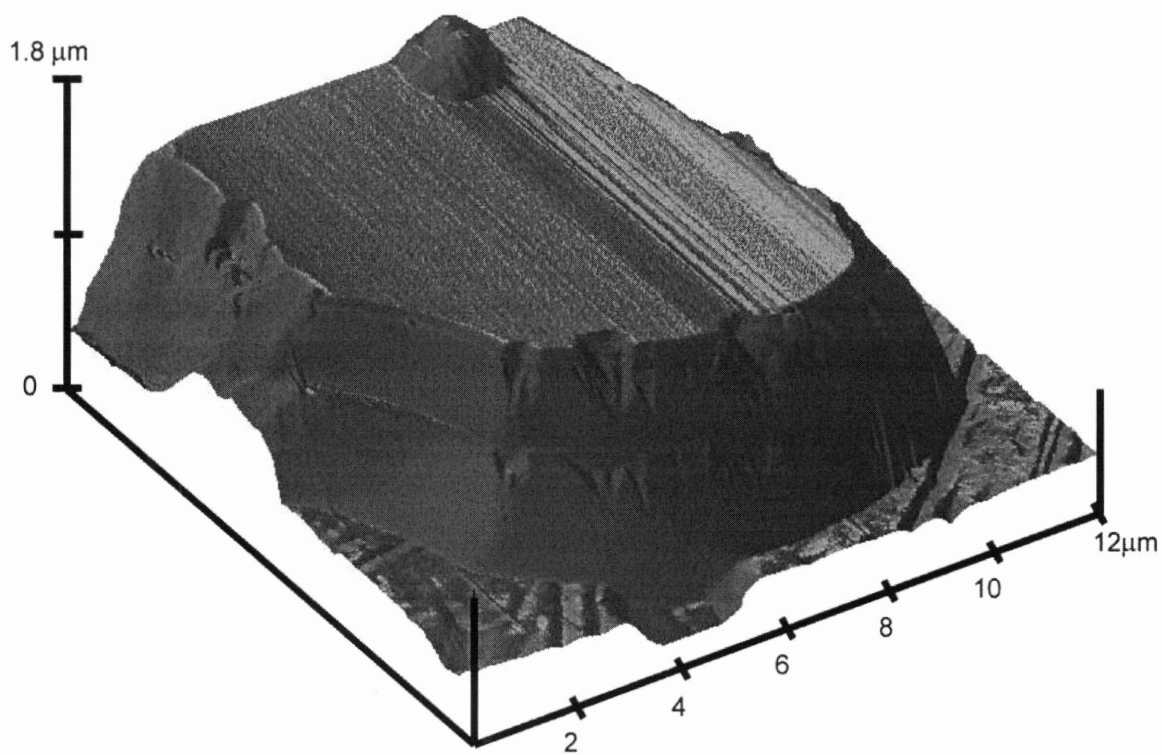
Figure 41. Dependence of EIS response on applied force as related to deflection setpoint of doped diamond-coated AFM tip (DDESP, Veeco) on bare $LiCoO_2$ particle. Large magnitude of impedance approached the limitations of the frequency response analyzer, and noise levels at low frequencies were problematic.
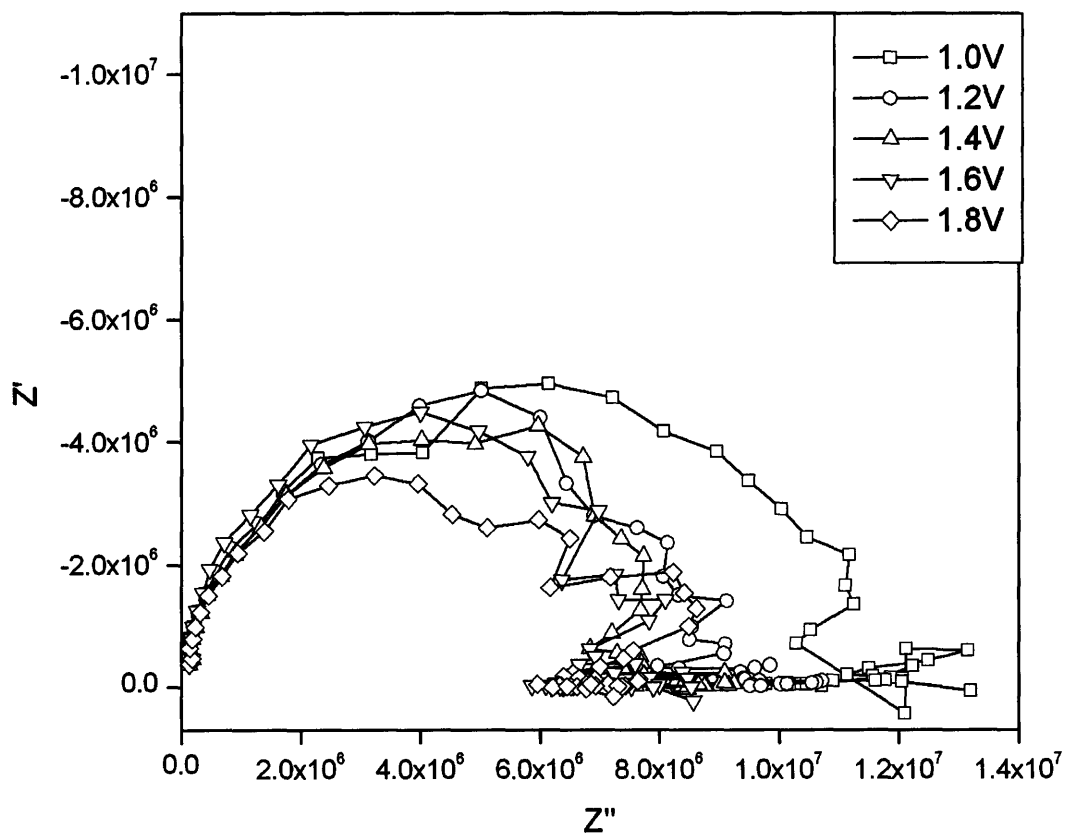
c. Recommendations for Further Development

Further improvement is necessary for the nanoimpedance spectroscopy technique to yield repeatable measurements that can provide insight to the differences between various cathode materials. Doped-diamond coated probe tips with a spring constant $k = \sim 40$ N/m are optimal for good electrical contact with the sample. To accurately measure the difference between two electrode materials, the noise level must be decreased to obtain a reasonable degree of precision.

While the described experimental design may yield interesting results into the conductivity of electrode materials alone, they must be studied in a different cell design to replicate the conditions it would experience in a battery cell. This would require constructing a three-electrode cell, with the AFM probe tip contacting a single $LiCoO_2$ particle as its current collector. One cell design might include a lithium metal counter electrode layered on the sample stage with a layer of fritted glass above it. The fritted glass would be soaked in electrolyte and would contain $LiCoO_2$ particles in the small pores, such that they would be electrically separated from the lithium metal. A lithium metal reference electrode could also be placed in contact with the electrolyte.

VI.   Conclusion

The purpose of this work is to understand the role of the $AlPO_4$-nanoparticle coating in improving the electrochemical performance of $LiCoO_2$ between charge voltage limits of 3.0V and 4.7V. The study aims to correlate the microstructure and composition of the coating layer to its effects in stabilizing $LiCoO_2$ both structurally and thermally at high voltages.

The improved electrochemical and thermal effects of a nanometer-scale coating of $AlPO_4$ on $LiCoO_2$ are elucidated by SEM and TEM microstructural studies which reveal the unique interaction of the coating material with the active sites at the layer edges of $LiCoO_2$. Elemental mapping reveals the non-uniform distribution of Al and P in the coating layer, such that Al is present in a thin coating layer which covers the surface more evenly, while P is confined mainly to smaller thick regions of the coating.

Evidence of reversible lithium-vacancy ordering and two distinct phase transitions from O3 to H1-3 to O1 phases seen only in the $AlPO_4$-coated $LiCoO_2$ indicate that excess lithium may diffuse out of the bulk structure during the coating procedure and interact with the $AlPO_4$ coating layer, leaving stoichiometric $LiCoO_2$ in the bulk. Preliminary EIS data shows the electronic resistance decreases at different rates upon initial deintercalation, corresponding with the degree of slope for the coated and bare materials' voltage profiles on charging to reach the 3.93V plateau. Both coated and bare materials show a subsequent rise in electronic resistance at voltages which correspond to the O3 to H1-3 phase transition, indicating that the H1-3 phase has a higher impedance than the O3

phase, which may be linked to the performance deterioration of $LiCoO_2$ when cycled to high voltages.

The proposed mechanism of coating structure and performance enhancement consists of a thin aluminum-rich layer covering most of the $LiCoO_2$ particle surface, with thicker islands of phosphorus-rich material. The aluminum layer may act to stabilize the $LiCoO_2$ structure from reaction with electrolyte species and cobalt dissolution. Because the galvanostatic voltage profiles indicate that excess lithium from overstoichiometric $LiCoO_2$ has diffused out of the bulk during the coating process, this lithium may have formed a compound with the aluminum or phosphate components of the coating layer. The possibility of a Li-P-O compound at the surface may increase the ionic conductivity of the surface layer while stabilizing the $LiCoO_2$ from side reactions.

In order to confirm and enhance the proposed mechanism, high-energy XPS studies will be conducted to further clarify the nature of the surface chemistries. Future work will also include validation of the electrochemical impedance spectroscopy results with a three-electrode cell, which will also allow for comprehensive analysis of the high-frequency semicircle data, providing insight into the charge-transfer and surface layer properties of bare and coated $LiCoO_2$.

Acknowledgments

References

1.   J. N. Reimers and J. R. Dahn, Electrochemical and Insitu X-Ray-Diffraction Studies of Lithium Intercalation in Li_xCoO_2. Journal of the Electrochemical Society, 1992. 139(8): p. 2091-2097.

2.   J. N. Reimers, J. R. Dahn and U. Vonsacken, Effects of Impurities on the Electrochemical Properties of $LiCoO_2$. Journal of the Electrochemical Society, 1993. 140(10): p. 2752-2754.

3.   M. Yoshio, H. Tanaka, K. Tominaga and H. Noguchi, Synthesis of $LiCoO_2$ from Cobalt Organic-Acid Complexes and Its Electrode Behavior in a Lithium Secondary Battery. Journal of Power Sources, 1992. 40(3): p. 347-353.

4.   H. J. Orman and P. J. Wiseman, Cobalt(Iii) Lithium-Oxide, $CoLiO_2$ - Structure Refinement by Powder Neutron-Diffraction. Acta Crystallographica Section C-Crystal Structure Communications, 1984. 40(JAN): p. 12-14.

5.   K. Mizushima, P. C. Jones, P. J. Wiseman and J. B. Goodenough, Li_xCoO_2 (0<x<=1) : a new cathode material for batteries of high energy density. Materials Research Bulletin, 1980. 15: p. 783-789.

6.   A. Van der Ven, M. K. Aydinol, G. Ceder, G. Kresse and J. Hafner, First-principles investigation of phase stability in Li_xCoO_2. Physical Review B, 1998. 58(6): p. 2975-2987.

7.   Y. Shao-Horn, F. Weill, L. Croguennec, D. Carlier, M. Menetrier and C. Delmas, Lithium and vacancy ordering in T(#)2-Li_xCoO_2 derived from O2-type $LiCoO_2$. Chemistry of Materials, 2003. 15(15): p. 2977-2983.

8.   T. Ohzuku and A. Ueda, Solid-State Redox Reactions of $LiCoO_2$ (R(3)over-Bar-M) for 4 Volt Secondary Lithium Cells. Journal of the Electrochemical Society, 1994. 141(11): p. 2972-2977.

9.   E. Plichta, S. Slane, M. Uchiyama, M. Salomon, D. Chua, W. B. Ebner and H. W. Lin, An Improved Li/Li_xCoO_2 Rechargeable Cell. Journal of the Electrochemical Society, 1989. 136(7): p. 1865-1869.

10.   S. Levasseur, M. Menetrier, E. Suard and C. Delmas, Evidence for structural defects in non-stoichiometric HT-$LiCoO_2$: electrochemical, electronic properties and ^{7}Li NMR studies. Solid State Ionics, 2000. 128(1-4): p. 11-24.

11.   G. G. Amatucci, J. M. Tarascon and L. C. Klein, Cobalt dissolution in $LiCoO_2$-based non-aqueous rechargeable batteries. Solid State Ionics, 1996. 83: p. 167-173.

12.   D. Aurbach, B. Markovsky, A. Rodkin, M. Cojocaru, E. Levi and H. J. Kim, An analysis of rechargeable lithium-ion batteries after prolonged cycling. Electrochimica Acta, 2002. 47(12): p. 1899-1911.

13.   H. Maleki, G. P. Deng, A. Anani and J. Howard, Thermal stability studies of Li-ion cells and components. Journal of the Electrochemical Society, 1999. 146(9): p. 3224-3229.

14.   H. Maleki, S. Al Hallaj, J. R. Selman, R. B. Dinwiddie and H. Wang, Thermal properties of lithium-ion battery and components. Journal of the Electrochemical Society, 1999. 146(3): p. 947-954.

15.   J. R. Dahn, E. W. Fuller, M. Obrovac and U. von Sacken, Thermal stability of Li_xCoO_2, Li_xNiO_2 and λ-MnO_2 and consequences for the safety of Li-ion cells. Solid State Ionics, 1994. 69(3-4): p. 265-270.

16.   P. Biensan, B. Simon, J. P. Peres, A. de Guibert, M. Broussely, J. M. Bodet and F. Perton, On safety of lithium-ion cells. Journal of Power Sources, 1999. 82: p. 906-912.

17.   R. A. Leising, M. J. Palazzo, E. S. Takeuchi and K. J. Takeuchi, Abuse testing of lithium-ion batteries - Characterization of the overcharge reaction of $LiCoO_2$/graphite cells. Journal of the Electrochemical Society, 2001. 148(8): p. A838-A844.

18.   Y. I. Jang, B. Y. Huang, H. F. Wang, D. R. Sadoway, G. Ceder, Y. M. Chiang, H. Liu and H. Tamura, $LiAl_yCo_{1-y}O_2$ (R(3)over-bar-m) intercalation cathode for rechargeable lithium batteries. Journal of the Electrochemical Society, 1999. 146(3): p. 862-868.

19.   H. Tukamoto and A. R. West, Electronic conductivity of $LiCoO_2$ and its enhancement by magnesium doping. Journal of the Electrochemical Society, 1997. 144(9): p. 3164-3168.

20.   S. Levasseur, M. Menetrier and C. Delmas, On the dual effect of Mg doping in $LiCoO_2$ and $Li_{1+delta}CoO_2$: Structural, electronic properties, and ^7Li MAS NMR studies. Chemistry of Materials, 2002. 14(8): p. 3584-3590.

21.   S. Levasseur, M. Menetrier and C. Delmas, Combined effects of Ni and Li doping on the phase transitions in Li_xCoO_2 - Electrochemical and ^7Li nuclear magnetic resonance studies. Journal of the Electrochemical Society, 2002. 149(12): p. A1533-a1540.

22.   G. Ceder, Y. M. Chiang, D. R. Sadoway, M. K. Aydinol, Y. I. Jang and B. Huang, Identification of cathode materials for lithium batteries guided by first-principles calculations. Nature, 1998. 392(6677): p. 694-696.

23.   S. T. Myung, K. Izumi, S. Komaba, Y. K. Sun, H. Yashiro and N. Kumagai, Role of alumina coating on Li-Ni-Co-Mn-O particles as positive electrode material for lithium-ion batteries. Chemistry of Materials, 2005. 17(14): p. 3695-3704.

24.   Y. J. Kim, J. P. Cho, T. J. Kim and B. Park, Suppression of cobalt dissolution from the $LiCoO_2$ cathodes with various metal-oxide coatings. Journal of the Electrochemical Society, 2003. 150(12): p. A1723-A1725.

25.   J. Cho, Y. J. Kim, T. J. Kim and B. Park, Zero-strain intercalation cathode for rechargeable Li-ion cell. Angewandte Chemie-International Edition, 2001. 40(18): p. 3367+.

26.   S. Oh, J. K. Lee, D. Byun, W. I. Cho and B. W. Cho, Effect of Al_2O_3 coating on electrochemical performance of $LiCoO_2$ as cathode materials for secondary lithium batteries. Journal of Power Sources, 2004. 132(1-2): p. 249-255.

27.   J. Cho, Y. J. Kim and B. Park, $LiCoO_2$ cathode material that does not show a phase transition from hexagonal to monoclinic phase. Journal of the Electrochemical Society, 2001. 148(10): p. A1110-a1115.

28.   Z. H. Chen and J. R. Dahn, Studies of $LiCoO_2$ coated with metal oxides. Electrochemical and Solid State Letters, 2003. 6(11): p. A221-A224.

29.   G. T. K. Fey, C. Z. Lu, J. D. Huang, T. P. Kumar and Y. C. Chang, Nanoparticulate coatings for enhanced cyclability of $LiCoO_2$ cathodes. Journal of Power Sources, 2005. 146(1-2): p. 65-70.

30.   J. Cho, Stabilization of spinel-like phase transformation of o-$LiMnO_2$ during 55 degrees C cycling by sol-gel coating of CoO. Chemistry of Materials, 2001. 13(12): p. 4537-4541.

31.   H. Cao, B. J. Xia, Y. Zhang and N. X. Xu, $LiAlO_2$-coated $LiCoO_2$ as cathode material for lithium ion batteries. Solid State Ionics, 2005. 176(9-10): p. 911-914.

32. H. L. Zhao, G. Ling, W. H. Qiu and X. H. Zhang, Improvement of electrochemical stability of $LiCoO_2$ cathode by a nano-crystalline coating. Journal of Power Sources, 2004. 132(1-2): p. 195-200.

33. J. Cho, Y. W. Kim, B. Kim, J. G. Lee and B. Park, A breakthrough in the safety of lithium secondary batteries by coating the cathode material with $AlPO_4$ nanoparticles. Angewandte Chemie-International Edition, 2003. 42(14): p. 1618-1621.

34. J. Kim, M. Noh, J. Cho, H. Kim and K. B. Kim, Controlled nanoparticle metal phosphates (metal = Al, Fe, Ce, and Sr) coatings on $LiCoO_2$ cathode materials. Journal of the Electrochemical Society, 2005. 152(6): p. A1142-A1148.

35. J. Cho, T. G. Kim, C. Kim, J. G. Lee, Y. W. Kim and B. Park, Comparison of Al_2O_3- and $AlPO_4$-coated $LiCoO_2$ cathode materials for a Li-ion cell. Journal of Power Sources, 2005. 146(1-2): p. 58-64.

36. H. Omanda, T. Brousse, C. Marhic and D. M. Schleich, Improvement of the thermal stability of $LiNi_{0.8}Co_{0.2}O_2$ cathode by a SiO_x protective coating. Journal of the Electrochemical Society, 2004. 151(6): p. A922-A929.

37. J. Cho, J. G. Lee, B. Kim and B. Park, Effect of P_2O_5 and $AlPO_4$ coating on $LiCoO_2$ cathode material. Chemistry of Materials, 2003. 15(16): p. 3190-3193.

38. Y. Lee, A. J. Woo, K. S. Han, K. S. Ryu, D. Sohn, D. Kim and H. Lee, Solid-state NMR studies of Al-doped and Al_2O_3-coated $LiCoO_2$. Electrochimica Acta, 2004. 50(2-3): p. 491-494.

39. H. Miyashiro, A. Yamanaka, M. Tabuchi, S. Seki, M. Nakayama, Y. Ohno, Y. Kobayashi, Y. Mita, A. Usami and M. Wakihara, Improvement of degradation at elevated temperature and at high state-of-charge storage by ZrO_2 coating on $LiCoO_2$. Journal of the Electrochemical Society, 2006. 153(2): p. A348-a353.

40. G. T. K. Fey, Z. X. Weng, J. G. Chen, C. Z. Lu, T. P. Kumar, S. P. Naik, A. S. T. Chiang, D. C. Lee and J. R. Lin, Preformed boehmite nanoparticles as coating materials for long-cycling $LiCoO_2$. Journal of Applied Electrochemistry, 2004. 34(7): p. 715-722.

41. J. Cho, Correlation between $AlPO_4$ nanoparticle coating thickness on $LiCoO_2$ cathode and thermal stability. Electrochimica Acta, 2003. 48(19): p. 2807-2811.

42.   J. Cho, Dependence of $AlPO_4$ coating thickness on overcharge behaviour of $LiCoO_2$ cathode material at 1 and 2 C rates. Journal of Power Sources, 2004. 126(1-2): p. 186-189.

43.   J. P. Cho, B. Kim, J. G. Lee, Y. W. Kim and B. Park, Annealing-temperature effect on various cutoff-voltage electrochemical performances in $AlPO_4$-Nanoparticle-Coated $LiCoO_2$. Journal of the Electrochemical Society, 2005. 152(1): p. A32-A36.

44.   B. Kim, J. G. Lee, M. Choi, J. Cho and B. Park, Correlation between local strain and cycle-life performance of $AlPO_4$-coated $LiCoO_2$ cathodes. Journal of Power Sources, 2004. 126(1-2): p. 190-192.

45.   J. Cho, J. G. Lee, B. Kim, T. G. Kim, J. Kim and B. Park, Control of $AlPO_4$-nanoparticle coating on $LiCoO_2$ by using water or ethanol. Electrochimica Acta, 2005. 50(20): p. 4182-4187.

46.   J. G. Lee, B. Kim, J. Cho, Y. W. Kim and B. Park, Effect of $AlPO_4$-nanoparticle coating concentration on high-cutoff-voltage electrochemical performances in $LiCoO_2$. Journal of the Electrochemical Society, 2004. 151(6): p. A801-A805.

47.   Z. H. Chen and J. R. Dahn, Methods to obtain excellent capacity retention in $LiCoO_2$ cycled to 4.5 V. Electrochimica Acta, 2004. 49(7): p. 1079-1090.

48.   H. S. Liu, Z. R. Zhang, Z. L. Gong and Y. Yang, A comparative study of $LiNi_{0.8}Co_{0.2}O_2$ cathode materials modified by lattice-doping and surface-coating. Solid State Ionics, 2004. 166(3-4): p. 317-325.

49.   G. T. K. Fey, H. Z. Yang, T. P. Kumar, S. P. Naik, A. S. T. Chiang, D. C. Lee and J. R. Lin, A simple mechano-thermal coating process for improved lithium battery cathode materials. Journal of Power Sources, 2004. 132(1-2): p. 172-180.

50.   E. Barsoukov, J. H. Kim, D. H. Kim, K. S. Hwang, C. O. Yoon and H. Lee, Parametric analysis using impedance spectroscopy: relationship between material properties and battery performance. Journal of New Materials for Electrochemical Systems, 2000. 3(4): p. 301-308.

51.   D. Aurbach, M. D. Levi, E. Levi, H. Teller, B. Markovsky, G. Salitra, U. Heider and L. Heider, Common electroanalytical behavior of Li intercalation processes into graphite and transition metal oxides. Journal of the Electrochemical Society, 1998. 145(9): p. 3024-3034.

52.   F. Nobili, F. Croce, B. Scrosati and R. Marassi, Electronic and electrochemical properties of $Li_xNi_{1-y}Co_yO_2$ cathodes studied by impedance spectroscopy. Chemistry of Materials, 2001. 13(5): p. 1642-1646.

53.   F. Nobili, R. Tossici, R. Marassi, F. Croce and B. Scrosati, An AC impedance spectroscopic study of Li_xCoO_2 at different temperatures. Journal of Physical Chemistry B, 2002. 106(15): p. 3909-3915.

54.   F. Nobili, S. Dsoke, F. Croce and R. Marassi, An ac impedance spectroscopic study of Mg-doped $LiCoO_2$ at different temperatures: electronic and ionic transport properties. Electrochimica Acta, 2005. 50(11): p. 2307-2313.

55.   P. G. Bruce and M. Y. Saidi, The Mechanism of Electrointercalation. Journal of Electroanalytical Chemistry, 1992. 322(1-2): p. 93-105.

56.   W. Weppner and R. A. Huggins, Determination of Kinetic-Parameters of Mixed-Conducting Electrodes and Application to System Li_3Sb. Journal of the Electrochemical Society, 1977. 124(10): p. 1569-1578.

57.   B. C. Han, A. Van der Ven, D. Morgan and G. Ceder, Electrochemical modeling of intercalation processes with phase field models. Electrochimica Acta, 2004. 49(26): p. 4691-4699.

58.   P. G. Bruce, A. Lisowskaoleksiak, M. Y. Saidi and C. A. Vincent, Vacancy Diffusion in the Intercalation Electrode $Li_{1-x}NiO_2$. Solid State Ionics, 1992. 57(3-4): p. 353-358.

59.   Y. I. Jang, B. J. Neudecker and N. J. Dudney, Lithium diffusion in Li_xCoO_2 (0.45 < x < 0.7) intercalation cathodes. Electrochemical and Solid State Letters, 2001. 4(6): p. A74-a77.

60.   H.-W. Ha, K. H. Jeong, N. J. Yun, M. Z. Hong and K. Kim, Effects of surface modification on the cycling stability of $LiNi_{0.8}Co_{0.2}O_2$ electrodes by CeO_2 coating. Electrochimica Acta, 2005. 50(18): p. 3764-3769.

61.   K. M. Shaju, G. V. S. Rao and B. V. R. Chowdari, Li-ion kinetics and polarization effect on the electrochemical performance of $Li(Ni_{1/2}Mn_{1/2})O_2$. Electrochimica Acta, 2004. 49(9-10): p. 1565-1576.

62.   J. P. Cho, H. S. Jung, Y. C. Park, G. B. Kim and H. S. Lim, Electrochemical properties and thermal stability of $Li_aNi_{1-x}Co_xO_2$ cathode materials. Journal of the Electrochemical Society, 2000. 147(1): p. 15-20.

63.   A. Layson, S. Gadad and D. Teeters, Resistance measurements at the nanoscale: scanning probe ac impedance spectroscopy. Electrochimica Acta, 2003. 48(14-16): p. 2207-2213.

64.   S. V. Kalinin and D. A. Bonnell, Scanning impedance microscopy of electroactive interfaces. Applied Physics Letters, 2001. 78(9): p. 1306-1308.

65.   S. V. Kalinin and D. A. Bonnell, Scanning impedance microscopy of an active Schottky barrier diode. Journal of Applied Physics, 2002. 91(2): p. 832-839.

66.   R. O'Hayre, M. Lee and F. B. Prinz, Ionic and electronic impedance imaging using atomic force microscopy. Journal of Applied Physics, 2004. 95(12): p. 8382-8392.

67.   R. O'Hayre, G. Feng, W. D. Nix and F. B. Prinz, Quantitative impedance measurement using atomic force microscopy. Journal of Applied Physics, 2004. 96(6): p. 3540-3549.

68.   Z. X. Wang, C. A. Wu, L. J. Liu, F. Wu, L. Q. Chen and X. J. Huang, Electrochemical evaluation and structural characterization of commercial $LiCoO_2$ surfaces modified with MgO for lithium-ion batteries. Journal of the Electrochemical Society, 2002. 149(4): p. A466-A471.

69.   K. M. Shaju, G. V. S. Rao and B. V. R. Chowdari, Electrochemical kinetic studies of Li-ion in O-2-structured $Li_{2/3}(Ni_{1/3}Mn_{2/3})O_2$ and $Li_{(2/3)+x}(Ni_{1/3}Mn_{2/3})O_2$ by EIS and GITT. Journal of the Electrochemical Society, 2003. 150(1): p. A1-a13.

70.   S. Levasseur, M. Menetrier, Y. Shao-Horn, L. Gautier, A. Audemer, G. Demazeau, A. Largeteau and C. Delmas, Oxygen vacancies and intermediate spin trivalent cobalt ions in lithium-overstoichiometric $LiCoO_2$. Chemistry of Materials, 2003. 15(1): p. 348-354.

71.   A. Van der Ven, G. Ceder, M. Asta and P. D. Tepesch, First-principles theory of ionic diffusion with nondilute carriers. Physical Review B, 2001. 6418(18).

72.   A. Clemencon, A. Appapillai, S. Kumar and Y. Shao-Horn, Atomic Force Microscopy Studies of Surface and Dimensional Changes in Li_xCoO_2 Crystals During Lithium De-intercalation. Chemistry of Materials, 2006. submitted.

73.   R. Alcantara, G. F. Ortiz, P. Lavela, J. L. Tirado, W. Jaegermann and A. Thissen, Rotor blade grinding and re-annealing of LiCoO₂: SEM, XPS, EIS and electrochemical study. Journal of Electroanalytical Chemistry, 2005. 584(2): p. 147-156.

74.   P. Swift, Adventitious Carbon - the Panacea for Energy Referencing. Surface and Interface Analysis, 1982. 4(2): p. 47-51.

75.   J. C. Dupin, D. Gonbeau, H. Benqlilou-Moudden, P. Vinatier and A. Levasseur, XPS analysis of new lithium cobalt oxide thin-films before and after lithium deintercalation. Thin Solid Films, 2001. 384(1): p. 23-32.

76.   T. Miyazaki, T. Doi, M. Kato, T. Miyake and I. Matsuura, Structure and catalysis of layered rock-salt type oxides for methane oxidation. Applied Surface Science, 1997. 121, p. 492-495.

77.   P. M. A. Sherwood, Introduction to studies of aluminum and its compounds by XPS. Surface Science Spectra, 1998. 5(1): p. 1-3.

78.   A. Nylund and I. Olefjord, Surface-Analysis of Oxidized Aluminum .1. Hydration of Al₂O₃ and Decomposition of Al(OH)₃ in a Vacuum as Studied by Esca. Surface and Interface Analysis, 1994. 21(5): p. 283-289.

79.   S. Thomas and P. M. A. Sherwood, Valence Band Spectra of Aluminum-Oxides, Hydroxides, and Oxyhydroxides Interpreted by X-α-Calculations. Analytical Chemistry, 1992. 64(21): p. 2488-2495.

80.   J. F. Moulder and J. Chastain, Handbook of x-ray photoelectron spectroscopy : a reference book of standard spectra for identification and interpretation of XPS data. Physical Electronics Division, Perkin-Elmer Corp., 1992.

81.   X. H. Yu, J. B. Bates, G. E. Jellison and F. X. Hart, A stable thin-film lithium electrolyte: Lithium phosphorus oxynitride. Journal of the Electrochemical Society, 1997. 144(2): p. 524-532.

Appendix. Supporting Data

    a. Electrochemical Impedance Spectroscopy

Figure 42 and Figure 43 show supporting results from different electrode batches tested

in coin cells using EIS as a function of delithiation. The resistance magnitudes vary due

to differing electrode batches and possibly non-uniform thicknesses within a single

electrode, but the overall trends with lithium content are the same and provide support for

the data presented in Chapter III. Error bars in lithium content x included in the plots

serve to indicate the differences in calculated lithium content due to inhomogeneous

cathode utilization and small weighing errors. Different scales in the y-axis are used in

Figures 31a and 31b in order to show more detail at low resistance values while including

data points at high resistances to completely display the trends.

Figure 42. Equivalent circuit fitting for the EIS spectra yields trends in electronic resistance as a function of (a) lithium deintercalation and (b) voltage in bare Li_xCoO_2 for electrode batch B3. X-error bars are included in (a) to indicate the effect of weighing errors and nonuniform cathode utilization.
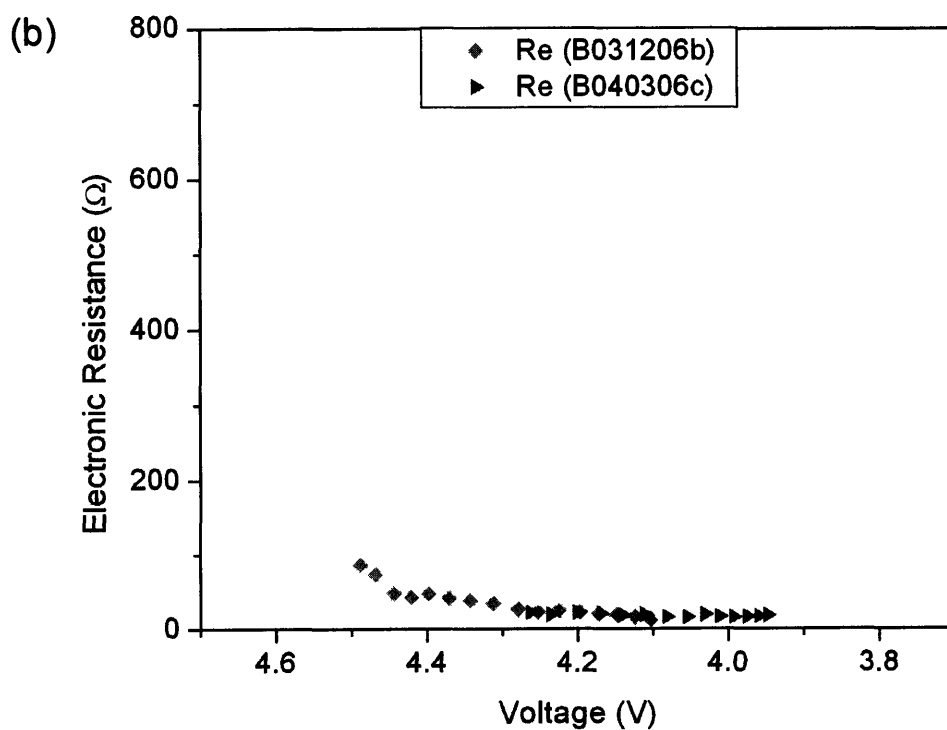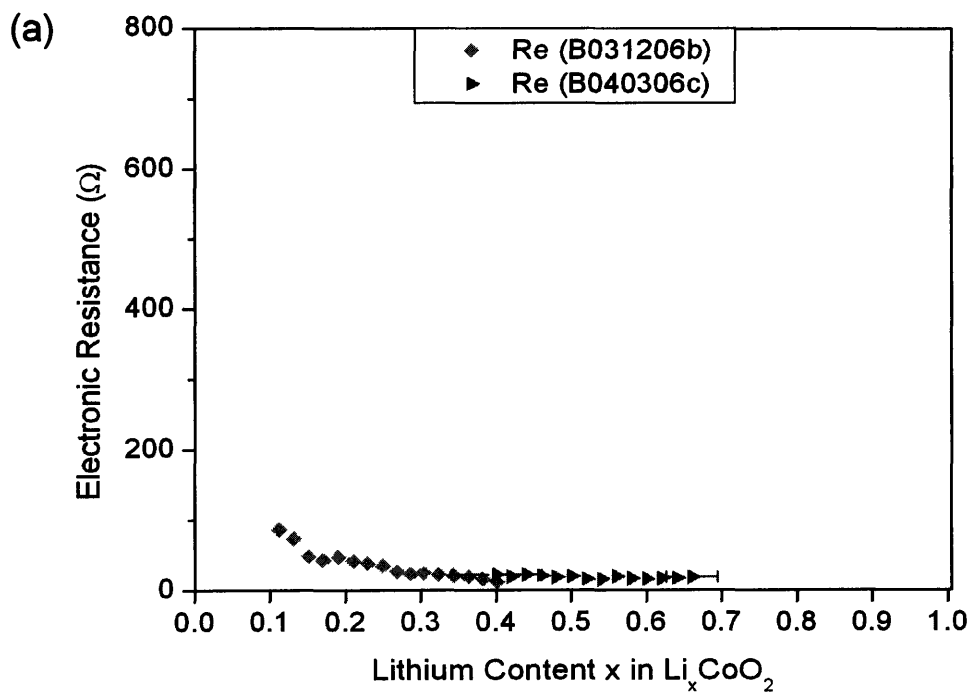

(a)

Electronic Resistance (Ω)

◆ Re (B031206b)
▶ Re (B040306c)

Lithium Content x in Li_xCoO_2

(b)

Electronic Resistance (Ω)

◆ Re (B031206b)
▶ Re (B040306c)

Voltage (V)

Figure 43. Equivalent circuit fitting for the EIS spectra yields trends in electronic resistance as a function of delithiation in $AlPO_4$-coated Li_xCoO_2 for electrode batches C1 and C2. The resistance change with lithium content in (a) shows the rapid decrease of R_e at the beginning of deintercalation. X-error bars are included to indicate the effect of weighing errors and nonuniform cathode utilization. Resistance as a function of voltage, (b), shows the relation to features in the charge profile and removes weighing errors.

(a)

(b)
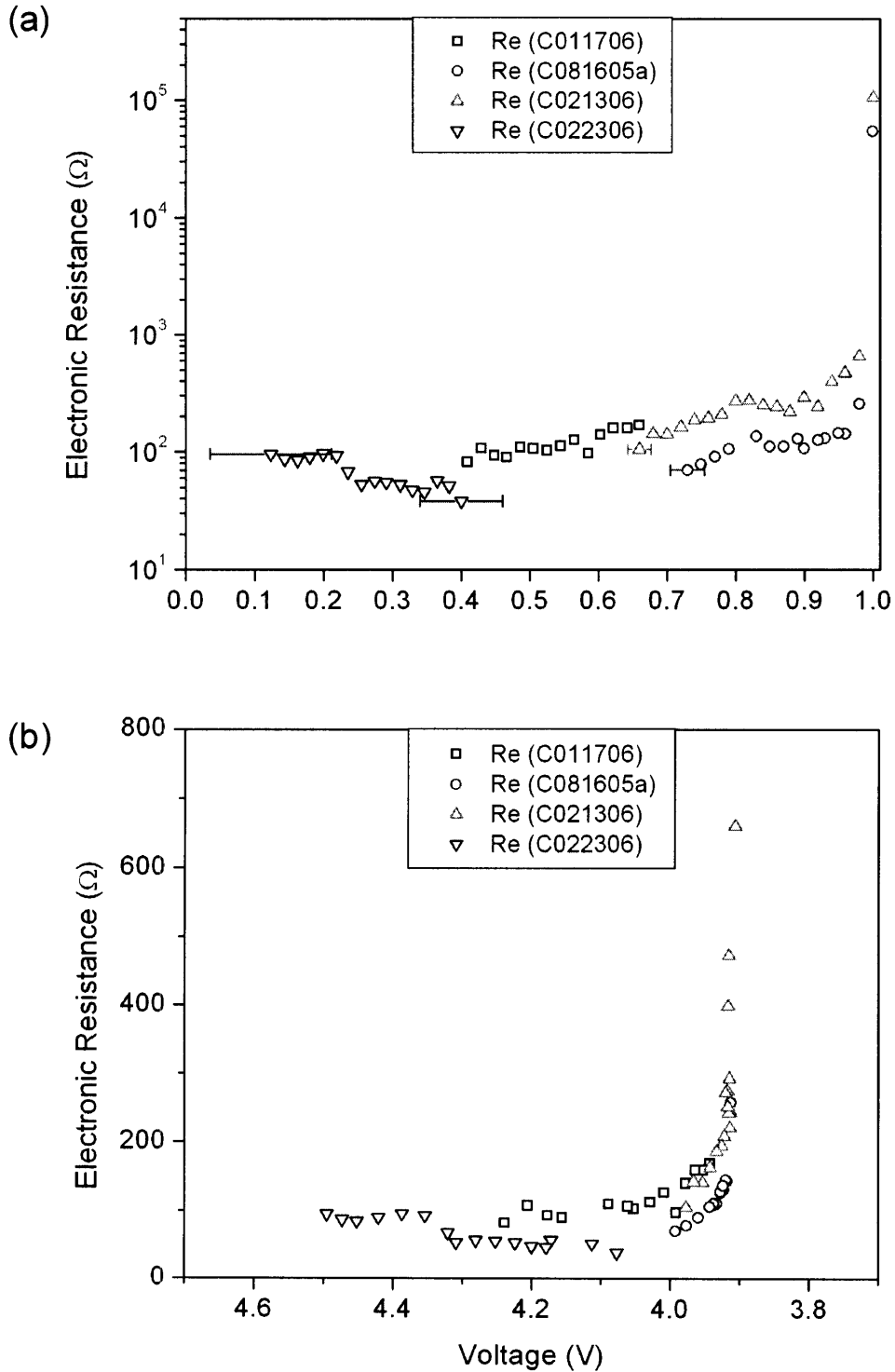
b. Cross-Sectional Morphology

The following images of $AlPO_4$-coated $LiCoO_2$ were prepared as discussed in Chapter II. Figure 44 shows a continuous coating layer region with ~50nm thickness on a microtomed $LiCoO_2$ particle. Figure 45 provides further support for the images shown in Chapter IV.

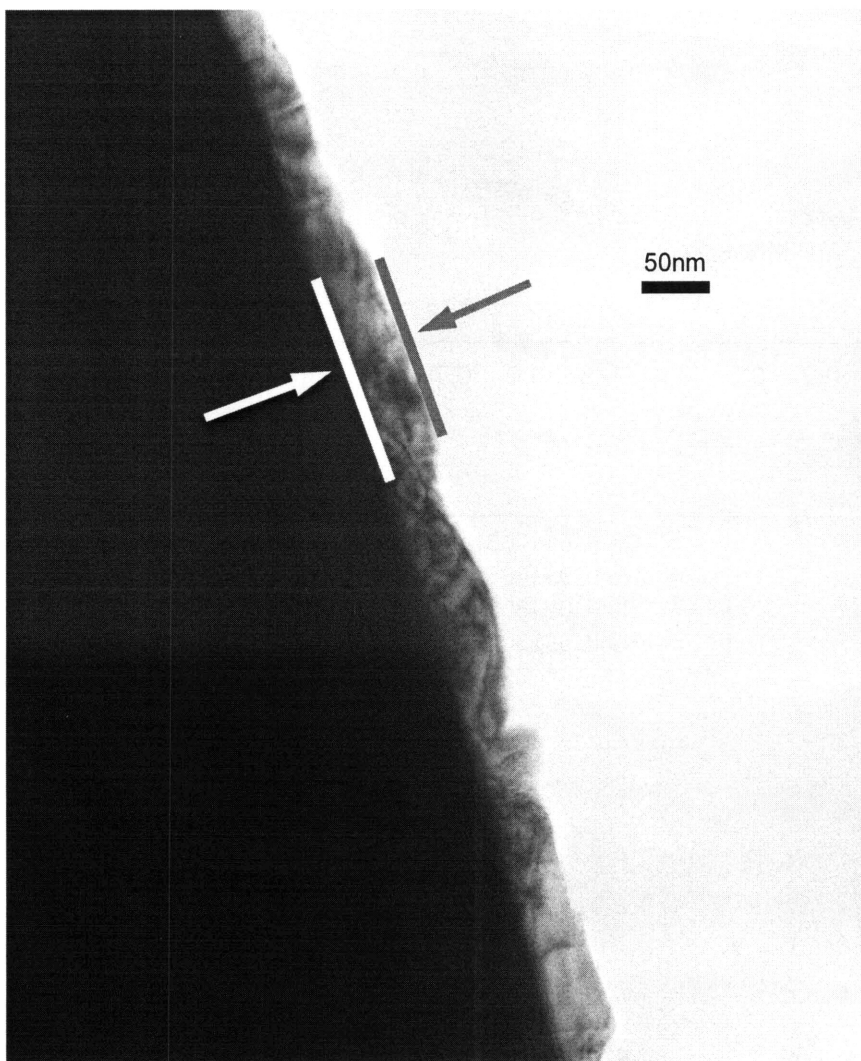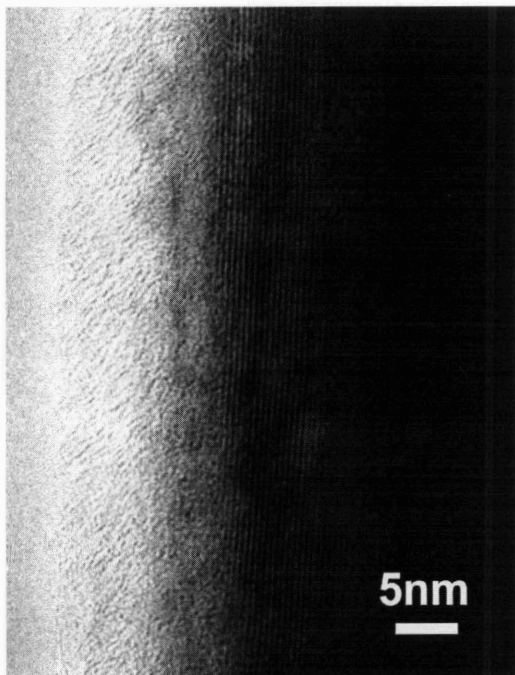Figure 44. Transmission electron micrograph of $AlPO_4$ coating layer on $LiCoO_2$ particle.

Figure 45. High-resolution transmission electron micrograph of $AlPO_4$ coating layer on $LiCoO_2$. Lattice fringes can be seen in the bulk of the $LiCoO_2$.

5nm